Solange Vieira da Silva

1 2 9 0

UNIVERSIDADE Ð
COIMBRA

Solange Vieira da Silva

TRAPPING LIGHT IN METAL AND TOPOLOGICAL
NANOSTRUCTURES

Março de 2020

TRAPPING LIGHT IN METAL AND TOPOLOGICAL NANOSTRUCTURES

UNIVERSIDADE Ð
COIMBRA

1 2 9 0

To my family, friends and boyfriend.

Abstract

Nanophotonics is a field of research dedicated to study the interactions of nanosized-objects with light. One of the goals of nanophotonics is to enable the miniaturization of optical components at a competitive scale with microelectronics. There are several rewards in using light based technologies, such as building photonic circuits that are not only smaller but faster and more efficient than the electronic counterparts, new solar cells that have enhanced energy absorption, nano-optical sensors able to detect ultralow concentrations of molecules in chemical solutions, amongst many others. My work aims to contribute to this field of research by exploring new mechanisms to accomplish an efficient spatial confinement of light.

This thesis is devoted to the analytical and numerical study of three different ways to confine light in the nanoscale.

First, we investigate light trapping in open plasmonic resonators (meta-atoms) with different shapes. It is found that in some conditions complex-shaped dielectric cavities may support discrete light states screened by volume plasmons that in the limit of a vanishing material loss have an infinite lifetime. The embedded eigenstates can be efficiently pumped with a plane wave excitation when the meta-atom core has a nonlinear response, such that the trapped light energy is precisely quantized. Then, we investigate how the spatial dispersion effects, e.g., caused by the electron-electron interactions in a metal, affect these trapped eigenstates in three-dimensional open plasmonic resonators. Heuristically, one may expect that the repulsive-type electron-electron interactions should act against light localization, and thereby that they should have a negative impact on the formation of the embedded eigenstates. Surprisingly, it is found that the nonlocality of the material response creates new degrees of freedom and relaxes the requirements for the observation of trapped light. In particular, a zero-permittivity condition is no longer mandatory and the same resonator shell can potentially suppress the radiation loss at multiple frequencies.

The possibility to trap and guide light in wire metamaterials is also investigated. Specifically, we investigate the guided modes supported by a metamaterial slab formed by two mutually orthogonal and nonconnected sets of parallel metallic wires. It is demonstrated that the wire medium slab has a peculiar comb-like dispersion diagram. In the continuum approximation, the metamaterial supports a diverging number of guided mode branches that accumulate near the light line due to a strong hyperbolic response in the static limit. In a realistic system, the number of guided modes branches is finite and is determined by the density of wires. Remarkably, the guided modes may be characterized by a fast field variation along the transverse direction, which can be exploited to detect subwavelength particles or defects.

Lastly, we investigated topological trapped states in photonic crystals. We show that in one-dimensional periodic systems the number of bands below a band gap determines the topological Chern number of an extended system with a synthetic dimension. It is theoretically and numerically demonstrated that in

real-space the Chern number gives the number of gapless trapped state branches localized at the interface of the photonic crystal, when its geometry is continuously displaced by one lattice period. Furthermore, we introduce a novel class of topological systems with inversion-symmetry and fractional (non-integral) Chern numbers. It is proven that the non-integral topological number arises due to the discontinuous behaviour of the Hamiltonian in the spectral domain. We introduce a bulk-edge correspondence that links the number of edge-states with the fractional topological number.

Resumo

A nano-fotónica é uma área de investigação dedicada ao estudo das interacções da luz com objectos nanométricos. Um dos objectivos da nanofotónica é possibilitar a miniaturização de componentes ópticos para uma escala competitiva com a microelectrónica. Existem vários benefícios em usar tecnologia fotónica, como a construção de circuitos fotónicos com pequenas dimensões que não são apenas mais rápidos mas também mais eficientes do que as suas contrapartes eletrónicas, novas células solares com uma maior absorção energética, sensores nano-ópticos capazes de detectar concentrações extremamente baixas de moléculas em soluções químicas, entre outros. O objectivo principal do meu trabalho é contribuir para esta área de investigação, explorando novos mecanismos de confinamento espacial da luz de forma eficiente.

Esta tese é dedicada ao estudo analítico e numérico de três mecanismos diferentes de confinar a luz à nano-escala.

Em primeiro lugar, é investigado o aprisionamento da luz em ressoadores plasmónicos abertos (meta-átomos) de diferentes geometrias. É mostrado que, em certas condições, cavidades dieléctricas de geometrias complexas podem suportar estado fotónicos discretos que, no limite em que as perdas materiais são nulas, possuem tempos de vida infinitos. Estes estados surgem devido à acção dos plasmões de volume suportados pela camada plasmónica exterior do meta-átomo e podem ser excitados eficientemente por uma onda plana quando o núcleo do ressoador possui uma resposta não-linear. Demonstra-se que a energia aprisionada no núcleo do ressoador é precisamente quantizada. Depois, é investigado o impacto dos efeitos de dispersão espacial, causados por exemplo pelas interacções electrão-electrão em metais, nos estados próprios embebidos suportados por ressoadores abertos plasmónicos tridimensionais. Heuristicamente, seria de esperar que as interacções repulsivas electrão-electrão agissem de maneira deteriorante no mecanismo de localização de luz e, portanto, tivessem um impacto negativo na formação dos estados próprios embebidos. Surpreendentemente, é mostrado neste trabalho que a dispersão não-local do material que encapsula o meta-átomo dá origem a novos graus de liberdade e relaxa os requisitos necessários ao aprisionamento da luz. Em particular, a condição que exige que o material da cápsula exiba uma permitividade exactamente igual a zero deixa de ser obrigatória, passando a ser possível que a mesma cápsula suprima a perda por radiação em várias frequências.

É estudada de seguida a possibilidade de aprisionar e guiar luz em metamateriais de fios metálicos. Especificamente, investigamos os modos guiados suportados por um metamaterial formado por dois planos de fios metálicos mutuamente ortogonais. É demonstrado que o meio de fios tem um diagrama de dispersão peculiar, semelhante a um pente. No limite em que o material é visto como um meio contínuo (homogeneizado), o metamaterial suporta um número divergente de "ramos" de modos guiados que se acumulam junto à linha da luz devido à forte resposta hiperbólica do metamaterial no limite estático. Num sistema realista, o número de ramos é finito e determinado pela densidade de fios. Curiosamente, os modos são caracterizados por uma variação do campo

rápida na direcção transversal, que pode ser explorada na detecção de partículas e defeitos de dimensão sub-lambda.

Por último, são investigados modos de luz topologicamente aprisionados em cristais fotónicos. São estudadas as propriedades topológicas de sistemas periódicos unidimensionais, e é mostrado que o número de bandas abaixo do hiato de frequências determina o número de Chern de um sistema extendido com uma dimensão sintética. É demonstrado teórica e numericamente que, no espaço-real, o número de Chern determina o número de estados aprisionados na interface de um cristal fotónico no intervalo de frequências da banda não-propagante, quando a sua geometria sofre uma deslocação contínua de um período de estrutura. Além disso, é introduzida uma nova classe de sistemas topológicos com inversão de simetria e números de Chern fraccionários. É provado que o número topológico fraccionário é devido às descontinuidades do Hamiltoniano no domínio espectral. É introduzida uma correspondência volume-interface que liga o número de estados de interface com o número topológico fraccionário.

Palavras-Chave– Plasmónica, Efeitos não-lineares, Estados próprios embutidos, Meios de fios, Imagiologia sub-lambda, Metamateriais, Fotónica topológica, Número de Chern, Correspondência volume-interface.

Preface

In this document, I present my Doctoral dissertation that results from work carried from January 2015 to December 2019 under the supervision of Professor Mário Silveirinha and Professor Tiago Morgado, at the University of Coimbra. My work was supported financially and technically by Fundação para a Ciência e Tecnologia, Instituto de Telecomunicações – Coimbra, and Department of Electrical and Computer Engineering of the Faculty of Science and Technology of the University of Coimbra. The originality and scientific validity of my work is sustained by a series of conference and journal papers published during my PhD. Future publications are still in order regarding some part of my work. Except where explicit reference is made to the work of others, the work contained in this dissertation is my own.

Acknowledgements

In all my life, I always found myself pursuing what was the most interesting and difficult endeavor I could find. I constantly have a feeling of restlessness that compels me to never be satisfied and to always try to learn something new every day. In the words of my father "knowledge takes no space in us", which are words that I never forget in anything I do. Under this belief, I jumped into this extraordinary adventure with thirst of knowledge and determination to make the best of these years. But I must confess, it was the hardest experience I ever had. In fact, I experienced all types of negative feelings during my PhD: desperation, sadness, disappointment, anger, doubt, depression... I had multiple times where I wanted to give up, and this was a totally new feeling for me. However, I was also blessed with the most valuable things someone can have that allowed me to push through and endure this challenge: family, friends and infinite support. Therefore, I dedicate these pages of my dissertation to all of you that made possible for me to complete this insane but rewarding task.

To Professor Mário Silveirinha I want to say that it was a true honor to meet him and to have the opportunity to work with him. I feel very lucky to have been accepted as his PhD student and grateful to know such an extraordinary scientist, but also the most kind and ethical person I have ever met. I will always cherish this time I had with him in my heart.

To Professor Tiago Morgado I want to thank for the patience and time spent on teaching me to be a better professional and also for always keeping up with my work. I truly admire his critical spirit and his rigorous work methodology. Also, I thank him for letting me be part of his circle of friends, for which I feel deeply privileged.

To my colleagues in the microwave laboratory I want to thank for all the help and support. To David and Verónica I want to specially thank for the endless support, not only technical but mostly emotional. I am very lucky to have gained such good friends and I hope to always be a part of their life.

To all my close friends that stayed with me throughout the years, I thank you for never doubting I could do this and, although geographically far, for always being close.

To my family it is hard to fully express how impactful you were in my success. Life changes all the time, but family always stays by our side. To my mother and father, I thank you for your extraordinary education, for the great perseverance you showed all these years and for wanting only the best for me. To my sisters, I thank you for never leaving my side, for the effort in trying to understand my not so good moments and for constantly believing in me.

I would like to especially thank Professor Henrique Silva, who unfortunately left us too soon, for cultivating my passion for photonics with his unparalleled expertise.

Last but not least, to Rui for always being there for me, in the good and the bad moments. Specially the bad moments, when you showed great wisdom and shone light when the darkness entrapped me.

Contents

List Of Symbols

ε_0	Dielectric permittivity of vacuum
μ_0	Magnetic permeability of vacuum
ε_r	Relative dielectric permittivity
μ_r	Relative magnetic permeability
ω	Angular frequency
ω_p	Plasma angular frequency
ω_c	Collision angular frequency
$\mathbf{E}$	Electric field vector
$\mathbf{H}$	Magnetic field vector
J_n	Bessel function of the first kind and order n
c	Speed of light in vacuum
k_0	Wave number in free space
Q	Quality factor
T	Period of oscillation
τ_{ph}	Oscillation lifetime
η_0	Wave impedance in vacuum
$\Delta\tau$	Full-width half maximum
$\chi^{(3)}$	Third-order nonlinear susceptibility
ε_∞	High-frequency relative permittivity
$\varepsilon_\mathrm{r,T}$	Relative permittivity seen by the transverse mode
$\varepsilon_\mathrm{r,L}$	Relative permittivity seen by the longitudinal mode
v_F	Fermi velocity
β	Nonlocality strength parameter
$Y_w^{\pm}$	Transverse wave admittance
$\mathbf{j}$	Current density
ρ	Charge density
$\bar{\varepsilon}$	Effective permittivity of the electron gas
Y_n	Bessel spherical harmonic of order n
a	Lattice period
λ	Wavelength
r_w	Wire radius
β_p	Effective plasma wavenumber
$\mathbf{k}$	Wavevector
$\mathbf{k}_{||}$	Transverse wavevector
L	Wire medium thickness
γ_0	Free-space propagation constant
f	Frequency
$\hat{H}_\mathbf{q}$	Hermitian operator parameterized by $\mathbf{q}$
C	Chern number (topological number)
$\hat{H}$	Hamiltonian
$\mathcal{A}_\mathbf{q}$	Berry potential
$Z_\mathrm{R,L}$	Bloch wave impedances calculated when looking at the right or left, respectively
θ_Zak	Zak phase

x

CHAPTER 1

Introduction

1.1 Background

The ability to communicate with no geographical restrictions with anyone in the world was once a dream of humanity, turned into reality in the last century. Some scientists attribute our tremendous evolutionary success to our unique communication skills. In fact, we are the only animals to have speech and complex languages with which not only we cooperate in tasks but also express feelings and eternize our creative thought. With the evolution of language, it became easy for small populations to exchange ideas and make decisions by having simple conversations, but as population increased there was an rising need to communicate efficiently with other populations that were physically far. This happened when transportation became readily available through horses and boats, which made possible cultural and technological exchanges that completely transformed human civilization.

Obviously, carrying a message through a rider in a horse was not ideal since it depended greatly on factors like weather conditions and, plus, was extremely slow. However, the advent of electricity gave us the first truly long-distance technology that was fast and reliable: the electric telegraph in the 1830s. The telegraph used electrical signals to convey information through copper wires. It was the first form of telecommunication that relied on travelling electrons. This event marked the beginning of a new technological era for telecommunications.

Later, we witness the birth of modern physics when Albert Einstein ex-

plained the origin of the photoelectric effect in 1905. Furthermore, when scientists started to study quantum-mechanical phenomena they concluded that light is made up of elementary particles called photons that exhibit wave-particle duality. Similar to electrons, photons were also capable of carrying information in guides such as optical fibers. Importantly, light can carry a larger amount of information and at much higher velocities than electrons. Ultimately, this led to the current state of affairs, where most of the communication systems are formed by a complex network of electronic and optical devices.

Even though light already dominates the transmission path, where instead of copper wires now we use optical fibers, a significant part of the communication systems still remains electronic. This means that there is a need for signal conversion in the system, from electrical to optical and vice versa, which is both inefficient and costly. To overcome this obstacle, researchers engineered photonic devices capable of creating, manipulating and detecting light like optical amplifiers [1], lasers [2–5] and light-emitting diodes [6–8]. These devices explore the electromagnetic interaction of light with the materials to achieve the relevant response. However, the footprint of light-based technologies is too large due to the limitation imposed by the diffraction limit of light in dielectric media, which does not allow the spatial localization of electromagnetic waves in the subwavelength regime. This hampers the miniaturization efforts of the optical circuits in scales equivalent to the electronic circuits.

Plasmonics may offer a solution to achieve optical miniaturization. It was found, as early as 1900, that the electromagnetic waves and electrons may interact strongly in metallic interfaces or in small metallic nanostructures, leading to enhanced optical near field of subwavelength dimension. This was latter described as a collective electron excitation, known as surface and volume plasmons. There are innumerous applications for plasmonic effects in technology, like plasmon nanoguiding [9–11] which can be realized through various types of metallic nanostructures, such as metal films of finite thickness and width embedded in a homogeneous dielectric. Another interesting developed technology based on plasmonics is Surface Enhanced Raman Scattering (SERS) [12–14], which provides much greater detection sensitivity than conventional Raman spectroscopy of biological molecules adsorbed by metal surfaces. Other application is the fabrication of electronic circuits through nanolithography [15–17]. Due to the increasingly small circuits, optical projection lithography benefits of surface plasmons that strongly enhance

2

the nanoscale spatial distribution of the electrical field near the surface.

With the evolution of optical technologies came an increasing necessity for materials that provided extraordinary and unusual electromagnetic responses. Researchers tried instead to fabricate their own artificial materials by tailoring the microscopic structure in such a manner that the materials behaved electromagnetically in the desired way. These structures are called "metamaterials," and typically consist of metallic or dielectric inclusions separated by a lattice constant much smaller than the radiation wavelength. The wave propagation depends on the overall properties of the structure and the discrete nature of the structure can be ignored: the material behaves as a homogeneous and continuous medium. It is possible then to describe it with an overall dielectric permittivity and magnetic permeability using homogenization techniques: this is known as the effective-medium approximation. Since the electromagnetic parameters of these materials depend on the geometry and composition of the man-made inclusions, the metamaterial concept offers an unprecedented flexibility in designing new electromagnetic responses. One of the most studied class of artificial media are arrays of metallic wires, known as "wire metamaterials". Such media have shown great potential in electromagnetic manipulation in the subwavelength scale [18–22], showing also other extraordinary effects such has superlensing [23–25], negative refraction [26,27], anomalous high density of photonic states [28,29] and strong spatial dispersion [30,31].

Another way of obtaining extraordinary optical effects is recurring to topological materials. The topology of a photonic material characterizes the global properties of the Bloch eigenfunctions. This new field of research is rooted in ideas originally developed to understand topological phases of matter in solid-state physics. In photonics, it has allowed us to discover novel states of light and consequently new extraordinary applications [32,33]. One discovery in condensed matter-physics that spurred the most interest was the discovery of topological insulators, which are materials that are isolators in the bulk but allow for propagation of electrons on their surface without backscattering even in the presence of impurities [34–37]. There are different classes of topological insulators, and typically the topological properties are rooted in some particular symmetry of the system, e.g., invariance to discrete translations, time-reversal symmetry, or others. The first example of a topological system in condensed matter was an electron gas biased with a magnetic field. In such case, it turns out that the Hall conductivity is quantized, and its quantum is determined by a topological invariant known

3

as the Chern number. Haldane and Raghu proposed a photonic analogue of Chern insulators in gyrotropic photonic crystals [40,41], which was later confirmed by experiments realized by *Wang et al* [42]. This analogy originated a series of subsequent scientific studies, resulting in some promising technological applications. One of the most important applications is the possibility to construct waveguides that transmit electromagnetic energy without reflection and thus can dramatically improve the robustness of optical devices against construction imperfections, mitigating the impact of insertion loss [43–45]. This could decrease significantly the power requirements of classical signals.

1.2 Scope of research

Spatial confinement of light is of tantamount importance to the development of optical devices, since it can be potentially useful for light-emitting devices [46,47] (e.g. plasmonic nanolasers), optical switching [48,49] and enhanced nonlinear effects [50]. In particular, there is currently a great demand for mechanisms that enable confining and storing light into tiny volumes for very long oscillation periods. However, this goal remains elusive today because the coupling with the surrounding environment invariably leads to absorption and radiation losses. The standard way to confine light into some space-region is by using opaque physical barriers, e.g., reflecting mirrors [51] or photonic band-gap materials [52,53], or alternatively by exploiting the total internal reflection as in whispering gallery resonators [54,55]. However, these resonators typically need to have dimensions much larger than the radiation wavelength to effectively block the radiation leakage to the exterior. Other mechanisms that promote the light localization rely on plasmonics [56,57], weakly radiating anapole modes in dielectric nanoparticles [58] and Anderson localization [59,60].

In this thesis, we investigate novel mechanisms to confine light in subwavelength spatial dimensions by using materials with a plasmonic nature, wire metamaterials and topological photonic materials. First, we explore the formation of "embedded eigenstates" by using plasmonic materials. These optical bound states have suppressed radiation loss and exist within the radiation continuum in open resonators [61–71]. Next, we explore the use of wire metamaterials to spatially confine electromagnetic energy along the transversal direction. At last, we investigate the topological properties of periodic systems and use them in a advantageous way to concentrate light

4

between two photonic crystals. We present the theoretical description of the relevant mechanisms for each studied problem using analytical models and numerically demonstrate the validity of our results.

1.3   Organization of the Thesis

This thesis is organized in 6 chapters, with the first one being this introduction.

In chapter II, we investigate light trapping in open plasmonic resonators (meta-atoms) with different shapes. We start by theoretically analyzing different possible cross-sectional geometries and deriving the analytical conditions under which the meta-atom supports embedded eigenstates. Then, we characterize the electromagnetic response of the meta-atom in the linear regime. Lastly, we consider a nonlinear material response in the meta-atom and investigate the properties of the trapped light energy, namely its quantization and decay in time.

In chapter III, we investigate the impact of a spatially-dispersive shell on the embedded eigenstates supported by the meta-atom. To this end, we start by doing a full electromagnetic characterization of the particle using Mie theory and using the hydrodynamic model to consider the impact of the nonlocal effects. By enforcing suitable boundary conditions, we obtain a characteristic equation whose solutions describe the allowed values for the occurrence of embedded eigenstates. We then calculate the embedded eigenstate solutions in terms of several parameters of the resonator and analyze the electromagnetic fields spatial distribution of such solutions. Lastly, we characterize the response of the meta-atom under external excitation.

In chapter IV, we study wave guiding in wire metamaterials. Specifically, we investigate the guided modes supported by a wire metamaterial slab formed by two mutually orthogonal and nonconnected sets of parallel wires. Firstly, using homogenization techniques and additional boundary conditions, we theoretically describe the electromagnetic properties of the fundamental transverse magnetic bulk modes supported by the wire medium slab. Then, we calculate the dispersion characteristic of the guided modes and compare the analytical results with full-wave simulations. Finally, we devise a subwavelength detector for defects or imperfections based on the studied guided modes.

Lastly, we study in chapter V topological light states in photonic crystals.

To that end, we investigate the topological properties of one-dimensional periodic systems. First, we describe the wave propagation along the periodic dimension using Hermitian operators and Bloch waves. We then add a synthetic dimension to the system and we show that, due to the cyclic nature of the Hermitian operator in both dimensions, it is possible to characterize its topological phases. We are then able to perform the calculation of the Chern number (topological number) associated with each photonic band. Remarkably, we find that the gap Chern number is determined by the number of bands below the gap, which is thereby a topological number. In the second part of the chapter, we establish a bulk-edge correspondence that links the number of gapless trapped states in real-space and the calculated topological number. We illustrate the developed ideas with several numerical examples with one-dimensional photonic crystals and also full-wave simulations of the trapped states that corroborate our hypothesis. Finally, we consider 1D-type systems with inversion symmetry. We show that in these type of systems, when the unit cell of the crystal is displaced only by half a period, the topological numbers are not integers but rather fractional numbers. We explain the consequences of this exotic feature and develop a fractional bulk edge-correspondence. To conclude, we show several numerical examples of such systems.

In chapter VI, the main conclusions and achievements of this thesis are reviewed.

1.4   List of Author Publications

1.4.1   Articles in Journal

[J1]   S. V. Silva, D. E. Fernandes, T. A. Morgado, and M. G. Silveirinha, "Fractional Chern numbers and topological pumping in photonic systems," - *Under review.*

[J2]   S. V. Silva, T. A. Morgado, and M. G. Silveirinha, "Multiple Embedded Eigenstates in Nonlocal Plasmonic Nanostructures," *Physical Review B - Condensed Matter and Materials Physics* **101**, 4, pp. 041106 (2020) - *This paper has been selected by the editors of PRB to be an Editors' Suggestion.* DOI: 10.1103/PhysRevB.101.041106

6

[J3]   S. V. Silva, T. A. Morgado, and M. G. Silveirinha, "Comb-like modal dispersion diagram in a double wire medium slab," *IEEE Trans. Antennas and Propag.* **68**, 3, pp. 1755-1760 (2020) - *Invited article in the special issue on "Recent Advances in Metamaterials and Metasurfaces".* DOI: 10.1109/TAP.2019.2950044

[J4]   S. V. Silva, T. A. Morgado, and M. G. Silveirinha, "Discrete Light Spectrum of Complex Shaped Meta-Atoms," *Radio Science* **53**, pp. 144-153 (2018) - *Invited article.* DOI: 10.1002/2017RS006381

1.4.2   Articles in Conference Proceedings

[C1]   S. V. Silva, T. A. Morgado, and M. G. Silveirinha, "Trapped light states in spatially dispersive plasmonic nanostructures," *International Conference on Metamaterials, Photonic Crystals and Plasmonics META*, Lisbon, Portugal (July 2019).

[C2]   S. V. Silva, T. A. Morgado, and M. G. Silveirinha, "Trapping light in open nanocavities with spatial dispersion," *Congresso do Comité Português da URSI*, Lisboa, Portugal (July 2019).

[C3]   S. V. Silva, T. A. Morgado, and M. G. Silveirinha, "Diverging number of guided mode branches in a wire-medium slab," *EIEC-XII Iberian Meeting on Computational Electromagnetics*, Coimbra, Portugal (May 2018).

[C4]   S. V. Silva, T. A. Morgado, and M. G. Silveirinha, "Light trapping in an all-dielectric open cavity," *International Congress on Engineered Material Platforms for Novel Wave Phenomena - Metamaterials*, Marseille, France (August 2017).

1.4.3   Awards

[A1]   First place on the "Best Student Paper Award Contest" in the 12th Congress on "Artificial Intelligence and Radio Sciences", organized by the URSI Portuguese Committee (2018).

Bibliography

[1] M. Wasfi, "Optical fiber amplifiers - review," *Int. J. Commun. Netw. Inf. Secur.*, vol. 1, April 2009.

[2] M. N. Zervas and C. A. Codemard, "High power fiber lasers: A review," *IEEE J. Sel. Top. Quantum Electron.*, vol. 20, April 2014.

[3] N. Dutta, "Long wavelength semiconductor lasers," *Technical Digest., International Electron Devices Meeting*, August 2002.

[4] X. Duan, Y. Huang, R. Agarwal, and C. M. Lieber, "Single-nanowire electrically driven lasers," *Nature*, vol. 421, pp. 241–245, 2003.

[5] C. W. Roberson, "A review of free-electron lasers," *Phys. Fluids B: Plasma Phys.*, vol. 1, no. 3, 1989.

[6] D. Delbeke, R. Bockstaele, P. Bienstman, R. Baets, and H. Benisty, "High-efficiency semiconductor resonant-cavity light-emitting diodes: a review," *IEEE J. Sel. Top. in Quantum Electron.*, vol. 8, pp. 189 – 206, August 2002.

[7] J. H. Burroughes, D. D. C. Bradley, A. R. Brown, R. N. Marks, K. Mackay, R. H. Friend, P. L. Burns, and A. B. Holmes, "Light-emitting diodes based on conjugated polymers," *Nature*, vol. 347, pp. 539–541, 1990.

[8] R. Fiederling, M. Keim, G. Reuscher, W. Ossau, G. Schmidt, A. Waag, and L. W. Molenkamp, "Injection and detection of a spin-polarized current in a light-emitting diode," *Nature*, vol. 402, pp. 787–790, 1999.

[9] D. K. Gramotnev and S. I. Bozhevolnyi, "Plasmonics beyond the diffraction limit," *Nat. Photonics*, vol. 4, pp. 83–91, 2010.

[10] X. Ni, S. Ishii, A. V. Kildishev, and V. M. Shalaev, "Ultra-thin, planar, babinet-inverted plasmonic metalenses," *Light Sci. Appl.*, vol. 2, p. 72, 2013.

[11] M. I. Stockman, "Nanofocusing of optical energy in tapered plasmonic waveguides," *Phys. Rev. Lett.*, vol. 93, September 2004.

[12] S. Nie and S. R. Emory, "Probing single molecules and single nanoparticles by surface-enhanced raman scattering," *Science*, vol. 275, pp. 1102–1106, February 1997.

[13] K. Kneipp, Y. Wang, H. Kneipp, L. T. Perelman, I. Itzkan, R. R. Dasari, , and M. S. Feld, "Single molecule detection using surface-enhanced raman scattering (sers)," *Phys. Rev. Lett.*, vol. 78, March 1997.

[14] A. Otto, I. Mrozek, H. Grabhorn, and W. Akemann, "Surface-enhanced raman scattering," *J. Phys. Condens. Matter*, vol. 4, no. 5.

[15] W. Srituravanich, N. Fang, C. Sun, Q. Luo, and X. Zhang, "Plasmonic nanolithography," *Nano Lett.*, vol. 4, pp. 1085–1088, May 2004.

[16] Y. Kim, S. Kim, H. Jung, E. Lee, and J. W. Hahn, "Plasmonic nano lithography with a high scan speed contact probe," *Opt. Express*, vol. 17, no. 22, pp. 19476–19485, 2009.

[17] Y. Kim, S. Kim, H. Jung, E. Lee, and J. W. Hahn, "High-speed plasmonic nanolithography with a solid immersion lens-based plasmonic optical head," *Appl. Phys. Lett.*, vol. 101, no. 161109, 2012.

[18] P. A. Belov, Y. Hao, and S. Sudhakaran, "Subwavelength microwave imaging using an array of parallel conducting wires as a lens," *Phys. Rev. B*, vol. 73, p. 033108, January 2006.

[19] M. G. Silveirinha, P. A. Belov, and C. R. Simovski, "Subwavelength imaging at infrared frequencies using an array of metallic nanorods," *Phys. Rev. B*, vol. 75, p. 035108, January 2007.

[20] P. A. Belov, Y. Zhao, S. Tse, P. Ikonen, M. G. Silveirinha, C. R. Simovski, S. Tretyakov, Y. Hao, and C. Parini, "Transmission of images with subwavelength resolution to distances of several wavelengths in the microwave range," *Phys. Rev. B*, vol. 77, p. 193108, May 2008.

[21] P. Ikonen, C. Simovski, and S. Tretyakova, "Magnification of subwavelength field distributions at microwave frequencies using a wire medium slab operating in the canalization regime," *Appl. Phys. Lett.*, vol. 91, p. 104102, 2007.

[22] G. Shvets, S. Trendafilov, J. B. Pendry, and A. Sarychev, "Guiding, focusing, and sensing on the subwavelength scale using metallic wire arrays," *Phys. Rev. Lett.*, vol. 99, p. 053903, August 2007.

[23] M. G. Silveirinha, "Artificial plasma formed by connected metallic wires at infrared frequencies," *Phys. Rev. B*, vol. 79, p. 035118, January 2009.

[24] M. G. Silveirinha, C. A. Fernandes, and J. R. Costa, "Superlens made of a metamaterial with extreme effective parameters," *Phys. Rev. B*, vol. 78, p. 195121, November 2008.

[25] M. G. Silveirinha, C. R. Medeiros, C. A. Fernandes, and J. R. Costa, "Experimental verification of broadband superlensing using a metamaterial with an extreme index of refraction," *Phys. Rev. B*, vol. 81, p. 033101, January 2010.

[26] Y. Liu, G. Bartal, and X. Zhang, "All-angle negative refraction and imaging in a bulk medium made of metallic nanowires in the visible region," *Opt. Express*, vol. 16, pp. 15439–15448, Sep 2008.

[27] J. Yao, Z. Liu, Y. Liu, Y. Wang, C. Sun, G. Bartal, A. M. Stacy, and X. Zhang, "Optical negative refraction in bulk metamaterials of nanowires," *Science*, vol. 321, no. 5891, pp. 930–930, 2008.

[28] S. I. Maslovski and M. G. Silveirinha, "Ultralong-range casimir-lifshitz forces mediated by nanowire materials," *Phys. Rev. A*, vol. 82, p. 022511, August 2010.

[29] S. I. Maslovski and M. G. Silveirinha, "Mimicking boyer's casimir repulsion with a nanowire material," *Phys. Rev. A*, vol. 83, p. 022508, February 2011.

[30] M. G. Silveirinha, "Nonlocal homogenization model for a periodic array of ε-negative rods," *Phys. Rev. E*, vol. 73, p. 046612, April 2006.

[31] P. A. Belov, R. Marqués, S. I. Maslovski, I. S. Nefedov, M. Silveirinha, C. R. Simovski, and S. A. Tretyakov, "Strong spatial dispersion in wire media in the very large wavelength limit," *Phys. Rev. B*, vol. 67, p. 113103, March 2003.

[32] L. Lu, J. Joannopoulos, and M. Soljačić, "Topological photonics," *Nature Photon.*, vol. 8, p. 821–829, October 2014.

[33] T. Ozawa, H. M. Price, A. Amo, N. Goldman, M. Hafezi, L. Lu, M. C. Rechtsman, D. Schuster, J. Simon, O. Zilberberg, and I. Carusotto, "Topological photonics," *Rev. Mod. Phys.*, vol. 91, p. 015006, Mar 2019.

[34] M. Z. Hasan and C. L. Kane, "Colloquium: Topological insulators," *Rev. Mod. Phys.*, vol. 82, pp. 3045–3067, November 2010.

[35] X.-L. Qi and S.-C. Zhang, "Topological insulators and superconductors," *Rev. Mod. Phys.*, vol. 83, pp. 1057–1110, October 2011.

[36] L. Fu, C. L. Kane, and E. J. Mele, "Topological insulators in three dimensions," *Phys. Rev. Lett.*, vol. 98, p. 106803, March 2007.

[37] J. Moore, "The birth of topological insulators," *Nature*, vol. 464, pp. 194–198, 2010.

[38] K. v. Klitzing, G. Dorda, and M. Pepper, "New method for high-accuracy determination of the fine-structure constant based on quantized hall resistance," *Phys. Rev. Lett.*, vol. 45, pp. 494–497, Aug 1980.

[39] K. von Klitzing, "The quantized hall effect," *Rev. Mod. Phys.*, vol. 58, pp. 519–531, Jul 1986.

[40] F. D. M. Haldane and S. Raghu, "Possible realization of directional optical waveguides in photonic crystals with broken time-reversal symmetry," *Phys. Rev. Lett.*, vol. 100, p. 013904, Jan 2008.

[41] S. Raghu and F. D. M. Haldane, "Analogous of quantum hall effect edge states in photonic crystals," *Phys. Rev. A*, vol. 78, p. 033834, Sept 2008.

[42] Z. Wang, Y. D. Chong, J. D. Joannopoulos, and M. Soljačić, "Reflection-free one-way edge modes in a gyromagnetic photonic crystal," *Phys. Rev. Lett.*, vol. 100, p. 013905, Jan 2008.

[43] Y. E. Kraus, Y. Lahini, Z. Ringel, and M. V. amd O. Zilberberg, "Topological states and adiabatic pumping in quasicrystals," *Phys. Rev. Lett.*, vol. 109, p. 106402, Sept 2012.

[44] M. C. Rechtsman, J. M. Zeuner, Y. Plotnik, Y. Lumer, D. Podolsky, F. Dreisow, S. Nolte, M. Segev, and A. Szameit, "Photonic floquet topological insulators," *Nature*, vol. 496, p. 196–200, Sept 2013.

[45] M. Hafezi, S. Mittal, J. Fan, A. Migdall, and J. M. Taylor, "Imaging topological edge states in silicon photonics," *Nature Photon.*, vol. 7, p. 1001–1005, Oct 2013.

[46] M. A. Noginov, G. Zhu, A. M. Belgrave, V. M. S. R. Bakker, E. E. Narimanov, S. Stout, E. Herz, T. Suteewong, and U. Wiesner, "Demonstration of a spaser-based nanolaser," *Nature*, vol. 460, pp. 1110—1112, 2009.

[47] R. F. Oulton, V. J. Sorger, T. Zentgraf, R.-M. Ma, C. Gladden, L. Dai, G. Bartal, and X. Zhang, "Plasmon lasers at deep subwavelength scale," *Nature*, vol. 461, pp. 629—632, 2009.

[48] M. Bajcsy, S. Hofferberth, V. Balic, T. Peyronel, M. Hafezi, A. S. Zibrov, V. Vuletic, and M. D. Lukin, "Efficient all-optical switching using slow light within a hollow fiber," *Phys. Rev. Lett.*, vol. 102, p. 203902, May 2009.

[49] K. Nozaki, T. Tanabe, A. Shinya, S. Matsuo, T. Sato, H. Taniyama, and M. Notomi, "Sub-femtojoule all-optical switching using a photonic-crystal nanocavity," *Nat. Photonics*, vol. 4, pp. 477—483, 2010.

[50] B. Luk'yanchuk, N. I. Zheludev, S. A. Maier, N. J. Halas, P. Nordlander, H. Giessen, and C. T. Chong, "The fano resonance in plasmonic nanostructures and metamaterials," *Nat. Mater.*, vol. 9, pp. 707—715, 2010.

[51] G. Rempe, R. J. Thompson, H. J. Kimble, and R. Lalezari, "Measurement of ultralow losses in an optical interferometer," *Opt. Lett.*, vol. 17, pp. 363–365, 1992.

[52] P. Lalanne, C. Sauvan, and J. P. Hugonin, "Photon confinement in photonic crystal nanocavities," *Laser and Photon. Rev.*, vol. 2, pp. 514–526, 2008.

[53] H. Sekoguchi, Y. Takahashi, T. Asano, and S. Noda, "Photonic crystal nanocavity with a q-factor of 9 million," *Opt. Express*, vol. 22, pp. 916–924, 2014.

[54] A. B. Matsko and V. S. Ilchenko, "Optical resonators with whispering-gallery modes - part i: basics," *IEEE J. Sel. Top. Quantum Electron.*, vol. 12, pp. 3–14, 2006.

[55] I. S. Grudinin, V. S. Ilchenko, and L. Maleki, "Ultrahigh optical q factors of crystalline resonators in the linear regime," *Phys. Rev. A*, vol. 74, p. 063806, 2006.

[56] I. M. Tribelsky and B. S. Luk'yanchuk, "Anomalous light scattering by small particles," *Phys. Rev. Lett.*, vol. 97, p. 263902, 2006.

[57] B. Luk'yanchuk, N. I. Zheludev, S. A. Maier, N. J. Halas, P. Nordlander, H. Giessen, and C. T. Chong, "The fano resonance in plasmonic nanostructures and metamaterials," *Nat. Mater.*, vol. 9, pp. 707–715, 2010.

[58] A. E. Miroshnichenko, A. B. Evlyukhin, Y. F. Yu, R. M. Bakker, A. Chipouline, A. I. Kuznetsov, B. Luk'yanchuk, B. N. Chichkov, and Y. S. Kivshar, "Nonradiating anapole modes in dielectric nanoparticles," *Nat. Commun.*, vol. 6, p. 8069, 2015.

[59] A. Lagendijk, B. V. Tiggelen, and S. D. Wiersma, "Fifty years of anderson localization," *Phys. Today*, vol. 62, p. 24, 2009.

[60] M. Segev, Y. Silberberg, and D. N. Christodoulides, "Anderson localization of light," *Nat. Photonics*, vol. 7, pp. 197–204, 2013.

[61] D. C. Marinica and A. G. Borisov, "Bound states in the continuum in photonics," *Phys. Rev. Lett.*, vol. 100, p. 183902, 2008.

[62] M. I. Molina, A. E. Miroshnichenko, and Y. S. Kivshar, "Surface bound states in the continuum," *Phys. Rev. Lett.*, vol. 108, p. 070401, 2012.

[63] Y. Plotnik, O. Peleg, F. Dreisow, M. Heinrich, S. Nolte, A. Szameit, and M. Segev, "Experimental observation of optical bound states in the continuum," *Phys. Rev. Lett.*, vol. 107, p. 183901, 2011.

[64] J. Lee, B. Zhen, S.-L. Chua, W. Qiu, J. D. Joannopoulos, M. Soljacic, and O. Shapira, "Observation and differentiation of unique high-q optical resonances near zero wave vector in macroscopic photonic crystal slabs," *Phys. Rev. Lett.*, vol. 109, p. 067401, 2012.

[65] C. W. Hsu, B. Zhen, J. Lee, S.-L. Chua, S. G. Johnson, J. D. Joannopoulos, and M. Soljacic, "Observation of trapped light within the radiation continuum," *Nature*, vol. 499, pp. 188–191, 2013.

[66] C. W. Hsu, B. Zhen, A. D. Stone, J. D. Joannopoulos, and M. Soljacic, "Bound states in the continuum," *Nat. Rev. Mater.*, vol. 1, p. 16048, 2016.

[67] E. N. Bulgakov and A. F. Sadreev, "Resonance induced by a bound state in the continuum in a two-level nonlinear fano-anderson model," *Phys. Rev. B*, vol. 80, p. 115308, 2009.

[68] E. N. Bulgakov and A. F. Sadreev, "Bound states in a photonic fabry-perot resonator with nonlinear off-channel defects," *Phys. Rev. B*, vol. 81, p. 115128, 2010.

[69] E. N. Bulgakov and A. F. Sadreev, "Robust bound state in the continuum in a nonlinear microcavity embedded in a photonic crystal waveguide," *Optic. Lett.*, vol. 39, pp. 5212–5215, 2014.

[70] E. N. Bulgakov, K. N. Pichugin, and A. F. Sadreev, "All-optical light storage in bound states in the continuum and release by demand," *Opt. Express*, vol. 23, p. 17, 2015.

[71] M. Minkov, I. A. D. Williamson, M. Xiao, and S. Fan, "Zero-index bound states in the continuum," *Phys. Rev. Lett.*, vol. 121, p. 263901, 2018.

CHAPTER 2

Light trapping in 2D open plasmonic nanostructures with complex geometries

2.1 Introduction

The natural modes of oscillation of a physical system can be usually split into two categories: the bound modes – which form the discrete spectrum – and the extended modes – which form the continuous spectrum. Usually, the discrete and the continuous spectra do not overlap. For example, in the hydrogen atom the allowed electron energy levels are split into two disjoint subsets: the discrete negative energies (bound states) and the continuous positive energies (free-electron states). The discrete spectrum is invariably associated with spatially localized states that are square integrable and hence normalizable. On the other hand, the continuous spectrum is associated with delocalized (extended) states that are not square-integrable. The emergence of a spatially localized state in a regime wherein the natural modes are inherently delocalized is contrary to common sense and may seem *a priori* impossible because of the markedly different nature of these states. For example, in electronic systems it is counterintuitive to have a bound state at the same energy level for which the system supports free electron states. Surprisingly, it was shown by von Neumann and Wigner in 1929 that bound states embedded in the continuum (embedded eigenstates) are really allowed

within the framework of the usual wave theories [1, 2], and the concept of an electronic state with "positive energy" was even experimentally verified in the context of semiconductor heterostructures [3].

Notably, in recent years there has been a considerable interest in the emergence of embedded eigenstates in photonic platforms [4–9]. In particular, it has been shown that open material structures (e.g., standing in free-space) with tailored geometries may support spatially localized stationary light oscillations with a square integrable electromagnetic field distribution, notwithstanding that at the same oscillation frequency the system also supports infinitely many spatially extended modes (belonging to the continuous spectrum) [4, 6–9]. Here, we note that in photonic platforms formed by material inclusions standing in free-space a localized photonic state is always embedded in the radiation continuum and hence is an "embedded eigenstate". Moreover, it should be highlighted that the emergence of embedded eigenstates in open (optically transparent) material structures is rather surprising because usually light escapes from any open region due to the radiation leakage. Until recently, all the known configurations to localize light in the radiation continuum with transparent materials required unbounded (infinitely extended) material structures [4, 6–9], which in practice has limited interest. Any deviation from the ideal situation leads to a perturbed localized eigenstate with a finite lifetime.

In a recent series of works [10–12], it was developed a different paradigm to implement open material structures with a discrete light spectrum. It was shown that volume plasmons, i.e. charge density oscillations in an electron gas, give the opportunity to confine light in a *spatially-bounded* open optical cavity in such a manner that in ideal conditions the oscillation lifetime can be infinitely large [10–14]. Moreover, in Ref. [11] it was devised a mechanism to pump the oscillations of the embedded eigenstate in a core-shell cavity and ensure at the same time that the trapped light energy has a precise value. In other words, the energy of the trapped light state is precisely quantized. Because of this property and due to the obvious analogies with electronic systems the core-shell resonator is designated as "optical meta-atom". The key idea of the "meta-atom" concept is to exploit nonlinear effects to squeeze the wavelength of the incoming light into the core region until it reaches a very precise value for which the plasmonic shell blocks the trapped radiation from exiting the meta-atom [11].

In this chapter we explore alternative two-dimensional (2D) meta-atom configurations and demonstrate that optical cavities with arbitrary com-

plex shapes can support embedded eigenstates similar to those studied in Refs. [10–12,14] for spherical core-shell geometries. Moreover, we investigate in detail realistic relaxation mechanisms of the meta-atom in the trapped regime, such as the leakage due to the conversion of light into higher order harmonics.

This chapter is organized as follows. In section 2.2, we outline different possible cross-sectional geometries for the meta-atom and derive the conditions under which the meta-atom supports embedded eigenstates. In section 2.3, we analyze the electromagnetic response of the meta-atom in the linear regime. In section 2.4, the nonlinear response of the meta-atom and the quantization of the trapped light energy are investigated. The conclusions are drawn in Sect. 2.5.

2.2 Embedded eigenstates in two-dimensional cavities

We consider a generic 2D core-shell nanostructure of arbitrary shape (Fig. 2.1) with a dielectric core with relative permittivity ε_1, and a shell with a plasma-type response in the frequency regime of interest. Specifically, it is assumed that the permittivity of the shell has a Drude-type dispersion $\varepsilon_2(\omega) = 1 - \omega_p^2/[\omega(\omega + i\omega_c)]$, where ω_p is the plasma frequency and ω_c is the collision frequency. The materials are non-magnetic $\mu = \mu_0$ and the meta-atom stands in free-space. Figure 2.1 depicts a generic geometry of the structure, being implicit that the core-shell structure is invariant to translations along the z-direction. It is also assumed that the fields are polarized in such a manner that $\mathbf{H} = H_z\hat{\mathbf{z}}$ and $\mathbf{E} = E_x\hat{\mathbf{x}} + E_y\hat{\mathbf{y}}$ (transverse magnetic – TM – polarization), and that the wave propagation is in the *xoy* plane with $\partial/\partial z = 0$. For now, it is supposed that the response of the involved materials is linear, but later we will allow the core to be characterized by a Kerr-type nonlinearity.

The embedded eigenstates may emerge in the regime wherein the shell supports volume plasmon oscillations, i.e. when the permittivity of the shell vanishes $\varepsilon_2(\omega_p) = 0$ [12]. Volume plasmons are non-radiative natural oscillations of an electron gas, which in some circumstances may hybridize with the radiation fields and in this manner perfectly screen the radiation in the core region [12]. From a purely electromagnetic point of view, this effect can
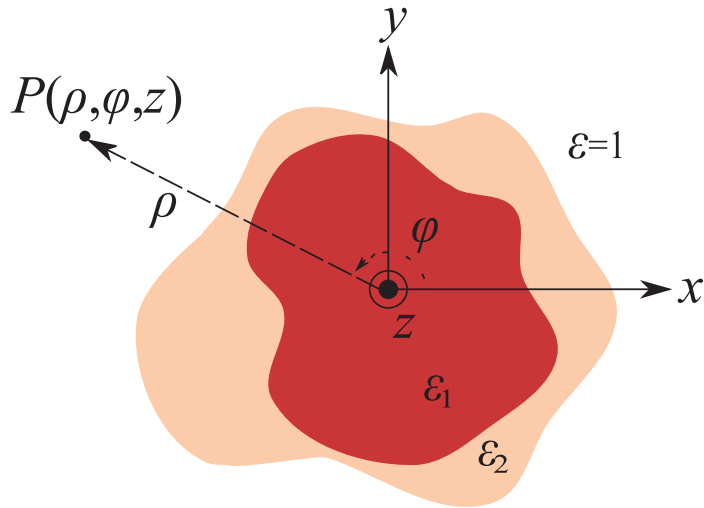
17

Figure 2.1: Generic geometry of the 2D core-shell meta-atom (top view).

be explained by the fact that a material with $\varepsilon = 0$ can behave as perfect magnetic conductor (PMC) for TM-polarized waves, which corresponds to an opaque boundary [15]. Specifically, for TM-polarized waves an $\varepsilon = 0$ material mimics precisely a PMC, except for incident waves that impinge on the material along the normal direction [15]. For normal incidence it is possible to have an energy flow through an ε-near-zero material (ENZ) due to an evanescent-type near-field tunneling effect [16–18]. Thus, the embedded eigenstates can occur at the frequency $\omega = \omega_{\mathrm{p}}$ in the limit of vanishing material loss ($\omega_{\mathrm{c}} \to 0$ with ε_1 real-valued).

Having a shell with $\varepsilon_2 = 0$ is a necessary but not a sufficient condition to trap light in the core-shell resonator. Indeed, there is an additional requirement: the geometry and the material parameters of the core region need to be such that $\omega = \omega_{\mathrm{p}}$ is coincident with one of the natural oscillation frequencies ω_m^{PMC} (m=1,2,...) of the equivalent PMC cavity [12]:

$$\omega_{\mathrm{p}} = \omega_m^{\mathrm{PMC}}, \quad \text{for some } m. \tag{2.1}$$

In the system under study the modes of the equivalent PMC cavity are solutions of a Dirichlet boundary value problem:

$$\nabla \cdot \left(\frac{1}{\varepsilon}\nabla H_z\right) + \frac{\omega^2}{c^2}H_z = 0, \quad \text{in the core region,} \tag{2.2a}$$

$$H_z = 0, \quad \text{at the core boundary.} \tag{2.2b}$$

Furthermore, in order that the field in the shell can have a purely electrostatic nature (volume plasmon mode), only the cavity modes with $\oint_{\text{core boundary}} \mathbf{E} \cdot \mathbf{dl} = 0$ are allowed. Equivalently, because of Faraday's law, it is necessary that:

$$\iint_{\text{core}} H_z dx dy = 0. \tag{2.3}$$

In the following subsections we illustrate the outlined ideas for different geometries of the meta-atom. We would like to highlight that a few recent works have explored similar concepts to demonstrate that zero-index materials can be used to realize geometry invariant cavities [13, 19, 20].

2.2.1 Circular cross-section geometry

In the first example, the meta-atom has a circular cross-section such that the core has radius R_1 and the shell has radius R_2. In this case, the eigenmodes of the equivalent PMC cavity (with a PMC wall placed at $\rho = R_1$) are the solutions of Eq. (2.2a),

$$H_z = H_0 e^{in\varphi} \begin{cases} J_{|n|}\left(\frac{\omega}{c}\sqrt{\varepsilon_1}\rho\right), & \rho < R_1 \\ 0, & \text{otherwise} \end{cases}, \tag{2.4}$$

where H_0 is a normalization constant, and J_n is the Bessel function of the first kind and order n. Imposing the boundary condition (2.2b), it is found that H_z must vanish at $\rho = R_1$, which implies that for $\omega = \omega_{\text{p}}$,

$$J_{|n|}\left(\frac{\omega_{\text{p}}}{c}\sqrt{\varepsilon_1}R_1\right) = 0. \tag{2.5}$$

This condition is satisfied only for well-defined values of the inner radius R_1 and of the core permittivity ε_1. Importantly, the embedded eigenmodes only occur for a nonzero azimuthal quantum number $n \neq 0$ ($\partial/\partial\varphi \neq 0$), so

that condition 2.3 can be satisfied. From a different perspective, for $n = 0$ the electromagnetic fields are constant over the ENZ shell boundary ($\partial/\partial\varphi = 0$). Hence, waves with $n = 0$ impinge along the normal direction on the ENZ material interface so that the shell is penetrable by these waves. Thus, the ENZ shell behaves as a PMC wall only for TM-polarized waves with $\partial/\partial\varphi \neq 0$. As an example, for waves associated with the lowest order positive mode $n = 1$ (dipole mode), the first zero of $J_1(u)$ occurs for $u \approx 3.81$, and this gives the opportunity to have an embedded eigenmode with infinite lifetime for $R_1 = R_{1,0} \equiv 3.83\frac{c}{\sqrt{\varepsilon_1}\omega_{\mathrm{p}}}$ at $\omega = \omega_{\mathrm{p}}$.

The electric field of a trapped mode in the core is calculated with the usual formulas $E_\rho = \frac{1}{-i\omega\varepsilon_1}\frac{1}{\rho}\partial_\varphi H_z$ and $E_\varphi = \frac{1}{i\omega\varepsilon_1}\partial_\rho H_z$, with H_z satisfying Eq. (2.4). On the other hand, the electric field in the shell must be a solution of the Laplace equation, and thereby is of the form $\mathbf{E} = -\nabla\phi$ with $\phi = (A_1\rho^{|n|} + A_2\rho^{-|n|})e^{in\varphi}$. Taking into account that the tangential (azimuthal) electric field vanishes at the shell-air boundary and is continuous at the shell-core boundary, it is simple to prove that the electric potential satisfies:

$$\phi = \eta_1 H_0 J'_{|n|}(k_1 R_1)R_1\frac{1}{n}\frac{(\rho/R_2)^{|n|} - (\rho/R_2)^{-|n|}}{(R_1/R_2)^{|n|} - (R_1/R_2)^{-|n|}}e^{in\varphi}, \quad R_1 < \rho < R_2. \tag{2.6}$$

Thus, the electromagnetic fields in the shell remain finite in the limiting case $\varepsilon_2 = \varepsilon'_2 + i\varepsilon''_2 \to 0$, and there are no singularities in this limit.

In general, if the material loss is nonzero or if the core radius is detuned the decay time becomes finite and the corresponding oscillation frequency has an imaginary part: $\omega_r = \omega' + i\omega''$ with $\omega'' < 0$. This complex resonant frequency can be found by considering solutions of the wave equation of the form:

$$H_z = H_0 e^{in\varphi}\begin{cases} a_n J_{|n|}(k_1\rho), & \rho < R_1 \\ b_n J_{|n|}(k_2\rho) + c_n Y_{|n|}(k_2\rho), & R_1 < \rho < R_2 \\ d_n H^{(1)}_{|n|}(k_0\rho), & \rho > R_2 \end{cases} \tag{2.7}$$

where $k_0 = \omega/c$, $k_1 = k_0\sqrt{\varepsilon_1}$, $k_2 = k_0\sqrt{\varepsilon_2}$, Y_n is the Bessel function of the second kind and order n, and $H^{(1)}_n$ is the Hankel function of the first kind and order n. The coefficients a_n, b_n, c_n and d_n must be such that H_z and $\frac{1}{\varepsilon}\frac{\partial H_z}{\partial\rho}$ are continuous functions of ρ at $\rho = R_1$ and $\rho = R_2$. This yields the following homogeneous linear system

$$
\begin{bmatrix}
J_{|n|}(k_1 R_1) & -J_{|n|}(k_2 R_1) & -Y_{|n|}(k_2 R_1) & 0 \\
0 & -J_{|n|}(k_2 R_2) & -Y_{|n|}(k_2 R_2) & H_{|n|}^{(1)}(k_0 R_2) \\
\frac{k_1}{\varepsilon_1} J_{|n|}'(k_1 R_1) & -\frac{k_2}{\varepsilon_2} J_{|n|}'(k_2 R_1) & -\frac{k_2}{\varepsilon_2} Y_{|n|}'(k_2 R_1) & 0 \\
0 & -\frac{k_2}{\varepsilon_2} J_{|n|}'(k_2 R_2) & -\frac{k_2}{\varepsilon_2} Y_{|n|}'(k_2 R_2) & k_0 H_{|n|}'^{(1)}(k_0 R_2)
\end{bmatrix}
\begin{bmatrix}
a_n \\ b_n \\ c_n \\ d_n
\end{bmatrix}
=
\begin{bmatrix}
0 \\ 0 \\ 0 \\ 0
\end{bmatrix},
$$

$$(2.8)$$

which has a nontrivial solution only when ω is such that the determinant of the matrix vanishes. The quality factor of the natural mode of oscillation is given by $Q = \omega'/(-2\omega'')$ and corresponds roughly to the ratio of the lifetime (τ_{ph}) and the period of oscillation (T): $Q/2\pi = \tau_{ph}/T$ [12].

To illustrate the discussion, we consider the case wherein $R_2 = 1.1 R_1$ and the meta-atom core is filled with air ($\varepsilon_1 = 1$). Figure 2.2 shows the calculated quality factor of the meta-atom as a function of the core radius $R_1/R_{1,0}$ and for different values of the shell material loss (i.e., different values of the normalized collision frequency ω_c/ω_p). As seen in Fig. 2.2, in the ideal case wherein the collision frequency vanishes and the core radius is tuned so that $R_1/R_{1,0} = 1$, the quality factor diverges to infinity $Q = \infty$, which corresponds to an embedded eigenvalue with infinite lifetime. When the effect of material loss is considered or the core radius is detuned ($R_1 \neq R_{1,0}$), the quality factor and the oscillation lifetime become finite. Different from conventional dielectric resonators (e.g., whispering gallery cavities), the quality factor can be rather large even for subwavelength meta-atoms. In practice, the maximum quality factor is determined by the ENZ material loss. Similar to the theory of Ref. [12] for a spherical cavity, it can be checked that when $R_1/R_{1,0} = 1$ the quality factor is $Q \approx \omega_p/\omega_c$, and hence is determined by the lifetime of the volume plasmons in the ENZ shell.

In the shell region the magnetic field is of the form $H_z = e^{in\varphi} f_n(k_2 \rho)$ and hence it is possible to introduce a transverse impedance given by:

$$
\frac{E_\varphi}{H_z} \equiv Z_n^{\mathrm{TM}} = \frac{k_2}{i\omega \varepsilon_0 \varepsilon_2} \frac{f_n'(k_2 \rho)}{f_n(k_2 \rho)}, \tag{2.9}
$$

where $\eta_2 = \eta_0/\sqrt{\varepsilon_2}$ is the impedance of the shell and f_n is some linear combination of Bessel functions of order n. It can be checked that in the limit $k_2 \rho \to 0$ and for $n \geq 1$, $\frac{f_n'(k_2 \rho)}{f_n(k_2 \rho)} \sim \frac{1}{k_2 \rho}$. Thus, the transverse impedance diverges, $Z_n^{\mathrm{TM}} \to \infty$, in the limit wherein $\varepsilon_2 \to 0$. This confirms that the ENZ shell really behaves as a PMC for TM-polarized modes with $\partial/\partial\varphi \neq 0$.
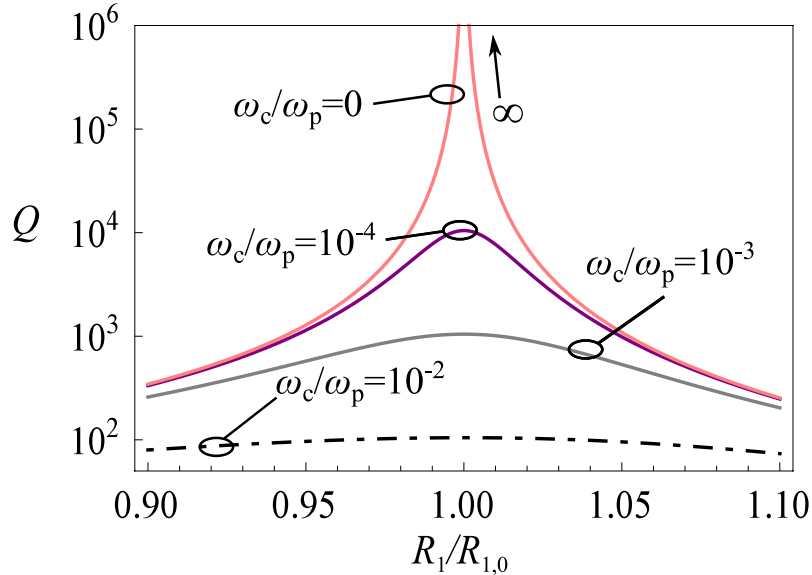
Figure 2.2: Quality factor as a function of $R_1/R_{1,0}$ for different values of the material loss in the cylindrical meta-atom shell and for the $n = 1$ mode.

Quite differently, for modes with $n = 0$ the transverse impedance is finite in the ENZ limit. For example, if $f_0 = J_0(k_2\rho)$ it can be verified that when $\varepsilon_2 \to 0$ the impedance satisfies $Z_0^{\mathrm{TM}} = i\eta_2 k_2\rho/2 = i\eta_0 k_0\rho/2$ and is therefore finite. Thus, the ENZ shell is generally penetrable by waves with $\partial/\partial\varphi = 0$ consistent with the discussion in the beginning of the subsection. It can also be verified that the transverse impedance of transverse electric (TE) waves (with electric field along the z-direction and magnetic field in the xoy plane) is finite in the ENZ limit. Thus, the ENZ shell mimics the PMC response only for a specific wave polarization and when $\partial/\partial\varphi \neq 0$, and hence the meta-atom is generally open to electromagnetic waves.

22

2.2.2 Other geometries: square-shaped and kite-shaped cross-sections

To demonstrate that the embedded eigenstates with infinite lifetime are not specific of meta-atoms with circular cross-section, we studied the natural modes of open cavities with more complex shapes, such as a square or a kite-shaped cross-section geometry [see Fig. 2.3].
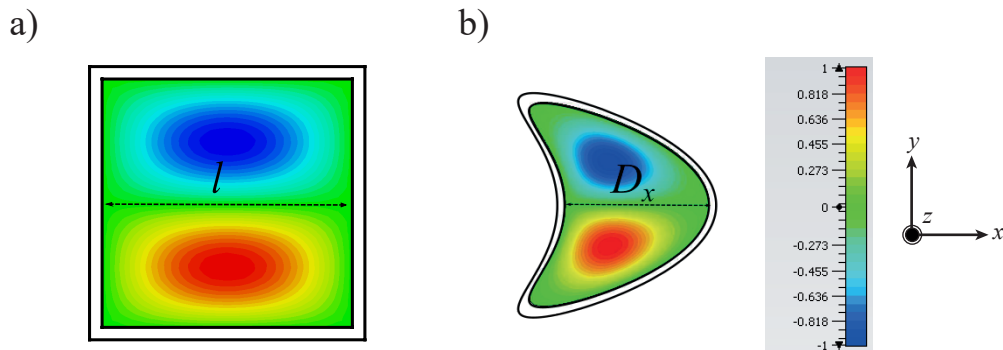
a)   b)

Figure 2.3: Snapshot in time of the magnetic field (H_z) associated with the dipolar trapped state (in arbitrary units) in a meta-atom with a) a square-shaped and b) a kite-shaped cross-section, respectively. The corresponding electric field is on average directed along the x-direction.

For a square-shaped cross-section geometry (Fig. 2.3a), Eq. (2.2) has an analytical solution, $H_z = H_0 \sin(n\frac{\pi}{l}x)\sin(m\frac{\pi}{l}y)$, where $n, m = 1, 2, ...$ are integer numbers and l is the side of the square (it is supposed that the boundaries are $x = 0, l$ and $y = 0, l$). The associated eigenfrequencies are $\omega_{S,mn} = \frac{c}{\sqrt{\varepsilon_1}}\sqrt{(\frac{m\pi}{l})^2 + (\frac{n\pi}{l})^2}$. Similar to the cylindrical case, the mode of interest cannot have a monopole-type symmetry. Indeed, the monopole mode $m = n = 1$ does not satisfy the condition (2.3) and hence must be excluded. For a dipolar-type symmetry there are two options, $(m, n) = (1, 2)$ or $(m, n) = (2, 1)$, which correspond to $\omega_{S,12} = \frac{c}{\sqrt{\varepsilon_1}}\frac{\pi}{l}\sqrt{5}$. The profile of the relevant dipolar mode is depicted in Fig. 2.3a. In order to have an embedded dipolar state it is required that the plasma frequency of the ENZ material satisfies $\omega_p = \omega_{S,12}$, or equivalently the side of the square is equal

to $l = \frac{c}{\sqrt{\varepsilon_1}} \frac{\pi}{\omega_\mathrm{p}} \sqrt{5}$.

Evidently, for a completely generic geometry, e.g. for a kite-shaped cross-section (see Fig. 2.3b), Eq. (2.2) does not have an analytical solution. In this case, the allowed oscillation frequencies of the embedded eigenstates need to be numerically determined. We used a commercial electromagnetic simulator [21] to calculate the resonant frequencies of the equivalent cavity with PMC walls. The profile of lowest frequency dipolar mode (the dipolar modes are nondegenerate for this geometry) is represented in Fig. 2.3b. From the numerical simulation, it is found that the resonant frequency is related to the diameter of the object D_x (along the x-direction) as $\omega_K = \frac{6.41c}{D_x \sqrt{\varepsilon_1}}$, so that the light trapping condition is $D_x = \frac{6.41c}{\omega_\mathrm{p} \sqrt{\varepsilon_1}}$. In summary, the geometrical conditions required to have infinite-lifetime oscillations with a dipolar mode in each of the meta-atom geometries are:

$$
\begin{aligned}
R_{1,0} &= \frac{3.83c}{\omega_\mathrm{p}\sqrt{\varepsilon_1}}, \quad \text{circular-shaped} \\
l_0 &= \frac{\sqrt{5}\pi c}{\omega_\mathrm{p}\sqrt{\varepsilon_1}}, \quad \text{square-shaped} \\
D_{x,0} &= \frac{6.41c}{\omega_\mathrm{p}\sqrt{\varepsilon_1}}, \quad \text{kite-shaped.}
\end{aligned}
\tag{2.10}
$$

Note that in the ideal case wherein the ENZ shell is lossless the oscillation frequency and the lifetime of the embedded eigenstate are totally independent of the geometry of the shell [12, 13, 19, 20].

2.3   Meta-atom excitation in the linear regime

Up to now, the discussion was focused on the physical nature and properties of the embedded eigenstates. Next, we analyze the electromagnetic response of a meta-atom under external excitation.

The meta-atom is illuminated by a linearly polarized plane wave with magnetic field along the z-direction and electric field along the x-direction. Figure 2.4 depicts the ratio between the electric field in the meta-atom core center (E_{x0}) and the incident electric field amplitude (E_inc) as a function of the frequency for the three geometries introduced in Sec. 2.2. The results of Fig. 2.4 were obtained using CST Microwave Studio [21]. Note that E_{x0}/E_inc

may be regarded as the transfer function of the meta-atom. For the circular cross-section case, E_{x0}/E_{inc} can be determined as well using Mie theory (for cylindrical waves) [12] and is given by the Mie coefficient a_1^{TM} of the inner core.
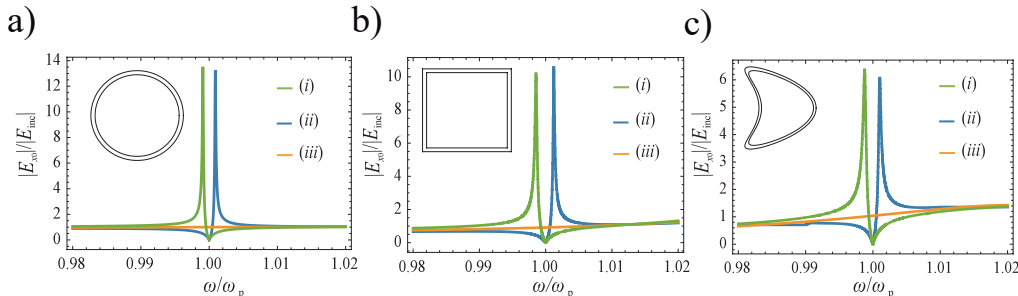

Figure 2.4: Normalized electric field in the meta-atom geometrical center as a function of the frequency for the a) circular geometry; b) square geometry; c) kite geometry. The curves (iii) correspond to meta-atoms that support embedded dipolar-type eigenstates with infinite lifetime, i.e., for which the condition (2.10) is satisfied. The curves (i) and (ii) correspond to objects with linear dimensions scaled by a factor of (i) 1.02 and (ii) 0.98 as compared to the tuned geometry [curve (iii)]. The effect of ENZ loss is neglected in the simulation ($\omega_{\text{c}}/\omega_{\text{p}} \approx 0$). The inner core has permittivity $\varepsilon_1 = 1$ for the circular-geometry and $\varepsilon_1 = 2$ for the square- and kite- geometries.

For each cross-sectional shape, we consider three different resonators with linear dimensions scaled by a factor of (i) 1.02, (ii) 0.98 and (iii) 1.00 relative to the ideal geometry [Eq. (2.10)] for which the meta-atom supports an embedded dipolar-type state with infinite lifetime. As seen in Fig. 2.4, independently of the cross-section, all the meta-atoms exhibit a similar response to the plane-wave excitation. In particular, when the meta-atom dimensions are slightly detuned from the optimum value in Eq. (2.10) [curves (i) and (ii)], the scattering coefficients display resonances with Fano-type lineshapes [22], similar to the spherical geometry case [12]. The fractional bandwidth of the resonance is inversely proportional to the quality factor, and hence for a perfectly tuned meta-atom [curves (iii)] the transfer function does not have resonant features and $|E_{x0}/E_{\text{inc}}| \approx 1$ [12]. Hence, counterintuitively, in the tuned case the meta-atom is penetrable by the incoming radiation, which

further highlights that the considered cavity is open to external excitations.

To shed some light on this intriguing property, the time dynamics of the electric field inside the meta-atom with circular cross-section was studied with CST Microwave Studio [21]. The nanostructure is illuminated by a linearly polarized plane wave with finite duration in time (Gaussian-shaped pulse). The wave propagates along the positive y direction and the Gaussian pulse is centered at $t_{\text{peak}} = 177$ ps with a full-width half maximum (FWHM) equal to $\Delta\tau = 78$ ps. The plasma frequency of the ENZ material is $\omega_{\text{p}}/2\pi = 1$ THz and the meta-atom radius is tuned according to Eq. (2.10).

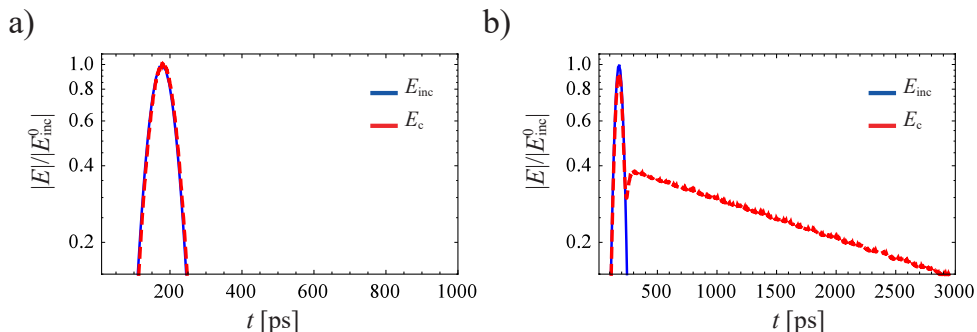a)   b)

Figure 2.5: Time evolution of the electric field envelope at the center of the meta-atom for an incident pulse with a peak amplitude $|E_{\text{inc}}^0|$ for a) $R_1 = R_{1,0}$ and b) $R_1 = 0.98R_{1,0}$. The effect of ENZ loss is neglected in the simulation ($\omega_{\text{c}}/\omega_{\text{p}} \approx 0$), the inner core has relative permittivity $\varepsilon_1 = 1$ and $R_2 = 1.1R_1$.

Figure 2.5a shows the normalized amplitude of the electric field at the center of the meta-atom as a function of time for a tuned cavity ($R_1 = R_{1,0}$). As seen, the electric field in the core is virtually coincident with the incoming field. This property is consistent with the fact that $|E_{x0}/E_{\text{inc}}| \approx 1$ (Fig. 2.4(a*iii*)), i.e. a perfectly tuned meta-atom is nearly transparent to the incoming radiation. Crucially, this property implies that the external excitation is unable to pump the embedded eigenstate with infinite lifetime when $R_1 = R_{1,0}$. Thus, consistent with the Lorentz reciprocity theorem, in the same way as the light trapped in the embedded state cannot escape from the meta-atom, an external source is also unable to excite the embedded light state with infinite lifetime [11, 12]. In contrast, Fig. 2.5(b) shows that when the structure is slightly detuned ($R_1 = 0.98R_{1,0}$) a significant part of the energy of the incoming field can remain trapped in the meta-atom, and

26

relax slowly with a decay rate $\omega'' = 4.12 \times 10^8$ rad/s, long after the incident pulse overtakes the meta-atom.

2.4 Meta-atom excitation in the nonlinear regime: Trapping a light "bit"

In Ref. [11], it was shown that the limitations imposed by the Lorentz reciprocity theorem can be surpassed with the help of a nonlinear response. The key idea is to use a nonlinear material in the core region and choose the core dimensions slightly below the optimum. The slight detuning of the inner core allows the relevant eigenstate to be externally pumped (Fig. 2.5(b), whereas the nonlinear material enables the resonator self-tuning and the trapping of a quantized amount of light energy [11]. Here, we will explore the same mechanism but for complex shaped 2D meta-atoms.

To begin with, we consider a meta-atom with a circular cross-section and set the inner radius equal to $R_1 = 0.98 R_{1,0}$. Assuming that the core has a Kerr-type nonlinear response, the condition to obtain a perfect trapping at the frequency ω_{p} can be estimated as $k_1^{\mathrm{NL}} R_1 = k_1 R_{1,0}$ [11], where $k_1^{\mathrm{NL}} = \sqrt{\varepsilon^{NL}} \frac{\omega_{\mathrm{p}}}{c}$ is the wave number inside the nonlinear medium and ε^{NL} is the relative nonlinear permittivity. This condition is equivalent to [11]

$$\chi^{(3)} \frac{3}{4} |E_{\mathrm{c}}|^2 = \varepsilon_1 \left[\left(\frac{R_{1,0}}{R_1} \right)^2 - 1 \right], \tag{2.11}$$

where $\chi^{(3)}$ is the third-order susceptibility of the nonlinear material [23] and E_{c} is the electrical field complex amplitude at the core center in the stationary state. A similar condition holds for the other cross-section geometries considered in this article with $R_{1,0}/R$ replaced by l_0/l for the square-shaped meta-atom and by $D_{x,0}/D_x$ for the kite-shaped meta-atom. Importantly, Eq. (2.11) reveals that E_{c}, and thereby also the field energy trapped in the meta-atom, are precisely quantized and only depend on the geometrical parameters of the resonator and on the considered materials. To demonstrate these ideas, we studied the time dynamics of the electric field in the open resonator when it is excited by a pulse with the same Gaussian profile as in the previous section. As discussed in Ref. [11], the effect of loss in the ENZ material is strongly detrimental to the light trapping in the core (see Fig. 2.2), and in practice the ENZ material loss needs to be compensated by some

active material with optical gain. Thus, in what follows it is assumed that the ENZ shell is lossless ($\omega_c/\omega_p \approx 0$).
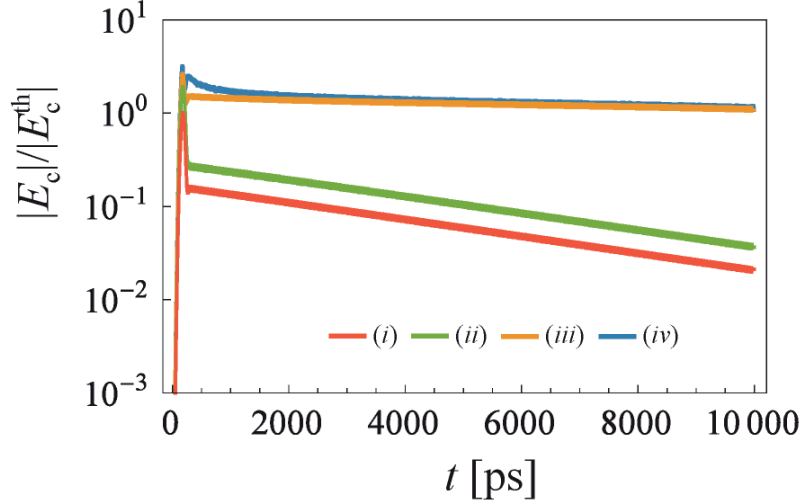

Figure 2.6: Time variation of the normalized electric field $|E_c|/|E_c^{\text{th}}|$ in the core for an excitation pulse with (*i*) $|E_{\text{inc}}^0| = 1|E_c^{\text{th}}|$, (*ii*) $|E_{\text{inc}}^0| = 2|E_c^{\text{th}}|$, (*iii*) $|E_{\text{inc}}^0| = 3|E_c^{\text{th}}|$, and (*iv*) $|E_{\text{inc}}^0| = 4|E_c^{\text{th}}|$, with the parameter $\chi^{(3)}$ fixed.

Figure 2.6 depicts the peak amplitude of the electric field in the core (i.e., the field envelope) as a function of time for different values of the peak amplitude of the incident field $|E_{\text{inc}}^0|$. For the sake of generality, we use normalized units so that the electric field is normalized to $|E_c^{\text{th}}| = \sqrt{\frac{4}{3}\frac{\varepsilon_1}{\chi^{(3)}}\left[\left(\frac{R_{1,0}}{R_1}\right)^2 - 1\right]}$, i.e., the theoretical value of the field in steady-state regime [Eq. (2.11)]. For example, if the third-order nonlinear susceptibility of the core is $\chi^{(3)} = 10^{-18}$ m^{-2}V^{-2} and $\varepsilon_1 = 1$ one has $|E_c^{\text{th}}| = 2.3 \times 10^8$ V/m.

The results of Fig. 2.6 confirm that in the stationary regime E_c always saturates at the same value [curves (*iii*) and (*iv*)], and hence the trapped light energy is indeed quantized. In our example, the saturation value is $|E_c| = 1.16|E_c^{\text{th}}|$, showing that the theoretical formula (2.11) underestimates the field in the core. The difference is expected because Eq. (2.11) is derived under the assumption that the electric field is uniform in the core. Thus, in steady-state the required nonlinearity strength is $\chi^{(3)}|E_c|^2 = 0.07$. The

nonlinearity strength can be made as small as one wishes with a design with $R_1/R_{1,0}$ closer to the unity. Moreover, one can see from Fig. 2.6 that there is a threshold value for $|E_{\mathrm{inc}}^0|$, and the light trapping only occurs for incident pulses with amplitude larger than the threshold. In the example of Fig. 2.6 the threshold is roughly $|E_{\mathrm{inc}}^0| = 3|E_{\mathrm{c}}^{\mathrm{th}}|$ [curve (*iii*)].

To further understand the nonlinear mechanisms that enable the light trapping, we show in Fig. 2.7 the normalized field in the core (in the horizontal axis) as a function of the normalized incident field (in the vertical axis) in the nonlinear regime and for two fixed frequencies near ω_{p}. This plot was obtained using $|E_{\mathrm{inc}}| = \frac{1}{|a_1^{\mathrm{TM}}|}|E_{\mathrm{c}}|$, with a_1^{TM} the Mie coefficient in the core. The Mie coefficient is a function of the core permittivity $\varepsilon^{\mathrm{NL}} = \varepsilon_1 + \frac{3}{4}\chi^{(3)}|E_{\mathrm{c}}|^2$, and thereby of the core electric field. Remarkably, the characteristic $|E_{\mathrm{c}}|$ *vs* $|E_{\mathrm{inc}}|$ is multi-valued, and hence the meta-atom has a bi-stable response.
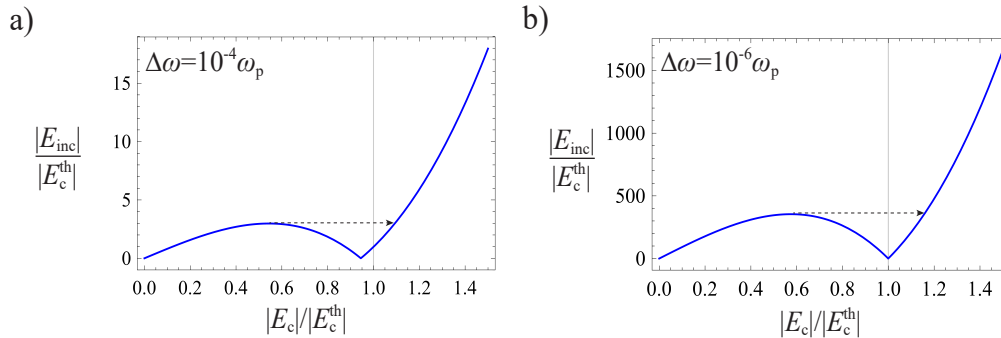
a)
b)

Figure 2.7: Bi-stable characteristic of the meta-atom for the fixed frequency $\omega = \omega_{\mathrm{p}} + \Delta\omega$ with a) $\Delta\omega = 10^{-4}\omega_{\mathrm{p}}$ and b) $\Delta\omega = 10^{-6}\omega_{\mathrm{p}}$. The arrow indicates the discontinuous transition between different branches.

The light trapping occurs at the point $|E_{\mathrm{c}}| = |E_{\mathrm{c}}^{\mathrm{th}}|$ and $|E_{\mathrm{inc}}| = 0$ when $\omega = \omega_{\mathrm{p}}$. To reach this point the amplitude of the incoming wave must exceed a threshold value, so that the transition between the two branches (indicated by the arrow) may take place. This threshold value depends strongly on the frequency detuning $\Delta\omega$ with respect to $\omega = \omega_{\mathrm{p}}$. The threshold value is roughly $3|E_{\mathrm{c}}^{\mathrm{th}}|$ for curve (a) and $350|E_{\mathrm{c}}^{\mathrm{th}}|$ for curve (b), and approaches infinity in the limit $\Delta\omega \to 0$. In practice, the meta-atom is excited by a finite duration pulse with a spectrum sufficiently wide to excite a continuum range of $\Delta\omega$. Thus, the threshold value that enables the transition from the

first to the second branch is determined by the global frequency response of the meta-atom.
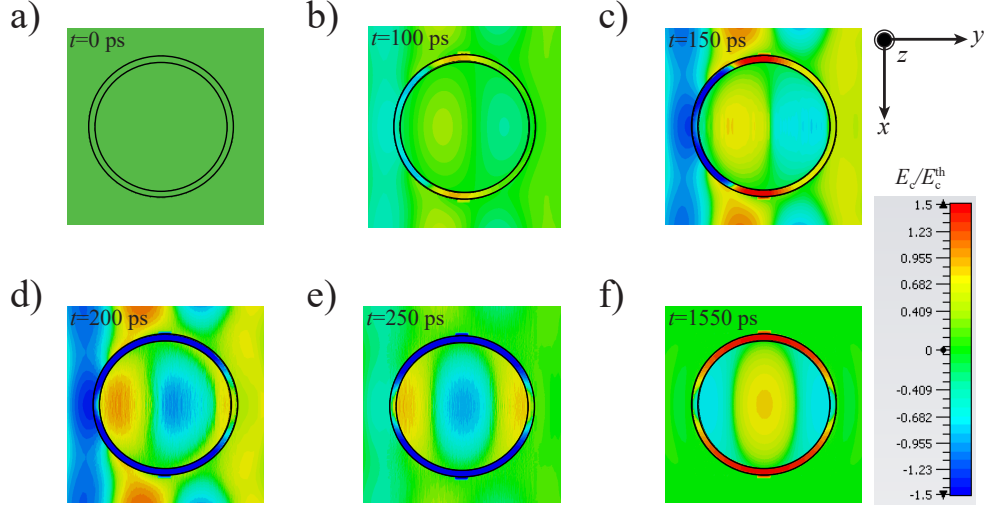

Figure 2.8: Time snapshots of the x-component of the electric field in the xoy plane showing the excitation of the meta-atom by the incoming pulse that propagates along the $+y$-direction, and the trapping of a light "bit" in the core after the incoming pulse overtakes the meta-atom.

To illustrate the dynamics of the light trapping, we show in Fig. 2.8 several time snapshots of the x-component of the electric field for the simulation of Fig. 2.6(iii). Figure 2.8 clearly shows that a quantized amount of the energy of the excitation pulse stays trapped in the open resonator and that there is no energy leaked to the exterior after the core permittivity is self-tuned.

As a result of the nonlinear response of the dielectric core, there is a frequency conversion so that a third-order harmonic is generated in the core [see Fig. 2.9]. The third-order harmonic generation may affect the mode lifetime and may contribute to the relaxation of the trapped light [11], but the process appears to be rather slow.

In order to investigate the impact of changing the cross-section geometry, we also analyzed the temporal dynamics of the fields in a kite-type resonator [see Fig. 2.3(b)]. Figure 2.10 shows the normalized electric field peak ampli-
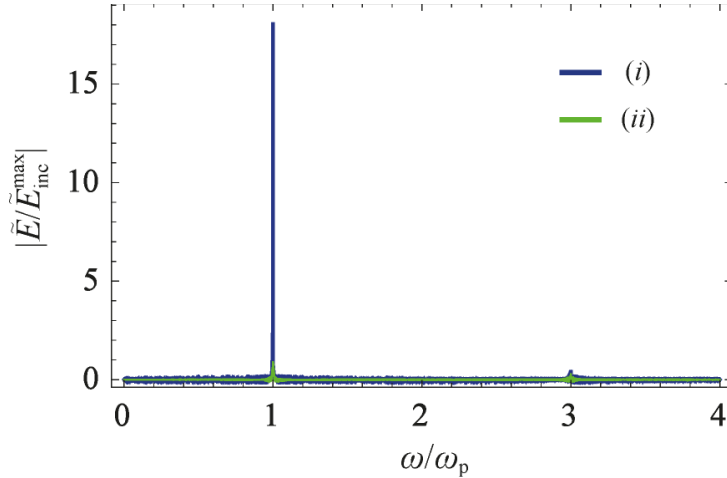
Figure 2.9: Plot of the Fourier transform of the x-component of the electric field normalized to the peak value of the Fourier transform of the incident wave: (i) at the center of the meta-atom and (ii) outside the meta-atom, at $(x, y, z) = (0, 1.5R_2, 0)$. The duration of the simulation is $114\Delta\tau$ and the simulation parameters are as in Fig. 2.6(iii).

tude at the center of the kite-shaped meta-atom for different amplitudes of the incident pulse. The diameter of the kite-shaped object is $D_x = 0.98D_{x,0}$ [curves (i-iv)] and the core permittivity in the linear regime is $\varepsilon_1 = 2$. The excitation pulse and the ENZ material are the same as in the previous examples. The results of Fig. 2.10 are somewhat analogous to those of the circular cross-section case in Fig. 2.6. In particular, in the trapping regime the field in the core has a nearly constant amplitude. However, the kite-geometry appears to be much more sensitive to realistic decay mechanisms (e.g., third harmonic conversion or absorption effects), because after the time instant $t = 2000$ ps the light bit escapes from the core at the same rate as in the linear regime. This increased sensitivity to relaxation mechanisms as compared to the meta-atom with circular cross-section is in part due to the lower quality factor of the kite resonator (see Fig. 2.4). In fact, for a kite resonator with a larger quality factor ($D_x = 0.99D_{x,0}$) [curve (v) of Fig. 2.10] the light bit is withheld in the core for a considerably longer period of time. However, it is evident that the circular cross-section geometry enables a more robust performance.
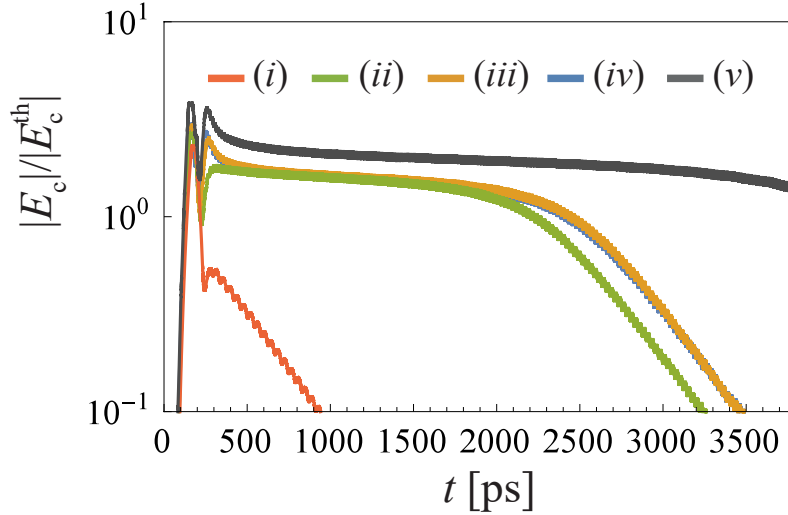
Figure 2.10: a) Time variation of the normalized electric field at the center of the kite-shaped meta-atom for an incident pulse with peak amplitude (*i*) $|E_{inc}^0| = 3|E_c^{th}|$, (*ii*) $|E_{inc}^0| = 4|E_c^{th}|$, (*iii*) $|E_{inc}^0| = 5|E_c^{th}|$ and (*iv*) $|E_{inc}^0| = 6|E_c^{th}|$. Curve (*v*) is for a kite with diameter $D_x = 0.99 D_{x,0}$ and an incident pulse with peak amplitude $|E_{inc}^0| = 7.13|E_c^{th}|$.

2.5 Conclusions

In this chapter we demonstrated that the light trapping mechanism introduced in Refs. [11,12] may be generalized to open core-shell plasmonic particles with arbitrary shape. When some particular geometrical conditions are satisfied, complex-shaped cavities can support embedded eigenstates that in the lossless limit have an infinite lifetime. Moreover, it was shown that a fundamental restriction imposed by the Lorentz reciprocity theorem, which forbids the direct external excitation of the embedded eigenstates, can be circumvented with a nonlinear dielectric response, similar to what was done in [11] for a spherical core-shell geometry. The amount of energy retained within the meta-atom is precisely quantized and depends only on the core-shell geometry. Numerical simulations suggest that the meta-atom geometry has a considerable influence on the sensitivity to relaxation mechanisms.

Bibliography

[1] J. V. Neumann and E. Wigner, "Über merkwürdige diskrete eigenwerte," *Phys. Z*, vol. 30, no. 465, 1929.

[2] F. H. Stillinger and D. R. Herrick, "Bound states in the continuum," *Phys. Rev. A*, vol. 11, no. 446, 1975.

[3] F. Capasso, C. Sirtori, J. Faist, D. L. Sivco, S. N. Chu, and A. Y. Cho, "Observation of an electronic bound state above a potential well," *Nature*, vol. 358, no. 565, 1992.

[4] C. W. Hsu, B. Zhen, S. L. C. J. Lee, S. G. Johnson, J. D. Joannopoulos, , and M. Soljačić, "Observation of trapped light within the radiation continuum," *Nature*, vol. 499, no. 188, 2013.

[5] C. W. Hsu, B. Zhen, A. D. Stone, J. D. Joannopoulos, and M. Soljačić, "Bound states in the continuum," *Nat. Rev. Mater.*, vol. 1, no. 16048, 2016.

[6] B. Z. J. Lee, S. L. Chua, W. Qiu, J. D. Joannopoulos, M. Soljačić, and O. Shapira, "Observation and differentiation of unique high-q optical resonances near zero wave vector in macroscopic photonic crystal slabs," *Phys. Rev. Lett.*, vol. 109, no. 067401, 2012.

[7] D. C. Marinica, A. G. Borisov, and S. V. Shabanov, "Bound states in the continuum in photonics," *Phys. Rev. Lett.*, vol. 100, no. 183902, 2008.

[8] M. I. Molina, A. E. Miroshnichenko, and Y. S. Kivshar, "Surface bound states in the continuum," *Phys. Rev. Lett.*, vol. 108, no. 070401, 2012.

[9] Y. Plotnik, O. Peleg, F. Dreisow, M. Heinrich, S. Nolte, A. Szameit, and M. Segev, "Experimental observation of optical bound states in the continuum," *Phys. Rev. Lett.*, vol. 107, no. 183901, 2011.

[10] I. Hrebikova, L. Jelinek, and M. G. Silveirinha, "Embedded energy state in an open semiconductor heterostructure," *Phys. Rev. B*, vol. 92, no. 155303, 2015.

[11] S. Lannebère and M. G. Silveirinha, "Optical meta-atom for localization of light with quantized energy," *Nat. Commun.*, vol. 6, no. 8766, 2015.

[12] M. G. Silveirinha, "Trapping light in open plasmonic nanostructures," *Phys. Rev. A*, vol. 89, no. 023813, 2014.

[13] I. Liberal and N. Engheta, "Nonradiating and radiating modes excited by quantum emitters in open epsilon-near-zero cavities," *Sci. Adv.*, vol. 2, no. e1600987, 2016.

[14] F. Monticone and A. Alù, "Embedded photonic eigenvalues in 3d nanostructures," *Phys. Rev. Lett.*, vol. 112, no. 213903, 2014.

[15] A. Alù, M. G. Silveirinha, A. Salandrino, and N. Engheta, "Epsilon-near-zero metamaterials and electromagnetic sources: Tailoring the radiation phase pattern," *Phys. Rev. B*, vol. 75, no. 155410, 2007.

[16] N. Engheta, "Pursuing near-zero response," *Science*, vol. 340, no. 286, 2013.

[17] M. G. Silveirinha and N. Engheta, "Tunneling of electromagnetic through subwavelength channels and bends using ε-near-zero materials," *Phys. Rev. Lett.*, vol. 97, no. 157403, 2006.

[18] M. G. Silveirinha and N. Engheta, "Transporting an image through a subwavelength hole," *Phys. Rev. Lett.*, vol. 102, no. 103902, 2009.

[19] I. Liberal and N. Engheta, "Zero-index platforms: where light defies geometry," *Optical Photonic News*, vol. 27, pp. 26–33, 2016.

[20] I. Liberal, A. M. Mahmoud, and N. Engheta, "Geometry-invariant resonant cavities," *Nat. Commun.*, vol. 7, no. 10989, 2016.

[21] C. GmbH, "2016 cst microwave studio."

[22] B. Luk'yanchuk, N. I. Zheludev, S. A. Maier, N. J. Halas, P. Nordlander, H. Giessen, and C. T. Chong, "The fano resonance in plasmonic nanostructures and metamaterials," *Nat. Mat.*, vol. 9, no. 707, 2010.

[23] R. W. Boyd, *Nonlinear Optics, Third ed.* New York: Academic Press.

CHAPTER 3

Impact of nonlocal effects on embedded eigenstates

3.1   Introduction

The light trapping studies done in chapter 2 and in Refs. [1–7] assumed that the plasmonic ENZ shell of the meta-atom had a local response, i.e., the material permittivity was assumed independent of the spatial variation of the fields. Possible effects of spatial dispersion were only superficially discussed in [1]. In metals the nonlocal effects arise primarily due to many-body electron-electron (repulsive-type) interactions, and are usually modelled through a diffusion-term in the framework of the hydrodynamic model [5, 8–17]. Nonlocal effects may be critically important in plasmonics, especially for nanosized particles [5, 8–19]. Thus, one might think that spatial dispersion would be an additional obstacle to create embedded eigenstates. Surprisingly, we prove in this chapter that it is precisely the opposite, and that nonlocal effects offer a unique path to localize light in an open resonator. It is shown that the conditions for the observation of embedded eigenstates are very much relaxed when nonlocal effects are taken into account; in particular, the shell permittivity is not anymore constrained to be precisely zero.

   This chapter is organized as follows. In Sect. 3.2, we describe the electro-magnetic fields in space of the nonlocal meta-atom using Mie theory and use hydrodynamic model to characterize the nonlocal effects on the shell. Using classical and additional boundary conditions, we find the characteristic

equation for the bound states. We then calculate the embedded eigenstates allowed solutions in function of several geometrical parameters of the particle. In Sect. 3.3, we study the electromagnetic response of the core-shell particle under an external excitation. In Sect. 3.4, we analyze the reasons why it is still possible to have trapped states with infinite lifetimes in core-shell plasmonic particles with nonlocal effects. Finally, in Sect. 3.5 the main conclusions are drawn.

3.2 Natural modes of the spatially dispersive plasmonic core-shell nanoparticle

Figure 3.1(a) illustrates the geometry of the core-shell meta-atom. It consists of a bi-layered spherical nanoparticle standing in air. The core region and the outer shell have radii R_1 and R_2, respectively. The core material is a simple dielectric with relative permittivity ε_1, e.g., air, and the shell is made of a plasmonic material, e.g., a noble or alkali metal at optical frequencies or a semiconductor in the terahertz regime. The unbounded plasmonic material supports three plane-wave modes with a spatial dependence of the type $e^{i\mathbf{k}\cdot\mathbf{r}}$: two transverse waves and also a longitudinal wave [5, 15].

Due to the spherical symmetry, the natural modes of the core-shell nanoparticle (Fig. 3.1(a)) can be split into transverse radial magnetic (TM^r) and transverse radial electric (TE^r) waves. We focus on the TM^r modes whose properties are determined by the hybridization of transverse and longitudinal waves. Using Mie theory [20, 21] the electromagnetic fields may be written in all the regions of space in terms of spherical Bessel functions [1]. Our analysis relies on the hydrodynamic (or drift-diffusion) model [5] that takes into account the nonlocal effects in the plasmonic shell. The hydrodynamic model couples the Maxwell's equations and the continuity equation

$$\nabla \times \mathbf{E} = -\mu_0 \partial_t \mathbf{H}, \quad \nabla \times \mathbf{H} = \mathbf{j} + \varepsilon_0 \varepsilon_\infty \partial_t \mathbf{E}, \tag{3.1a}$$

$$\partial_t \rho = -\nabla \cdot \mathbf{j} \tag{3.1b}$$

with the Navier-Stokes equation that governs the electron transport

$$\partial_t \mathbf{j} = \varepsilon_0 \omega_p^2 \mathbf{E} - \omega_c \mathbf{j} - \beta^2 \nabla \rho. \tag{3.2}$$

38

In the above, ρ is the charge density and $\mathbf{j}$ the current density. In the spectral domain ($\partial_t = -i\omega$ and $\nabla = i\mathbf{k}$) the current density $\mathbf{j}$ can be expressed in terms of the electric field. The effective permittivity of the shell electron gas ($\bar{\varepsilon}_2$) is defined such that $\mathbf{j} - i\omega\varepsilon_0\varepsilon_\infty\mathbf{E} = -i\omega\varepsilon_0\bar{\varepsilon}_2 \cdot \mathbf{E}$. As is well-known, it is of the form:

$$\bar{\varepsilon}_2 = \varepsilon_{2,\mathrm{T}}\left(\mathbf{1} - \frac{1}{k^2}\mathbf{k} \otimes \mathbf{k}\right) + \varepsilon_{2,\mathrm{L}}\frac{1}{k^2}\mathbf{k} \otimes \mathbf{k}, \qquad (3.3\mathrm{a})$$

$$\varepsilon_{2,\mathrm{T}}(\omega) = \varepsilon_\infty - \frac{\omega_\mathrm{p}^2}{\omega(\omega + i\omega_\mathrm{c})}, \quad \varepsilon_{2,\mathrm{L}}(\mathbf{k},\omega) = \varepsilon_\infty - \frac{\omega_\mathrm{p}^2}{\omega(\omega + i\omega_\mathrm{c}) - \beta^2 k^2}. \quad (3.3\mathrm{b})$$

The transverse permittivity $\varepsilon_{2,\mathrm{T}}$ associated with the transverse waves follows the Drude-type dispersion model, with ω_p the plasma frequency, ω_c the collision frequency and ε_∞ is the high-frequency relative permittivity. The longitudinal permittivity $\varepsilon_{2,\mathrm{L}}$ associated with the longitudinal wave [5] depends explicitly on the wave-vector ($\nabla = i\mathbf{k}$). The dispersion of the longitudinal wave is determined by $k^2 = \frac{1}{\beta^2}\left[\omega(\omega + i\omega_\mathrm{c}) - \frac{\omega_\mathrm{p}^2}{\varepsilon_\infty}\right]$, where $\beta^2 = 3/5 v_\mathrm{F}^2$ and v_F is the Fermi velocity [12,13]. The nonlocality strength parameter β/c may reach values on the order of $1/450$ in alkali metals [8], $1/280$ in semiconductors [17], and even larger values in metamaterials [22,23]. For simplicity, except if explicitly mentioned otherwise, it is assumed in the paper that $\varepsilon_\infty = 1$.

For the geometry of the main text and TM_n^r-polarized waves, the electromagnetic field in the plasmonic shell is a superposition of the transverse and longitudinal waves such that [1, 13]

$$\mathbf{E} = \mathbf{E}_\mathrm{T} + \mathbf{E}_\mathrm{L} = \nabla \times \nabla \times \{\mathbf{r}\Psi_\mathrm{T}(r)Y_n(\hat{\mathbf{r}})\} + \nabla\{\Psi_\mathrm{L}(r)Y_n(\hat{\mathbf{r}})\}, \qquad (3.4)$$

$$\mathbf{H} = +i\omega\varepsilon_0\varepsilon_{2,\mathrm{T}}\Psi_\mathrm{T}(r)\hat{\mathbf{r}} \times \mathrm{Grad}Y_n(\hat{\mathbf{r}}), \qquad (3.5)$$

where Y_n is a spherical harmonic of order n and Grad is the surface gradient operator.
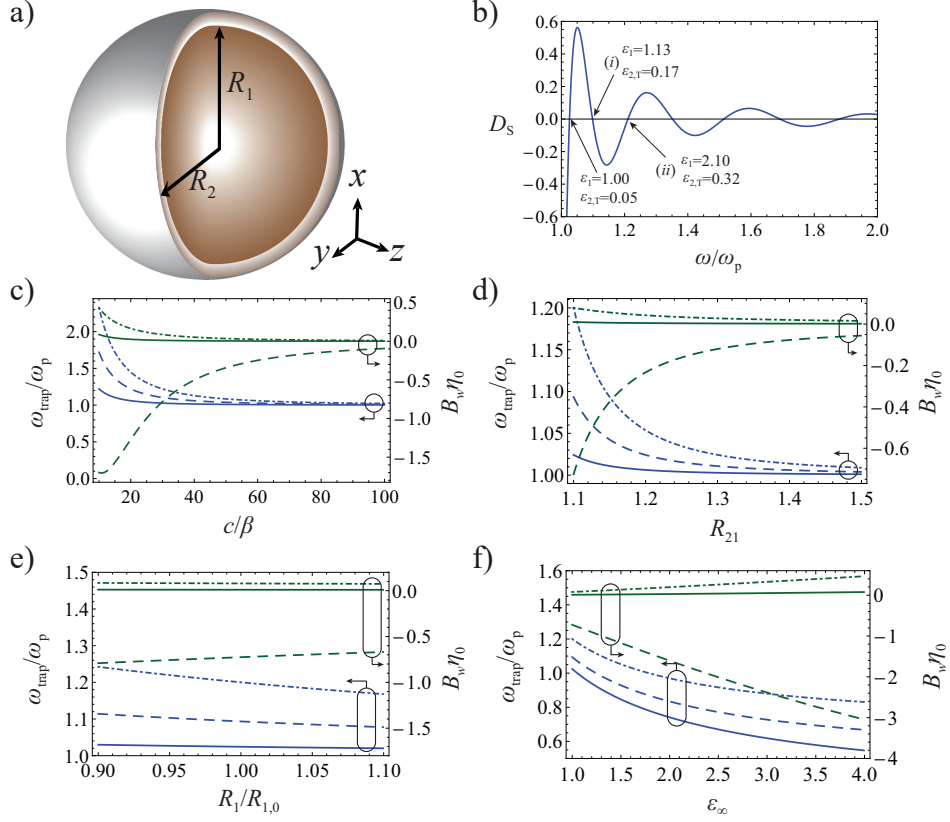
Figure 3.1: (a) Geometry of the open bounded bi-layered spherical meta-atom. The shell is made of a plasmonic spatially-dispersive material. (b) Characteristic function D_S as a function of frequency, for a meta-atom with $\beta/c = 1/10^{3/2}$, $R_{21} = 1.1$, $R_1 = 0.973R_{10}$ and $\omega_c = 0$. The zeros indicate the values of the frequencies $\omega_{trap}^{(j)}$. The insets give the values of the core permittivity ε_1 and of the shell transverse permittivity $\varepsilon_{2,T}$ for the first three solutions. (c)-(f) Embedded eigenstate frequency (blue lines) and susceptance at the core interface (green lines) as a function of the (c) locality strength c/β, (d) normalized shell radius $R_{21} = R_2/R_1$, (e) normalized core radius $R_1/R_{1,0}$ and (f) high-frequency relative permittivity ε_∞. The susceptance is normalized to the free-space impedance η_0. The solid, dashed, and dot-dashed curves correspond to the $j = 1, 2, 3$ solution branches, respectively. The structural parameters are $c/\beta = 1/10^{3/2}$, $\omega_c = 0$, $R_{21} = 1.1$, $R_1/R_{1,0} = 1$ and $\varepsilon_\infty = 1$ except when one of the parameters is shown in the horizontal axis of a plot.

40

The functions Ψ_T and Ψ_L are the transverse and longitudinal potentials, respectively, and satisfy a spherical Bessel equation. For natural modes of oscillation they are given by

$$\Psi_T = \begin{cases} Aj_n(k_1 r) & , \quad r < R_1 \\ B_{1T}j_n(k_T r) + B_{2T}y_n(k_T r) & , \quad R_1 < r < R_2 , \\ Ch_n^{(1)}(k_0 r) & , \quad r > R_2 \end{cases} \qquad (3.6)$$

$$\Psi_L = \begin{cases} B_{1L}j_n(k_L r) + B_{2L}y_n(k_L r) & , \quad R_1 < r < R_2 \\ 0 & , \quad otherwise \end{cases} , \qquad (3.7)$$

with $k_0 = \omega/c$, $k_1 = \sqrt{\varepsilon_1}\omega/c$, $k_T = \sqrt{\varepsilon_{2,T}}\omega/c$ and $k_L^2 = \frac{1}{\beta^2}\left[\omega(\omega + i\omega_c) - \frac{\omega_p^2}{\varepsilon_\infty}\right]$. The coefficients A, B_{1T}, B_{2T}, B_{1L}, B_{2L} and C must ensure i) the continuity of the tangential components of the electromagnetic field and ii) that there is no electric charge flow through the shell interfaces $\hat{\mathbf{n}}\cdot\mathbf{j} = 0$. The latter constraint is the so called "additional boundary condition". From these conditions, we obtain a homogeneous linear system of equations of the form $\mathbf{M}\cdot\mathbf{x} = 0$ with $\mathbf{x} = (A, B_{1T}, B_{2T}, B_{1L}, B_{2L}, C)^T$ and

$$\mathbf{M} = \begin{pmatrix} -[j_n(k_1 r)r]'_{r=R_1} & [j_n(k_T r)r]'_{r=R_1} & [y_n(k_T r)r]'_{r=R_1} & j_n(k_L R_1) & y_n(k_L R_1) & 0 \\ -\varepsilon_1 j_n(k_1 R_1) & \varepsilon_{2,T}j_n(k_T R_1) & \varepsilon_{2,T}y_n(k_T R_1) & 0 & 0 & 0 \\ 0 & qj_n(k_T R_1) & qy_n(k_T R_1) & k_L R_1 j_n'(k_L R_1) & k_L R_1 y_n'(k_L R_1) & 0 \\ 0 & qj_n(k_T R_2) & qy_n(k_T R_2) & k_L R_2 j_n'(k_L R_2) & k_L R_2 y_n'(k_L R_2) & 0 \\ 0 & [j_n(k_T r)r]'_{r=R_2} & [y_n(k_T r)r]'_{r=R_2} & j_n(k_L R_2) & y_n(k_L R_2) & -[h_n^{(1)}(k_0 r)r]'_{r=R_2} \\ 0 & \varepsilon_{2,T}j_n(k_T R_2) & \varepsilon_{2,T}y_n(k_T R_2) & 0 & 0 & -\varepsilon_0 h_n^{(1)}(k_0 R_2) \end{pmatrix}$$

$$(3.8)$$

with $q = (1 - \varepsilon_{2,T})n(n+1)$ [1]. The nontrivial solutions $\omega = \omega' + i\omega''$ (with $\omega'' \leq 0$) of the characteristic equation $D(\omega, R_1, \varepsilon_1, R_2, \omega_p, \beta) \equiv det(\mathbf{M}) = 0$ are the natural frequencies of oscillation of the system.

We also introduce a reduced characteristic system ($\mathbf{M}_S \cdot \widetilde{\mathbf{x}} = 0$ with $\widetilde{\mathbf{x}} = (B_{1T}, B_{2T}, B_{1L}, B_{2L})^T$) obtained by imposing that the tangential electromagnetic field components vanish at the outer interface $r = R_2^-$ [1], and that the additional boundary condition $\hat{\mathbf{n}}\cdot\mathbf{j} = 0$ is satisfied at the inner ($r = R_1^+$) and outer ($r = R_2^-$) interfaces. The relevant matrix is:

$$
\mathbf{M_S} =
\begin{pmatrix}
qj_n(k_T R_1) & qy_n(k_T R_1) & k_L R_1 j_n'(k_L R_1) & k_L R_1 y_n'(k_L R_1) \\
qj_n(k_T R_2) & qy_n(k_T R_2) & k_L R_2 j_n'(k_L R_2) & k_L R_2 y_n'(k_L R_2) \\
[j_n(k_T r)r]'_{r=R_2} & [y_n(k_T r)r]'_{r=R_2} & j_n(k_L R_2) & y_n(k_L R_2) \\
\varepsilon_{2,T} j_n(k_T R_2) & \varepsilon_{2,T} y_n(k_T R_2) & 0 & 0
\end{pmatrix}.
$$

(3.9)

The zeros of $D_S \equiv det(\mathbf{M_S}) = 0$ in ω determine the frequencies for which a given shell can support embedded eigenstates.

For each solution of $D_S = 0$, we introduce a transverse admittance Y_w^+ that links the fields at the inner shell interface $(r = R_1^+)$ as $Y_w^+ \hat{\mathbf{r}} \times \mathbf{E} = \hat{\mathbf{r}} \times (\mathbf{H} \times \hat{\mathbf{r}})$. The transverse admittance is purely imaginary $Y_w^+ = -iB_w$. Using Eqs. (3.4)-(3.5) it is straightforward to show that:

$$
Y_w^+ = \frac{i\omega\varepsilon_0\varepsilon_{2,T}\psi_T(r)}{\frac{1}{r}\{[r\psi_T(r)]' + \psi_L(r)\}}\Big|_{r=R_1}.
$$

(3.10)

From Eqs. (3.6)-(3.7) one obtains the explicit formula:

$$
Y_w^+ \eta_0 = ik_0 R_1 \frac{B_{1T}\varepsilon_{2,T} j_n(k_T R_1) + B_{2T}\varepsilon_{2,T} y_n(k_T R_1)}{B_{1T}[j_n(k_T r)r]'_{r=R_1} + B_{2T}[y_n(k_T r)r]'_{r=R_1} + B_{1L} j_n(k_L R_1) + B_{2L} y_n(k_L R_1)}
$$

(3.11)

In the above, η_0 is the free-space impedance and $(B_{1T}, B_{2T}, B_{1L}, B_{2L})$ is determined by the null space of $\mathbf{M_S}$. On the other hand, from Eq. (3.6), the transverse admittance calculated at the core side of the interface $(r = R_1^-)$ is:

$$
Y_w^- \eta_0 = ik_0 R_1 \frac{\varepsilon_1 j_n(k_1 R_1)}{[rj_n(k_1 r)]'_{r=R_1}}.
$$

(3.12)

An embedded eigenvalue can be formed only when the conditions $D_S = 0$ and $Y^+ = Y^-(\omega, R_1, \varepsilon_1)$ are simultaneously satisfied. In general, there are multiple allowed solutions for ε_1.

In the local limit $(\beta = 0)$, i.e., for an electron gas with non-interacting electrons, it is known from Ref. [1] that the embedded eigenstates can occur only if the shell has a zero-permittivity, i.e., $\varepsilon_2 = 0$ is a mandatory condition. Thus, the oscillation frequency of a trapped state is necessarily $\omega = \omega_p$. An $\varepsilon_2 = 0$ shell behaves as a perfect magnetic (PMC) wall for TM^r waves. The embedded eigenstates are formed when $\omega = \omega_p$ coincides

with an eigenfrequency of the equivalent PMC resonator, i.e., the core surrounded by a fictitious PMC boundary. For an embedded eigenstate with dipolar-type symmetry, this condition leads to the geometrical constraint $R_1 = R_{1,0} \equiv 4.49c/(\omega_{\mathrm{p}}\sqrt{\varepsilon_1})$ [1].

In general, for a spatially dispersive shell, the embedded eigenstates are solutions of $D = 0$ with a real-valued ω so that the oscillations do not decay with time. The simplest way to understand the general structure of the solutions and to generate them is by using the reduced dispersion equation $D_{\mathrm{S}} = 0$. Remarkably, it turns out that in the lossless limit the solutions of the reduced equation $D_{\mathrm{S}} = 0$ consist of an *infinite* number of branches $\omega = \omega_{\mathrm{trap}}^{(j)}(R_1, R_2, \omega_{\mathrm{p}}, \beta)$, $j = 1, 2, 3,...$ (see Fig. 3.1(b)). This implies that a nonlocal plasmonic shell with a given geometry may support *multiple* embedded eigenstates, rather than a unique bound state as in the local case [1]. This finding is contrary to common sense as the nonlocal effects are rooted in repulsive electron-electron interactions, which intuitively should act against light localization. Curiously, it was shown in [24] that the nonlocal effects in thin metal slabs may not adversely affect other type of plasmonic phenomena.

As mentioned above, the core permittivity ε_1 needs to be precisely tuned to ensure that $Y_w^+ = Y_w^-(\omega, R_1, \varepsilon_1)$. The insets of Fig. 3.1(b) show the values of $(\varepsilon_1, \varepsilon_{2,T})$ for the first three allowed eigenfrequencies. The insets of Fig. 3.1(b) show the values of $(\varepsilon_1, \varepsilon_{2,\mathrm{T}})$ for the first three allowed eigenfrequencies. We choose solutions characterized by $\varepsilon_1 \geq 1$ (there are many solutions for ε_1 both in the local and in the nonlocal cases). The multiplicity of eigenfrequencies is a consequence of the extra degrees of freedom provided by the nonlocal response and gives the opportunity to trap light at frequencies considerably far from ω_{p}. Different from the local case, when $\beta \neq 0$ the condition $\omega = \omega_{\mathrm{trap}}^{(j)}$ does not lead to a zero permittivity, i.e., $\varepsilon_{2,\mathrm{T}} \neq 0$ (the longitudinal permittivity is also nontrivial due to the wave-vector dependence).

Figures 3.1(c)-(f) depict the numerically calculated oscillation frequency (ω_{trap}) and the corresponding wave susceptance (B_w) for the first three branches of solutions and for fields with a dipolar-type structure (TM_n^r mode with $n = 1$), as a function of the different geometrical and material parameters of the meta-atom. Figure 3.1(c) shows that for a strong spatial dispersion (small values of c/β), ω_{trap} and B_w may differ considerably from the corresponding local values ω_{p} and 0. Note that in the local regime, one has $Y_w^+ \equiv 0$, which corresponds to a PMC boundary. As the nonlocality strength decreases ($c/\beta \to \infty$), and thereby the response of the

plasmonic shell becomes increasingly local, the frequency of oscillation of the embedded eigenstate approaches ω_p. The sign of B_w alternates from branch to branch and is positive for the first and third branches (solid and dot-dashed curves) and negative for the second branch (dashed curve). The deviations from the local case are more significant for the higher order solution branches. Figure 3.1(d) illustrates the variation of ω_{trap} and B_w with the normalized shell radius $R_{21} = R_2/R_1$, for a fixed value of the nonlocality strength, $\beta/c = 1/10^{3/2} = 1/31.62$ (we use a large value of β/c to illustrate more clearly the impact of the spatial dispersion). The nonlocal effects are stronger, i.e., the frequency detuning $\omega_{\text{trap}} - \omega_p$ is larger, when the plasmonic shell is thinner. Figure 3.1(e) depicts the variation of ω_{trap} and B_w with the normalized core radius $R_1/R_{1,0}$. Results reveal that the frequency detuning $\omega_{\text{trap}} - \omega_p$ is larger when the meta-atom is smaller. Finally, in Fig. 3.1(f) we have the variation of ω_{trap} and B_w with the high-frequency relative permittivity ε_∞, in which we see that ω_{trap} is shifted to lower frequencies with an increase of ε_∞.
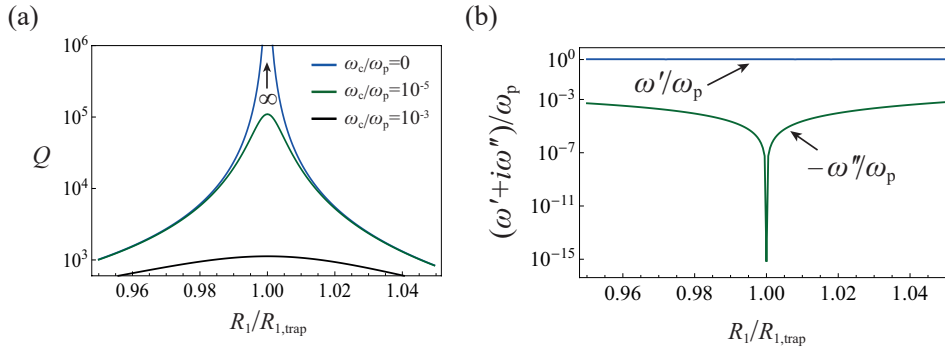

Figure 3.2: (a) Quality factor (for the dipolar mode) as a function of the normalized core radius $R_1/R_{1,\text{trap}}$, for different values of the material loss in the plasmonic shell. (b) Variation of the real ω' and imaginary ω'' parts of the eigenmode frequency $\omega = \omega' + i\omega''$ with $R_1/R_{1,\text{trap}}$, for a lossless plasmonic shell $(\omega_c/\omega_p = 0)$. The structural parameters are $c/\beta = 1/10^{3/2}$, $R_{21} = 1.1$, $\varepsilon_\infty = 1$. The quality factor diverges to infinity when $R_1 = R_{1,\text{trap}} = 0.973 R_{1,0}$ which yields $\omega = \omega_{\text{trap}} = 1.026\omega_p$.

For a specific design example, we pick $\varepsilon_1 = 1$, $R_{21} = 1.1$ and $\beta/c = 1/10^{3/2}$ and solve $D = 0$ with respect to (ω, R_1) real-valued. We obtain

$R_{1,\mathrm{trap}} = 0.973R_{1,0}$ and $\omega_{\mathrm{trap}} = 1.026\omega_{\mathrm{p}}$ in the 1st branch of solutions (1st zero of Fig. 3.1(b)). The quality factor of this meta-atom is depicted in Fig. 3.2(a) for a detuned core radius and different values of the shell material loss. Similar to the local problem [1], for a tuned resonator ($R_1 = R_{1,\mathrm{trap}}$) the quality factor diverges to infinity ($Q \to \infty$) when the material loss is suppressed ($\omega_{\mathrm{c}} \to 0$), but in the nonlocal case for a frequency $\omega = \omega_{\mathrm{trap}} \neq \omega_{\mathrm{p}}$. Evidently, when the material response is dissipative, the quality factor and the oscillation lifetime are finite. Figure 3.2(b) illustrates how the complex resonance frequency $\omega = \omega' + i\omega''$ varies with the core radius for a lossless material. As expected, when the core radius matches $R_{1,\mathrm{trap}}$ the oscillation frequency becomes real-valued, and the radiation loss is fully suppressed.

Figure 3.3(a) shows the electromagnetic field distribution (solid lines) of the embedded eigenstate with $R_{1,\mathrm{trap}} = 0.973R_{1,0}$ and $\omega_{\mathrm{trap}} = 1.026\omega_{\mathrm{p}}$. The dashed lines represent the profile of the embedded eigenstate in a meta-atom without spatial dispersion ($\omega_{\mathrm{trap}} = \omega_{\mathrm{p}}$ and $R_{1,\mathrm{trap}} = R_{1,0}$). From Fig. 3.3(a), one can see that the electron-electron interactions in the plasmonic shell affect weakly the electromagnetic field distributions of the trapped field in the core region ($r < R_1$). In contrast, the fields in the plasmonic shell ($1 < r/R_1 < 1.1$) are strongly perturbed by the nonlocality. Most strikingly, the radial component of the electric field in the shell (see the curve $|E_r|_{y=0}$ in Fig. 3.3(a)) becomes continuous at the boundaries because the charge diffusion effects prevent the localization of a surface charge density at the interfaces. Both the local and the nonlocal models predict a strong enhancement of the radial electric field in the plasmonic shell, which is a clear fingerprint of the excitation of volume-plasmon-type oscillations. Furthermore, Fig. 3.3(b) reveals that the magnetic field in the spatially dispersive shell, albeit small is nontrivial. Thus, the embedded eigenstate results from the hybridization of transverse (with $\nabla \cdot \mathbf{E} = 0$) and longitudinal (with $\nabla \cdot \mathbf{E} \neq 0$) waves in the shell. Quite differently, in the local case the embedded eigenstate has a vanishing magnetic field in the shell and hence is purely longitudinal ($\nabla \cdot \mathbf{E} \neq 0$) [1]. Figure 3.3(d) shows time snapshots of the radial $E_r(t = 0)$ electric field and of the z-component $H_z(t = 0)$ of the magnetic field obtained using the nonlocal model. The dipolar structure of the field in the core is evident; the electric dipole moment is oriented along x and the fields have symmetry of revolution around the x-axis. Note that due to the symmetry of the system the eigenmode is triply degenerate.
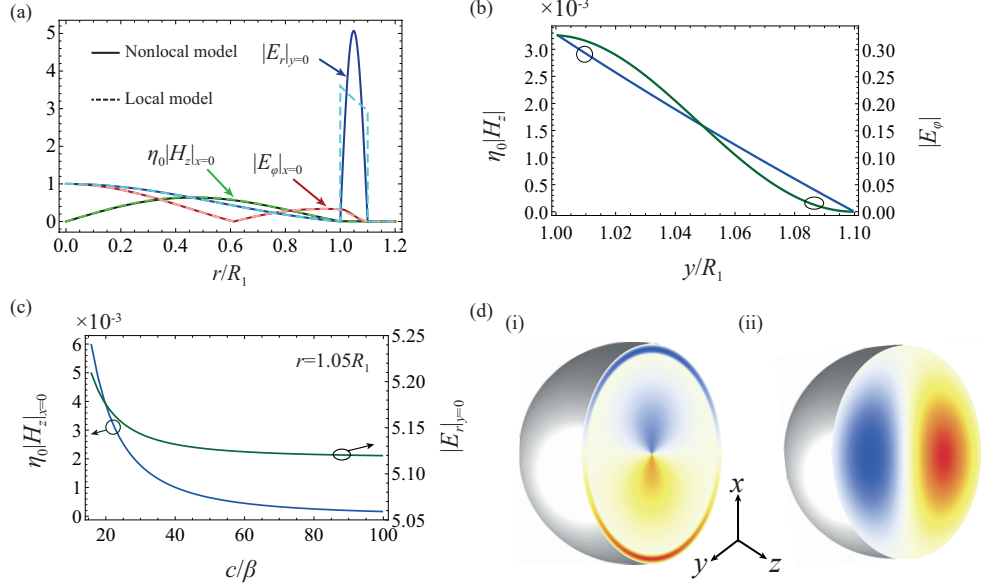
Figure 3.3: Electromagnetic fields of an embedded eigenstate. (a) Field amplitudes in the core-shell resonator (normalized to the electric field at the core center, $r = 0$) as a function of the radial distance in the xoy plane, calculated using the local (dashed lines) and the nonlocal models (solid lines). Local model results: $c/\beta \to \infty$, $\omega_{\text{trap}} = \omega_{\text{p}}$, and $R_{1,\text{trap}} = R_{1,0}$; Nonlocal model results: $c/\beta = 1/10^{3/2}$, $\omega_{\text{trap}} = 1.026\omega_{\text{p}}$ and $R_{1,\text{trap}} = 0.973R_{1,0}$. (b) Zoom of $\eta_0|H_z|$ (blue) and $|E_\phi|$ (green) in the shell for the nonlocal case. (c) $\eta_0|H_z|_{x=0}$ (blue) and $|E_r|_{y=0}$ (green) as a function of c/β at center of the shell ($r = 1.05R_1$). (d) Time snapshots of the electric field in the nonlocal meta-atom: (i) $|E_r|(t = 0)$ and (ii) $|H_z|(t = 0)$ in the xoy plane. In all the panels, $R_{21} = 1.1$, $\varepsilon_1 = 1$, and $\omega_{\text{c}} = 0$.

46

Figure 3.3(c) depicts the amplitude of the embedded eigenstate fields in the plasmonic shell center as a function of c/β; the values of $R_{1,\mathrm{trap}}$ and ω_{trap} are recalculated for each c/β. Clearly, as the nonlocality strength increases (smaller values of c/β), the amplitudes of the magnetic field and of the radial electric field in the shell are enhanced. For $\beta \to 0$ the magnetic field in the shell approaches zero.

Figures 3.4(a) and (b) show the electromagnetic field profiles in the shell for the second and third solutions of Fig. 3.1(b), respectively. The electric field profiles of the higher order modes are characterized by an increased number of maxima and nulls as compared to the first (fundamental) mode shown in Fig. 3.3(a). The fields in the core are similar to those of the fundamental mode (not shown).
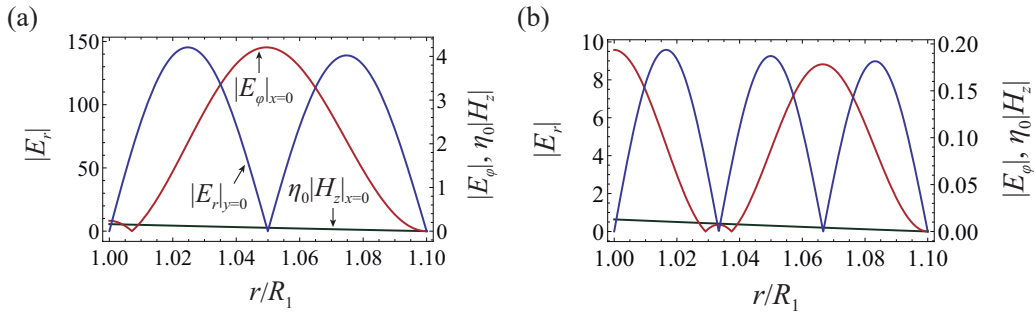
Figure 3.4: (a)-(b) Spatial variation of the electromagnetic fields in the shell (cut in the *xoy* plane) for the modes labeled (*i*) and (*ii*) in Fig. 1b), respectively. The right vertical axis is used for $\eta_0|H_z|_{x=0}$ and $|E_\phi|_{x=0}$, and the left vertical axis for $|E_r|_{y=0}$.

3.3 Scattering by a spatially dispersive plasmonic core-shell nanoparticle under external excitation

To study the electromagnetic response of the core-shell particle under an external excitation, we consider the problem of plane wave scattering with the electric field linearly polarized. The meta-atom parameters are as in

Fig. 3.3(a). The Mie scattering coefficients for plane wave incidence can be found by expanding the fields in spherical harmonics, similar to the previous section. To take into account the incident wave, the function Ψ_T must be modified as

$$\Psi_\mathrm{T} = \begin{cases} A j_n(k_1 r) & r < R_1 \\ B_{1\mathrm{T}} j_n(k_\mathrm{T} r) + B_{2\mathrm{T}} y_n(k_\mathrm{T} r) & R_1 < r < R_2 \\ C h_n^{(1)}(k_0 r) + \frac{1}{ik_0} j_n(k_0 r) & r > R_2 \end{cases} \qquad (3.13)$$

In the above, $a_n \to ik_1 A$ and $c_n \to ik_0 C$ are the standard Mie coefficients in the core and the air regions, respectively. Applying the same boundary conditions as done in the previous section, one obtains a linear system of equations of the form $\mathbf{M} \cdot \mathbf{x} = \mathbf{b}$, where $\mathbf{M}$ is given by the matrix (3.8) and $\mathbf{b}$ is the vector:

$$\mathbf{b} = \frac{1}{ik_0} \begin{pmatrix} 0 & 0 & 0 & 0 & [j_n(k_0 r) r]'_{r=R_2} & j_n(k_0 R_2) \end{pmatrix}^T. \qquad (3.14)$$

Figure 3.5(a) depicts the absolute value of the Mie coefficient in the core region $|a_1^{\mathrm{TM}}|$ as a function of frequency and for three different values of the core radius R_1. When R_1 is detuned from the optimal value $R_{1,\mathrm{trap}}$, the Mie coefficient has a resonant behavior with a Fano-type line shape. In contrast, when R_1 exactly matches R_1, $|a_1^{\mathrm{TM}}| \approx 1$ has no resonant features due to a pole-zero cancellation rooted in the reciprocity of the system [1]. The reciprocity constraint can be circumvented with a nonlinear material response [4]. Specifically, with a nonlinearity the embedded eigenstates can be pumped from the outside, ensuring that the energy stored in the resonator is precisely quantized [4] (see also [25–28]). Figure 3.5(b) shows that the Mie coefficient in the air region c_1^{TM} has a behavior analogous to a_1^{TM}.

3.4 Theoretical insights and justifications for the embedded eigenstates in the nonlocal meta-atom

The emergence of embedded eigenstates in plasmonic nanostructures is a quite unique effect. Indeed, it is fundamentally impossible to localize light in any spatially bounded (inhomogeneous) structure formed by transparent
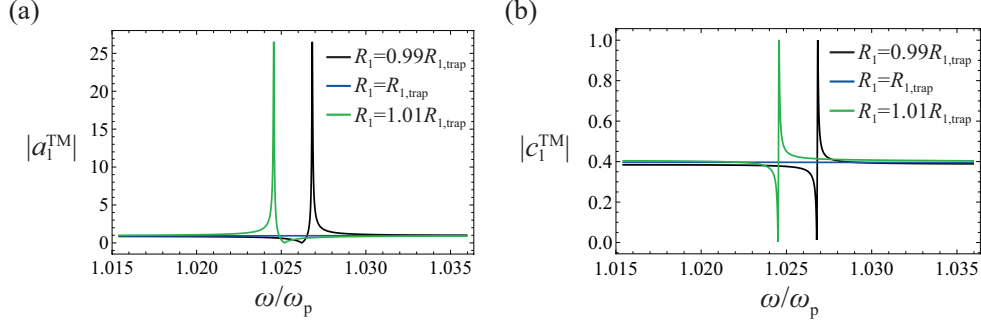
(a)

(b)

Figure 3.5: . (a) Mie coefficient $|a_1^{\mathrm{TM}}|$ in the core region and (b) Mie coefficient $|c_1^{\mathrm{TM}}|$ in the air region as a function of the normalized frequency $\omega/\omega_{\mathrm{p}}$ and for three different values of the core radius. The meta-atom parameters are $c/\beta = 1/10^{3/2}$, $R_{21} = 1.1$, $\varepsilon_1 = 1$, and $\omega_{\mathrm{c}} = 0$. The embedded eigenstate is characterized by $\omega_{\mathrm{trap}} = 1.026\omega_{\mathrm{p}}$ and $R_{1,\mathrm{trap}} = 0.973R_{1,0}$.

local isotropic dielectrics with $\varepsilon \neq 0$ and $\mu \neq 0$ [1]. Next we unveil the reason why spatially dispersive materials are less constrained than local materials. In particular, we present two different justifications.

The first key point is that the electromagnetic field of a TM^r mode in the nonlocal shell is a superposition of two counter-propagating transverse waves and two counter-propagating longitudinal waves; hence, for a given spherical harmonic order there are $2 + 2 = 4$ degrees of freedom. In order that the radiation loss is suppressed, the electromagnetic fields outside the core-shell nanoparticle must vanish. Thus, both the tangential electromagnetic fields and the normal component of the electric current $(\hat{\mathbf{n}} \cdot \mathbf{j})$ must vanish at the shell outer interface, which corresponds to $1 + 1 + 1 = 3$ scalar homogeneous boundary conditions. Evidently, there is a remaining degree of freedom $(4 - 3 = 1)$, and thereby the homogeneous boundary conditions at the outer interface do not automatically force $(\mathbf{E}, \mathbf{H})$ to vanish in the shell when $\omega \neq \omega_{\mathrm{p}}$. In contrast, in the local limit there are only 2 degrees of freedom associated with the TM^r transverse waves. In this case, the boundary conditions at the outer shell interface require the continuity of the tangential components of the fields, which correspond to 2 scalar equations. For homogeneous boundary conditions there are no extra degrees of freedom, and thus, in the local case the fields in the shell are necessarily trivial and it is fundamentally impossible to have embedded eigenstates with $\varepsilon_2 \neq 0$ [1].

49

A more general argument is presented next. In the lossless limit, the hydrodynamic model [Eqs. (3.1a), (3.1b) and (3.2)] can be written in a compact form as

$$\mathbf{M}_g \cdot i\partial_t \mathbf{Q} = \hat{L} \cdot \mathbf{Q}, \tag{3.15}$$

where $\mathbf{Q} = (\mathbf{E}, \mathbf{H}, \tilde{\mathbf{j}}, \tilde{\rho})^T$ represents a ten-component state vector with $\tilde{\mathbf{j}} = \mathbf{j}/\sqrt{\varepsilon_0 \omega_{\mathrm{p}}^2}$ and $\tilde{\rho} = \rho\beta/\sqrt{\varepsilon_0 \omega_{\mathrm{p}}^2}$. Here, is a first-order linear-differential Hermitian operator defined as

$$\hat{L} = \begin{pmatrix} \mathbf{0} & i\nabla \times \mathbf{1} & -i\sqrt{\varepsilon_0 \omega_{\mathrm{p}}^2}\mathbf{1} & 0 \\ -i\nabla \times \mathbf{1} & \mathbf{0} & \mathbf{0} & 0 \\ i\sqrt{\varepsilon_0 \omega_{\mathrm{p}}^2}\mathbf{1} & \mathbf{0} & \mathbf{0} & -i\beta\nabla \\ \mathbf{0} & \mathbf{0} & -i\beta\nabla\cdot & 0 \end{pmatrix}, \tag{3.16}$$

where $\mathbf{1}$ is the 3x3 identity matrix and $\mathbf{0}$ is a 3x3 matrix filled with zeros, and $\mathbf{M}_g$ is a material matrix given by

$$\mathbf{M}_g = \begin{pmatrix} \varepsilon_0\mathbf{1} & \mathbf{0} & \mathbf{0} & 0 \\ \mathbf{0} & \mu_0\mathbf{1} & \mathbf{0} & 0 \\ \mathbf{0} & \mathbf{0} & \mathbf{1} & 0 \\ \mathbf{0} & \mathbf{0} & \mathbf{0} & 1 \end{pmatrix}. \tag{3.17}$$

Let us introduce the Green's function $\mathbf{G}$ (for a homogeneous unbounded space) that satisfies $\hat{L} \cdot \mathbf{G} = \omega\mathbf{M}_g \cdot \mathbf{G} + i\delta(\mathbf{r} - \mathbf{r}')\mathbf{1}_g$. Consider now some solution of $\hat{L} \cdot \mathbf{Q} = \omega\mathbf{M}_g \cdot \mathbf{Q}$ defined in the interior of some volumetric region of space V (the plasmonic shell). Let Σ stand for the boundary surface enclosing volume V. The considered function can be trivially extended to all space (with the state vector identical to zero outside V) as the solution of:

$$\hat{L} \cdot \mathbf{Q} = \omega\mathbf{M}_g \cdot \mathbf{Q} + \begin{pmatrix} -i\hat{\mathbf{n}} \times \mathbf{H} \\ i\hat{\mathbf{n}} \times \mathbf{E} \\ i\beta\hat{\mathbf{n}}\tilde{\rho} \\ i\beta\hat{\mathbf{n}} \cdot \tilde{\mathbf{j}} \end{pmatrix} \delta_\Sigma, \tag{3.18}$$

where δ_Σ represents a delta-function type distribution that vanishes outside Σ, which when integrated over all space gives the area of Σ; $\hat{\mathbf{n}}$ is the outward unity normal vector. From the definition of the Green function, we have

$$\mathbf{Q}(\mathbf{r}) = \int_{\Sigma} ds' \mathbf{G}(\mathbf{r} - \mathbf{r}') \cdot \begin{pmatrix} -\hat{\mathbf{n}} \times \mathbf{H}(\mathbf{r}') \\ \hat{\mathbf{n}} \times \mathbf{E}(\mathbf{r}') \\ \beta \hat{\mathbf{n}} \tilde{\rho}(\mathbf{r}') \\ \beta \hat{\mathbf{n}} \cdot \tilde{\mathbf{j}}(\mathbf{r}') \end{pmatrix}. \tag{3.19}$$

Let us consider that Σ (the shell boundary) is formed by external and internal surfaces $\Sigma = \Sigma_{\text{out}} \cup \Sigma_{\text{in}}$. Suppose also that the tangential electromagnetic fields and the normal component of the current vanish at the outer shell boundary, which are the necessary conditions for the formation of an embedded eigenstate. Then, Eq. (3.19) becomes (imposing also that the normal component of the current vanishes at the inner shell interface)

$$\mathbf{Q}(\mathbf{r}) = \int_{\Sigma_{\text{out}}} ds' \mathbf{G}(\mathbf{r} - \mathbf{r}') \cdot \begin{pmatrix} \mathbf{0} \\ \mathbf{0} \\ \beta \hat{\mathbf{n}} \tilde{\rho}(\mathbf{r}') \\ \mathbf{0} \end{pmatrix} + \int_{\Sigma_{\text{in}}} ds' \mathbf{G}(\mathbf{r} - \mathbf{r}') \cdot \begin{pmatrix} -\hat{\mathbf{n}} \times \mathbf{H}(\mathbf{r}') \\ \hat{\mathbf{n}} \times \mathbf{E}(\mathbf{r}') \\ \beta \hat{\mathbf{n}} \tilde{\rho}(\mathbf{r}') \\ 0 \end{pmatrix}. \tag{3.20}$$

Importantly, Eq. (3.20) shows that notwithstanding the homogeneous boundary conditions on the outer surface, the surface integral over Σ_{out} is not suppressed because $\tilde{\rho}|_{\Sigma_{\text{out}}}$ can be nontrivial. Due to this reason, different from the local case discussed in [1], it is not feasible to use analytical continuation arguments to conclude that $\mathbf{Q}$ vanishes inside the shell (volume V). In other words, for layered structures, the state vector $\mathbf{Q}$ can have a contribution from the outer surface, and thereby does not need to vanish in the shell region. This explains why embedded eigenstates can be formed in a wide spectral range when the nonlocality of the shell is taken into account.

Furthermore, Eq. (3.20) can be understood as an homogeneous integral equation with respect to the unknowns $\tilde{\rho}|_{\Sigma_{\text{out}}}$, $\tilde{\rho}|_{\Sigma_{\text{in}}}$, $\hat{\mathbf{n}} \times \mathbf{E}|_{\Sigma_{\text{in}}}$ and $\hat{\mathbf{n}} \times \mathbf{H}|_{\Sigma_{\text{in}}}$ and subject to the constraints $\hat{\mathbf{n}} \times \mathbf{E}|_{\Sigma_{\text{out}}} = 0$ and $\hat{\mathbf{n}} \times \mathbf{H}|_{\Sigma_{\text{out}}} = 0$, $\hat{\mathbf{n}} \cdot \tilde{\mathbf{j}}|_{\Sigma_{\text{out}}} = 0$ and $\hat{\mathbf{n}} \cdot \tilde{\mathbf{j}}|_{\Sigma_{\text{in}}} = 0$. This homogeneous integral equation generalizes the reduced characteristic system discussed in Sect. 3.2. The homogeneous integral equation can have non-trivial solutions only for specific values of ω which depend exclusively on the geometrical shape of the plasmonic resonator, and on ω_{p}, β. Such values of ω determine the frequencies of the allowed embedded eigenstates. Clearly, the spatially dispersive response strongly relaxes the conditions under which the embedded eigenstates can be formed and does not require the material response to be singular in any manner.

3.5   Conclusion

In conclusion, we theoretically demonstrated that multiple embedded eigen-states with suppressed radiation loss may be supported by open spatially-dispersive core-shell meta-atoms. Surprisingly, the nonlocal effects due to electron-electron repulsive interactions do not prevent the emergence of bound states in the continuum. They rather act to strongly relax the material and geometrical conditions required for the formation of light oscillations with infinite lifetimes. Remarkably, the nonlocality enables the same material shell to perfectly screen multiple frequencies. Moreover, the material parameters of the shell do not exhibit any type of singularity. The effect is not restricted to spherical geometries, but can occur in any plasmonic resonator with two or more disjoint interfaces. Even though realistic material loss remains a practical obstacle, in principle it can be compensated using some gain mechanism [29, 30]. Thus, we believe that spatial-dispersion may provide an exciting and novel path for the realization of nanostructures with embedded eigenstates, which can have applications in optical memories and others. Furthermore, our work unveils a novel mechanism to couple radiation with matter without any form of radiation leakage.

Bibliography

[1] M. G. Silveirinha, "Trapping light in open plasmonic nanostructures," *Phys. Rev. A*, vol. 89, p. 023813, 2014.

[2] F. Monticone and A. Alù, "Embedded photonic eigenvalues in 3d nanostructures," *Phys. Rev. Lett.*, vol. 112, p. 213903, 2014.

[3] I. Liberal and N. Engheta, "Nonradiating and radiating modes excited by quantum emitters in open epsilon-near-zero cavities," *Sci. Adv.*, vol. 2, no. 10, p. e1600987, 2016.

[4] S. Lannebère and M. G. Silveirinha, "Optical meta-atom for localization of light with quantized energy," *Nat. Commun.*, vol. 6, p. 8766, 2015.

[5] C. David and F. J. G. de Abajo, "Spatial nonlocality in the optical response of metal nanoparticles," *J. Phys. Chem. C*, vol. 115, no. 40, pp. 19470–19475, 2011.

[6] F. Monticone, H. M. Doeleman, W. D. Hollander, A. F. Koenderink, and A. Alù, "Trapping light in plain sight: Embedded photonic eigenstates in zero-index metamaterials," *Laser Photonics Rev.*, vol. 12, p. 1700220, 2018.

[7] F. Monticone, D. Sounas, A. Krasnok, and A. Alù, "Can a nonradiating mode be externally excited? nonscattering states versus embedded eigenstates," *ACS Photonics*, 2019.

[8] A. R. Melnyk and M. J. Harrison, "Theory of optical excitation of plasmons in metals," *Phys. Rev. B*, vol. 2, no. 835, 1970.

[9] M. Anderegg, B. Feuerbacher, and B. Fitton, "Optically excited longitudinal plasmons in potassium," *Phys. Rev. Lett.*, vol. 27, p. 1565, 1971.

[10] R. Ruppin, "Optical properties of small metal spheres," *Phys. Rev. B*, vol. 11, p. 2871, 1975.

[11] R. Ruppin, "Mie theory with spatial dispersion," *Opt. Commun.*, vol. 30, pp. 380–382, 1979.

[12] D. Pines and D. Bohm, "A collective description of electron interactions: Ii. collective vs individual particle aspects of the interactions," *Phys. Rev.*, vol. 85, p. 338, 1952.

[13] R. Ruppin, "Non-local optics of the near field lens," *J. Phys.: Condens. Matter.*, vol. 17, p. 1803, 2005.

[14] T. Christensen, W. Yan, S. Raza, A. P. Jauho, N. A. Mortensen, and M. Wubs, "Nonlocal response of metallic nanospheres probed by light, electrons, and atoms," *ACS Nano*, vol. 8, no. 2, pp. 1745–1758, 2014.

[15] S. Raza, S. I. Bozhevolnyi, M. Wubs, and N. A. Mortensen, "Nonlocal optical response in metallic nanostructures," *J. Phys.: Condens. Matter*, vol. 27, p. 183204, 2015.

[16] M. Wubs and N. A. Mortensen, "Nonlocal response in plasmonic nanostructures," *Quantum plasmonics*, vol. 185, pp. 279–302, 2016.

[17] J. R. Maack, N. A. Mortensen, and M. Wubs, "Size-dependent nonlocal effects in plasmonic semiconductor particles," *EPL (Europhysics Letters)*, vol. 119, p. 17003, 2017.

[18] S. Buddhiraju, Y. Shi, A. Song, C. Wojcik, M. Minkov, I. A. D. Williamson, A. Dutt, and S. Fan, "Absence of unidirectionally propagating surface plasmon-polaritons in nonreciprocal plasmonics," 2018.

[19] S. A. H. Gangaraj and F. Monticone, "Do truly unidirectional surface plasmon-polaritons exist?," *Optica*, vol. 6, no. 9, pp. 1158–1165, 2019.

[20] C. F. Bohren and D. R. Huffman, *Absorption and Scattering of Light by Small Particles*. New York: John Wiley and Sons, 2008.

[21] J. D. Jackson, *Classical Electrodynamics*. New York: Wiley, 1998.

[22] M. G. Silveirinha and C. A. Fernandes, "Homogenization of 3d- connected and non-connected wire metamaterials," *IEEE Trans. on Microwave Theory and Tech.*, vol. 53, p. 1418, 2005.

[23] G. W. Hanson, E. Forati, and M. G. Silveirinha, "Modeling of spatially-dispersive wire media: transport representation, comparison with natural materials, and additional boundary conditions," *IEEE Trans. on Antennas and Propagat.*, vol. 60, p. 4219, 2012.

[24] C. David, N. A. Mortensen, and J. Christensen, "Perfect imaging, epsilon-near zero phenomena and waveguiding in the scope of nonlocal effects," *Sci. Rep.*, vol. 3, p. 2526, 2013.

[25] E. N. Bulgakov and A. F. Sadreev, "Resonance induced by a bound state in the continuum in a two-level nonlinear fano-anderson model," *Phys. Rev. B*, vol. 80, p. 115308, 2009.

[26] E. N. Bulgakov and A. F. Sadreev, "Bound states in a photonic fabry-perot resonator with nonlinear off-channel defects," *Phys. Rev. B*, vol. 81, p. 115128, 2010.

[27] E. N. Bulgakov and A. F. Sadreev, "Robust bound state in the continuum in a nonlinear microcavity embedded in a photonic crystal waveguide," *Optic. Lett.*, vol. 39, no. 17, pp. 5212–5215, 2014.

[28] E. N. Bulgakov, K. N. Pichugin, and A. F. Sadreev, "All-optical light storage in bound states in the continuum and release by demand," *Opt. Express*, vol. 23, no. 17, 2015.

[29] I. D. Leon and P. Berini, "Amplification of long-range surface plasmons by a dipolar gain medium," *Nat. Photon.*, vol. 4, p. 382, 2010.

[30] M. T. Hill and M. C. Gather, "Advances in small lasers," *Nat. Photon.*, vol. 8, p. 908, 2014.

Confined guided modes in a double wire medium slab

4.1 Introduction

As stated in the introduction, wire metamaterials have been extensively studied in recent years [1]. These artificial media are formed by long metallic rods arranged in various possible ways, ranging from simple periodic arrays of parallel wires [2–5] to more complex configurations with connected or non-connected orthogonal sets of wires [1,4,6–8]. The unique geometry of the wire metamaterials (with long and thin inclusions), combined with the high optical contrast between the metallic wires and the dielectric background, gives rise to peculiar electromagnetic properties such as a strongly spatially dispersive (nonlocal) response [1,5,6,9–11], extreme optical anisotropy [12], anomalously high density of photonic states [13–17], and low-loss broadband anomalous dispersion [18,19]. These unusual properties lead to quite interesting applications, including near-field transport and manipulation [20–26], ultra-compact waveguiding [27–29], negative refraction [30–33], near-field [34–36] and far-field [37, 38] superlensing and the correction of chromatic aberrations [39]. Furthermore, wire metamaterials may boost the Cherenkov emission by charged particles [14], enhance the Purcell factor [15], the Casimir interactions [13, 16, 40], and the radiative near-field heat transfer [41].

Effective medium models enable the accurate and fast characterization of the electromagnetic response of wire metamaterials [5,6,9–11,42]. In partic-

ular, homogenization methods have been used to analyze the guided modes supported by single wire medium slabs [43–48], and double wire medium slabs [27–29]. In the configurations studied in [27–29] the metallic wires are tilted by $\pm$ 45° with respect to the interfaces. In contrast, here we characterize the transverse magnetic (TM) guided modes supported by a double wire grid with one set of wires perpendicular to the interface with air, and another set parallel to the interface [see Fig. 4.1]. Our analytical model is based on the transverse average (TA)-field approach introduced in [49, 50], which enables taking into account explicitly the termination of the bulk structure. We demonstrate that in the continuum limit, the metamaterial slab supports a diverging (infinite) number of guided mode branches with dispersions that accumulate near the light line, with a comb-like structure. Interestingly, the guided modes that are weakly bounded to the wire metamaterial slab, may exhibit a fast field variation along the transverse direction. We suggest that these waves may be useful to detect structural defects with subwavelength dimensions.

The chapter is organized as follows. In Sect. 4.2 we briefly review the TA-field homogenization approach. In Sect. 4.3, we discuss the properties of the fundamental TM bulk mode supported by the double wire medium slab. In Sect. 4.4, we calculate the dispersion characteristic of the TM guided modes and compare the analytical results with full-wave simulations. Then, in Sect. 4.5 we show that the guided modes can be used to detect subwavelength defects or imperfections. Finally, in Sec. 4.6 the conclusions are drawn. In this work we assume that the fields are monochromatic with a time variation $e^{j\omega t}$.

4.2   Homogenization model

The wire metamaterial consists of a grid of nonconnected metallic wires with radius r_{w}. The two mutually orthogonal sets of wires are oriented along the x and z directions, as illustrated in Fig. 4.1. The spacing between adjacent parallel wires is a, whereas the spacing between adjacent orthogonal wires is $a/2$. The wires are embedded in a standard dielectric with relative permittivity ε_h.

In the long-wavelength regime ($\lambda >> a$) the wire grid may be regarded as a continuum described by the relative dielectric function [6, 8, 51]
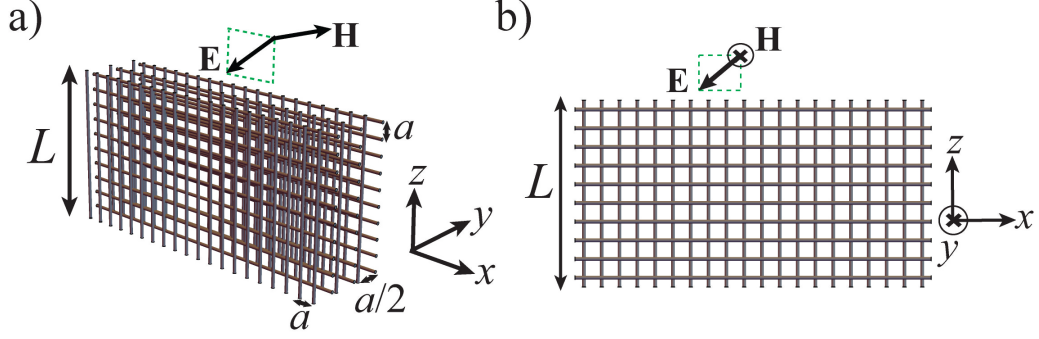
Figure 4.1: Geometry of the crossed wire grid formed by two mutually orthogonal and nonconnected sets of metallic wires oriented along the x and z directions. The spacing between adjacent parallel wires is a, whereas the spacing between adjacent orthogonal wires is $a/2$. The thickness of the slab along the z direction is L. (a) Perspective view and (b) top view.

$$\bar{\bar{\varepsilon}} = \varepsilon_{xx}\hat{\mathbf{x}} \otimes \hat{\mathbf{x}} + \varepsilon_h\hat{\mathbf{y}} \otimes \hat{\mathbf{y}} + \varepsilon_{zz}\hat{\mathbf{z}} \otimes \hat{\mathbf{z}} \quad , \tag{4.1}$$

where $\hat{\mathbf{x}}$, $\hat{\mathbf{y}}$ and $\hat{\mathbf{z}}$ are the unit vectors along the coordinate axes. For ideal perfectly electrical conducting (PEC) thin wires ($r_{\mathrm{w}}/a << 1$), the relative permittivity components ε_{xx} and ε_{zz} are given by [6, 8, 51]

$$\varepsilon_{ii} = \varepsilon_h\left(1 - \frac{\beta_{\mathrm{p}}^2}{\beta^2 - k_i^2}\right), \quad i = x, z \quad , \tag{4.2}$$

where β_{p} is the effective plasma wavenumber, $\beta = \sqrt{\varepsilon_h}(\omega/c)$ is the wave number in the dielectric host, and c is the speed of light in vacuum. The parameter β_{p} depends uniquely on the geometrical properties of the structure [5] and satisfies

$$\beta_{\mathrm{p}} = \frac{1}{a}\sqrt{\frac{2\pi}{ln\left(\frac{a}{2\pi r_{\mathrm{w}}}\right) + 0.5275}} \quad . \tag{4.3}$$

In the usual approach, the bulk medium fields obtained from the effective dielectric function are used to characterize the wave propagation. However, for thin metamaterial slabs, the bulk medium fields may fail to accurately model the electromagnetic response near the interfaces, as shown in [50].

This happens in part because the electromagnetic response is sensitive to the termination plane, i.e., to the plane where the bulk material is truncated. To circumvent this problem, we rely on the transverse average (TA)-field approach introduced in [49,50]. In the TA-field approach the microscopic fields are averaged only along the directions parallel to the interface (in the present problem, along the x- and y- directions). In contrast, the bulk medium fields are obtained by averaging the microscopic fields over the 3D unit cell.

Interestingly, it was demonstrated in [50] that in some conditions the TA-fields can be written in terms of the bulk medium fields. In particular, for the considered wire grid the TA-fields associated with a plane wave of the bulk medium with electric field $\mathbf{E} = \mathbf{E}_{\mathrm{av}} e^{-j\mathbf{k}\cdot\mathbf{r}}$ and wave vector $\mathbf{k} = (k_x, k_y, k_z)$ are given by (for convenience, we use notations slightly different from the ones of [50])

$$\mathbf{E}_{\mathrm{TA}}(z; k_z) = \beta^2 \bar{\mathcal{G}}(z|z_x; \mathbf{k}) e^{-jk_z z_x} \cdot \hat{\mathbf{x}}\hat{\mathbf{x}} \cdot (\varepsilon_{xx} - 1)\mathbf{E}_{\mathrm{av}} e^{-j\mathbf{k}_{||}\cdot\mathbf{r}}$$
$$+ \frac{1}{k^2 - \beta^2}(\beta^2 \mathbf{1} - \mathbf{k} \otimes \mathbf{k}) e^{-jk_z z} \cdot \hat{\mathbf{z}}\hat{\mathbf{z}} \cdot (\varepsilon_{zz} - 1)\mathbf{E}_{\mathrm{av}} e^{-j\mathbf{k}_{||}\cdot\mathbf{r}}, \quad (4.4\mathrm{a})$$

$$\mathbf{B}_{\mathrm{TA}} = \frac{1}{-j\omega}\left(-j\mathbf{k}_{||} + \frac{\partial}{\partial z}\hat{\mathbf{z}} \right) \times \mathbf{E}_{\mathrm{TA}} \quad , \quad (4.4\mathrm{b})$$

where $\mathbf{k}_{||} = (k_x, k_y, 0)$ is the transverse wave vector, $\mathbf{1}$ is the identity dyadic, and $z = z_x$ represents the z-coordinate of a generic plane of wires directed along the x-direction. The TA electric and induction fields are denoted by $\mathbf{E}_{\mathrm{TA}}$ and $\mathbf{B}_{\mathrm{TA}}$. The tensor $\bar{\mathcal{G}}$ is defined by [50]

$$\bar{\mathcal{G}}(z|z_x; \mathbf{k}) = \left[\mathbf{1} + \frac{1}{\beta^2}\left(-j\mathbf{k}_{||} + \frac{\partial}{\partial z}\hat{\mathbf{z}} \right) \otimes \left(-j\mathbf{k}_{||} + \frac{\partial}{\partial z}\hat{\mathbf{z}} \right) \right] A(z - z_x; k_z) \quad (4.5\mathrm{a})$$

$$A(z; k_z) = \frac{a}{2\gamma_0}\left[e^{-\gamma_0|z|} + \sum_{\pm} \frac{e^{\pm\gamma_0 z}}{e^{(\gamma\pm jk_z)a} - 1} \right], \quad |z| < a/2. \quad (4.5\mathrm{b})$$

Here, $\gamma = \sqrt{k_{||}^2 - \beta^2}$ and the sum in (4.5b) is over two terms one with the "+" sign and other with the "-" sign. The function $A(z; k_z)$ can be extended to arbitrary z as a Bloch wave with propagation constant k_z. For more details, a reader is referred to [50].

4.3   Isofrequency contours of the bulk medium

We want to study the wave propagation in the *xoz* plane ($k_y = 0$) with magnetic field polarized along the *y*-direction [see Fig. 4.1]. The dispersion characteristic of the TM modes supported by the crossed wire grid is determined by [32]

$$\frac{k_x^2}{k^2 - \beta^2 \varepsilon_{xx}} + \frac{k_z^2}{k^2 - \beta^2 \varepsilon_{zz}} = 1, \tag{4.6}$$

which may be reduced to a polynomial equation of second degree in the variable k_z^2. This means that the crossed wire grid supports *two* independent TM plane wave modes with $\mathbf{H} = H_y \hat{\mathbf{y}}$ and propagation constants along z of the form $\pm k_z^{(1)}$ and $\pm k_z^{(2)}$. Thus, as compared to a standard dielectric there is an additional TM wave. This property is a fingerprint of the strongly nonlocal response of the wire metamaterial [6, 8, 51]. It turns out that for long wavelengths, one of the TM waves is an evanescent wave ($\pm k_z^{(2)}$ is purely imaginary), and thereby there is a single propagating mode in the wire grid (with real-valued propagation constant $\pm k_z^{(1)}$). The (bulk) fields associated with a generic TM plane wave are of the form:

$$\mathbf{H} = H_0 e^{-j\mathbf{k}\cdot\mathbf{r}}\hat{\mathbf{y}}, \quad \mathbf{E} = \frac{H_0}{\omega\varepsilon_0}\left(\frac{k_z}{\varepsilon_{xx}}\hat{\mathbf{x}} - \frac{k_x}{\varepsilon_{zz}}\hat{\mathbf{z}}\right)e^{-j\mathbf{k}\cdot\mathbf{r}}. \tag{4.7}$$

The isofrequency contours of the propagating TM mode supported by the unbounded wire grid are depicted in Fig. 4.2(a). The isofrequency contours consist of two hyperbolas with asymptotes running along the x and z directions, i.e., the directions parallel to the two sets of wires. Curiously, the asymptotes correspond to the flat isofrequency contours of the TEM modes supported by each individual array of parallel wires [45, 52]. The shape of the isofrequency contours implies that the group velocity tends to be oriented along the wire directions.

Moreover, because of the hyperbolic nature of the isofrequency contours the wire grid can support waves with rather large wave vectors. Interestingly, as $|k_x|$ approaches the host medium wave number ($|k_x| \to \beta + 0^+$) the corresponding $k_z \equiv k_z^{(1)}$ diverges to infinity [see Fig. 4.2(b)]. This suggests that a finite thickness wire medium slab (truncated at $z = 0$ and $z = L$) may support weakly bounded guided modes with $|k_x|$ slightly larger than β. Specifically, if the host medium is air, the guided modes are expected to
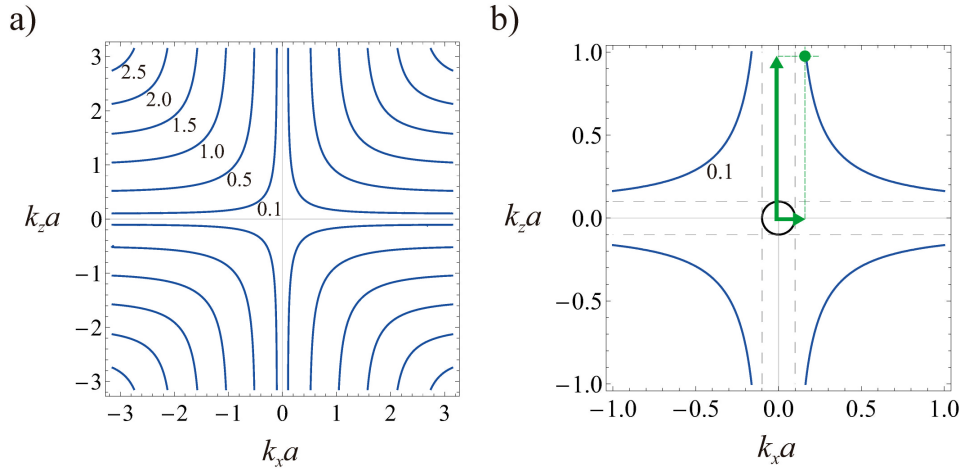
a)

b)

Figure 4.2: (a) Isofrequency contours of the fundamental TM bulk mode for a metamaterial formed by wires standing in air. The wire radius is $r_{\mathrm{w}} = 0.05a$. The text insets indicate the value of the normalized frequency $\omega a/c$. The gray dashed lines represent the asymptotes of the hyperbolas. The green arrows represent the k_x and k_z components of the wave vector of a particular bulk mode with k_x slightly larger than ω/c.

have dispersions near the light line and to be associated with fields that vary extremely fast along the z direction. Note that heuristically the condition for the emergence of guided modes is that $k_z^{(1)} L \approx n\pi$ with $n = 1, 2, 3, \ldots$ an integer and $k_z^{(1)} = k_z^{(1)}(k_x, \omega)$ the positive real-valued solution of (4.6) with respect to k_z. Since $k_z^{(1)}$ has a divergent behavior as $|k_x| \to \omega/c$, it is obvious that $k_z^{(1)} L \approx n\pi$ can have an infinite number of solutions (each associated with a different n) with k_x slightly larger than ω/c. In other words, the continuum model predicts a diverging number of guided modes with dispersions piling up near the light line. In the next section, this prediction is numerically verified.

4.4 Dispersion characteristic of the guided modes

The dispersion of the TM guided modes supported by the wire grid slab can be calculated in the usual way by expanding the electromagnetic fields in

the air and wire grid regions in terms of plane waves. However, different from the standard homogenization approach, here the fields inside the wire metamaterial are written in terms of the TA-fields, rather than in terms of the bulk fields. Specifically, for $0 < z < L$ one has:

$$
\begin{aligned}
\mathbf{E}(z) = & B_1^+ \mathbf{E}_{\text{TA}}(z; k_z^{(1)}) + B_1^- \mathbf{E}_{\text{TA}}(z; -k_z^{(1)}) \\
& + B_2^+ \mathbf{E}_{\text{TA}}(z; k_z^{(2)}) + B_2^- \mathbf{E}_{\text{TA}}(z; -k_z^{(2)})
\end{aligned}
\tag{4.8a}
$$

$$
\begin{aligned}
\mathbf{H}(z) = & B_1^+ \mathbf{H}_{\text{TA}}(z; k_z^{(1)}) + B_1^- \mathbf{H}_{\text{TA}}(z; -k_z^{(1)}) \\
& + B_2^+ \mathbf{H}_{\text{TA}}(z; k_z^{(2)}) + B_2^- \mathbf{H}_{\text{TA}}(z; -k_z^{(2)})
\end{aligned}
\tag{4.8b}
$$

where $B_{1,2}^{\pm}$ are the complex amplitudes of the excited waves in the meta-material and $\mathbf{E}_{\text{TA}}(z; k)$ is found from the relevant bulk electric field in (4.7) using (4.4a) with $\mathbf{k}_{||} = k_x \hat{\mathbf{x}}$. Here, k_x is the wavenumber of the guided mode. Furthermore, $\mathbf{H}_{\text{TA}} = \mathbf{B}_{\text{TA}}/\mu_0$ is obtained from the corresponding $\mathbf{E}_{\text{TA}}$ using equation (4.4b). Similarly, in the air regions it is possible to write:

$$
\mathbf{E} = \frac{1}{j\omega\varepsilon_0} e^{-jk_x x}
\begin{cases}
(\gamma_0 \hat{\mathbf{x}} - jk_x \hat{\mathbf{z}}) A_1 e^{-\gamma_0(z-L)} & , z > L \\
(-\gamma_0 \hat{\mathbf{x}} - jk_x \hat{\mathbf{z}}) A_2 e^{+\gamma_0 z} & , z < 0
\end{cases}
\tag{4.9a}
$$

$$
\mathbf{H} = \hat{\mathbf{y}} e^{-jk_x x}
\begin{cases}
A_1 e^{-\gamma_0(z-L)} & , z > L \\
A_2 e^{+\gamma_0 z} & , z < 0
\end{cases}
\tag{4.9b}
$$

where $\gamma_0 = \sqrt{k_x^2 - \omega^2 \varepsilon_0 \mu_0}$ is the free-space propagation constant and $A_{1,2}$ are the complex amplitudes of the excited waves in the air regions.

At the interfaces with air ($z = 0$ and $z = L$), we enforce the continuity of the tangential components of the electromagnetic fields (H_y and E_x) and an additional boundary condition (ABC) [53, 54] that guarantees that the electric current flowing along the wires directed along z vanishes. When the host medium is the same in all the three regions of space, the ABC is equivalent to enforce that the normal component of the electric field (E_z) is continuous at the interfaces [54]. In this manner, we obtain a homogeneous 6×6 linear system. The dispersion of the TM guided modes is found by setting the determinant of the linear system equal to zero.

The calculated dispersion characteristic (ω vs. k_x) of the TM guided modes for a wire grid with a fixed thickness L and two different wire densities a/L is depicted in Fig. 4.3. As seen, the metamaterial slab has an intriguing dispersion diagram formed by a "comb" of guided mode branches that

accumulate near the light line for low frequencies. The green dashed curves in Fig. 4.3 were obtained with the effective medium model, whereas the blue solid curves were calculated with the eigenmode solver of CST Microwave Studio [55] that takes into account the granularity of the metamaterial slab. The effective medium results concur well with the full-wave results, even for high frequencies and large wave vectors when the lattice constant becomes comparable to the wavelength and the homogenization is expected to become less accurate (the limit of the Brillouin zone).
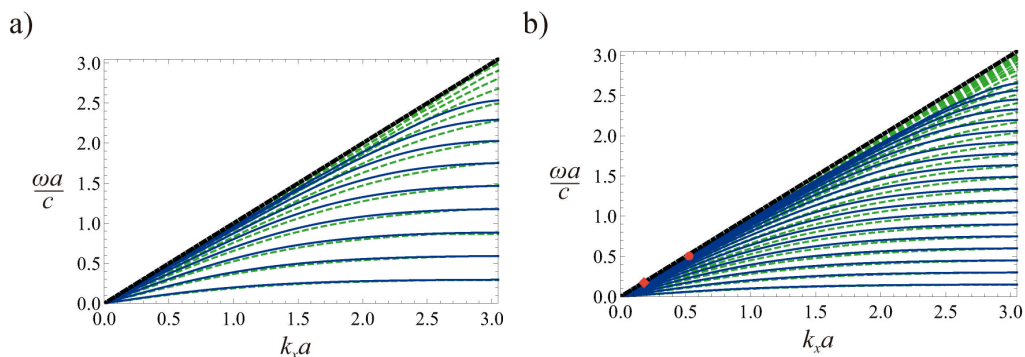

Figure 4.3: Comb-like dispersion diagram of the TM guided modes supported by a metamaterial slab, for a fixed slab thickness L and different lattice periods a. The radius of the wires is $r_{\mathrm{w}} = 0.05a$. (a) $a = L/10$ and (b) $a = L/20$. The green dashed curves and the blue solid curves are obtained from the effective medium model and CST Microwave Studio simulations [55], respectively. The black dashed line represents the light line.

The peculiar comb-like structure of the dispersion diagram is a consequence of the strongly hyperbolic response of the metamaterial near the static limit, as already discussed in Sect. 4.3. Remarkably, within the effective medium framework – wherein the wire grid is regarded as an ideal electromagnetic continuum – the number of guided modes diverges to infinity [see green dashed curves in Fig. 4.3(a)-(b)]. In contrast, when the granularity of the metamaterial slab is taken into account the number of guided modes becomes finite and depends on the wire density. Specifically, it turns out that the number of guided modes is exactly $N - 1$, where $N = L/a$ represents the number of unit cells along the z-direction. This feature is consistent with the fact that the structure is effectively a stack of N metallic sheets; i.e., the

structure may be roughly regarded as a transmission line formed by N independent conductors, which supports $N-1$ independent transmission-line modes (quasi-TEM modes). Note that all the wires in the same z =const. plane behave effectively as a single conductor.
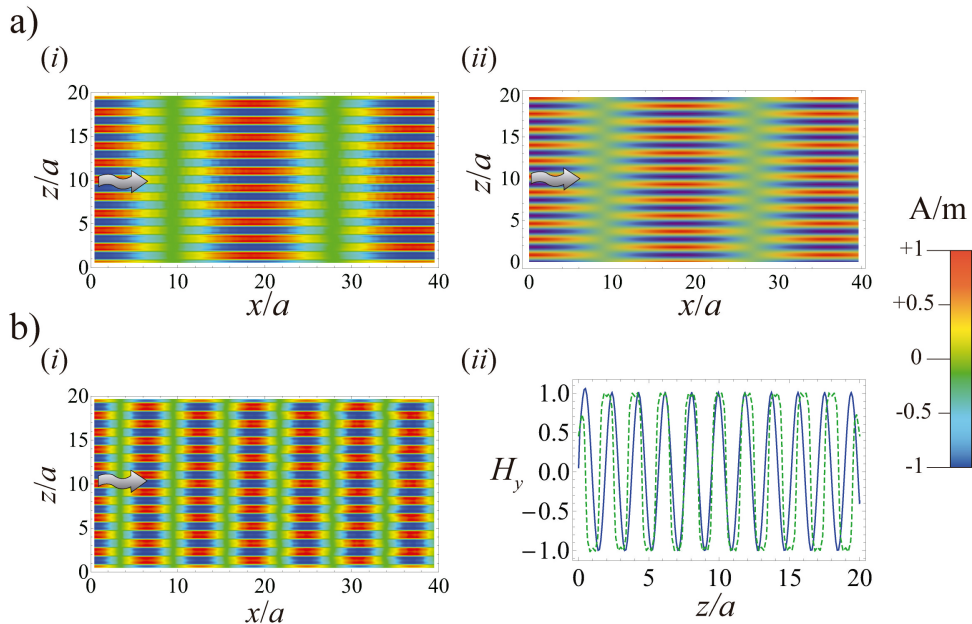

Figure 4.4: (a) Magnetic field (H_y) distribution in the xoz-plane for the guided mode associated with the diamond-shaped red symbol in Fig. 4.3(b); the mode has $\omega a/c = 0.17$ and $k_x c/\omega = 1.007$. (i) Result obtained with CST Microwave Studio [55]; (ii) Result obtained with the effective medium model. (b) (i) Similar to (ai) but for the mode associated with the circular-shaped red symbol in Fig. 4.3(b) obtained with CST Microwave Studio [55]; the mode has $\omega a/c = 0.506$ and $k_x c/\omega = 1.005$; (ii) Transverse field profile for the same mode as in (i). The blue solid curves are calculated with the effective medium model and the green dashed curves with the full-wave simulator [55].

In Fig. 4.4, we depict the transverse electromagnetic field distributions of the modes marked in Fig. 4.3(b) with the discrete red symbols. The results are calculated using both the effective medium model (solving the homogeneous system discussed in Sect. 4.4) and the full-wave simulations (excitation of the guided mode by applying a phased array of voltage gener-

ators to the wires directed along x, analogous to Fig. 4.5(b)) [55]. As seen in Figs. 4.4(a)(i-ii) and (b)(ii), there is a reasonably good agreement between the two calculation methods, further demonstrating the validity of the TA-field approach. In Fig. 4.4(b)(ii), the agreement between the full wave simulation and the effective model deteriorates slightly near the interfaces ($z = 0$ and $z = 20a$) because of the excitation of higher order evanescent waves not captured by the effective medium formalism.

The results of Fig. 4.4 confirm that the weakly bounded guided modes (with $k_x c/\omega \approx 1$) may exhibit a very fast variation along the z-direction. This is evident in the time snapshot of the transverse magnetic field shown in Figs. 4.4(a)(i-ii). Clearly, the longitudinal component of the wave vector is much smaller than the transverse component (i.e. $k_x/k_z << 1$), which is in agreement with the hyperbolic isofrequency contours of the bulk medium (Fig. 4.2). For increasing frequencies, the discrepancy between the transverse and longitudinal wave numbers is progressively smaller [see Fig. 4.4(b)(i)].

4.5 Detection of structural imperfections

The rather short transverse wavelength of the guided modes may be advantageously exploited to detect structural defects or imperfections with subwavelength dimensions in the host medium. For example, they may be used to detect structural changes due to the exposure of the material to adverse conditions (e.g., high pressure, mechanical deformations, etc), which may lead to cracks or other defects.

To illustrate the idea, we consider a scenario wherein a pair of subwavelength square-shaped obstacles (with dimensions $p_x = p_z = 2a$) made of an highly absorbing material are placed inside a square wire grid with dimensions $L_x = L_z = 30a$ and lattice constant $a = 1$mm [Fig. 4.5(a)]. A fast-varying guided mode is generated by exciting adjacent planes of metallic wires with voltages in opposition of phase, as illustrated in Fig. 4.5(b). The two orthogonal sets of wires are excited separately: first the wires parallel to the z-direction (Fig. 4.5(b)(i)) and then the wires oriented along the x-direction (Fig. 4.5(b)(ii)).
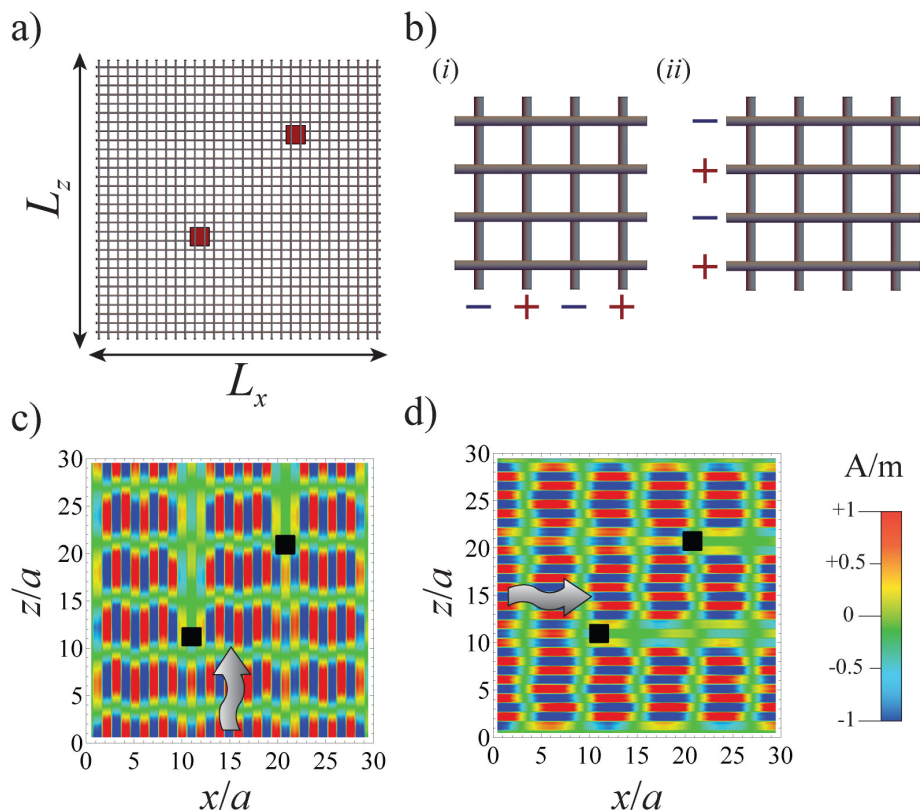
Figure 4.5: (a) Geometry of a square wire grid with lattice period $a = L/30$ and wire radius $r_\text{w} = 0.05a$, with two square-shaped obstacles with dimensions $2a$ placed inside the grid. The obstacles are made of a highly absorbing material ($\varepsilon_\text{obs}/\varepsilon_0 = 1 - j5$, $\mu_{obs}/\mu_0 = 1 - j5$). (b) Illustration of the wire grid excitation. (c) and (d) Time snapshots of the normalized magnetic field $H_y(t = 0)$ obtained with CST Microwave Studio [55], for a wire grid with $a = 1$ mm and $f = 23.9$ GHz. (c) Excitation of the z-oriented wires; (d) excitation of the x-oriented wires. The direction of the wave propagation is indicated by the gray arrows.

In Figs. 4.5(c)-(d), we show time snapshots of the radiated magnetic field, $H_y(t = 0)$, in the presence of the two subwavelength absorbing obstacles, for each of the two excitations discussed previously and for the oscillation frequency $f = 23.9$ GHz. The results were obtained using CST Microwave Studio [55]. Notwithstanding the subwavelength dimensions of the absorbing obstacles, two prominent shadows are perfectly discernible behind the obstacles position. In this example, the shadow regions are due to the energy absorbed by the particles. The emergence of the subwavelength shadows is only possible due to the fast transverse variation of the guided modes supported by the wire grid. A similar effect would occur in presence of a crack that disrupts some subset of metallic wires. Thus, the proposed structure may be useful to detect and localize defects due to structural changes of the host material.

4.6 Conclusions

In conclusion, it was demonstrated that with the continuum approximation a nonconnected crossed wire grid supports a diverging number of guided mode branches that pile up near the light line for low frequencies. In practice, due to the granularity of the metamaterial, the number of guided modes is finite and depends on the wire density. The comb-like structure of the dispersion diagram is rooted in the strong hyperbolic response of the double wire array near the static limit. It was shown that even though the guided modes are weakly attached to the wire grid slab, they exhibit an extremely fast field variation along the transverse direction. Finally, it was suggested that the studied metamaterial may be useful to pinpoint subwavelength defects or imperfections due to structural changes of the host material.

Bibliography

[1] C. R. Simovski, P. A. Belov, A. V. Atrashchenko, and Y. S. Kivshar, "Wire Metamaterials: Physics and Applications," *Advanced Materials*, vol. 24, no. 31, pp. 4229–4248, 2012.

[2] W. Rotman, "Plasma simulation by artificial dielectrics and parallel-plate media," *IRE Transactions on Antennas and Propagation*, vol. 10, no. 1, pp. 82–95, 1962.

[3] J. Brown, "Artificial dielectrics," *Prog. Dielect.*, vol. 2, pp. 195–225, 1960.

[4] J. B. Pendry, A. J. Holden, W. J. Steart, and I. Youngs, "Extremely Low Frequency Plasmons in Metallic Mesostructures," *Physical Review Letters*, vol. 76, p. 4773, 1996.

[5] P. A. Belov, R. Marqués, S. I. Maslovski, I. S. Nefedov, M. Silveirinha, C. R. Simovski, and S. A. Tretyakov, "Strong spatial dispersion in wire media in the very large wavelength limit," *Physical Review B*, vol. 67, p. 113103, 2003.

[6] C. R. Simovski and P. A. Belov, "Low-frequency spatial dispersion in wire media," *Physical Review E*, vol. 70, p. 046616, 2004.

[7] I. S. Nefedov, A. J. Viitanen, and S. A. Tretyakov, "Propagating and evanescent modes in two-dimensional wire media," *Physical Review E*, vol. 71, p. 046612, 2005.

[8] M. G. Silveirinha and C. A. Fernandes, "Homogenization of 3-D-Connected and Nonconnected Wire Metamaterials," *IEEE Transactions on Microwave Theory and Techniques*, vol. 53, no. 4, 2005.

[9] M. G. Silveirinha, "Nonlocal homogenization model for a periodic array of ϵ-negative rods," *Physical Review E*, vol. 73, p. 046612, 2006.

[10] M. G. Silveirinha, "Additional Boundary Condition for the Wire Medium," *IEEE Transactions on Antennas and Propagation*, vol. 54, no. 6, 2006.

[11] S. I. Malovski and M. G. Silveirinha, "Nonlocal permittivity from a quasistatic model for a class of wire media," *Physical Review B*, vol. 80, p. 245101, 2009.

[12] M. G. Silveirinha, C. A. Fernandes, and J. R. Costa, "Electromagnetic characterization of textured surfaces formed by metallic pins," *IEEE Transactions on Antennas and Propagation*, vol. 56, no. 2, pp. 405–415, 2008.

[13] S. I. Maslovski and M. G. Silveirinha, "Mimicking Boyer's Casimir repulsion with a nanowire material," *Physical Review A*, vol. 83, p. 022508, 2011.

[14] D. E. Fernandes, S. I. Maslovski, and M. G. Silveirinha, "Cherenkov emission in a nanowire material," *Physical Review B*, vol. 85, p. 155107, 2012.

[15] A. N. Poddubny, P. A. Belov, and Y. S. Kivshar, "Purcell effect in wire metamaterials," *Physical Review B*, vol. 87, p. 035136, 2013.

[16] T. A. Morgado, S. I. Maslovski, and M. G. Silveirinha, "Ultrahigh Casimir interaction torque in nanowire systems," *Optics Express*, vol. 21, no. 12, pp. 14943–14955, 2013.

[17] A. Poddubny, I. Iorsh, P. Belov, and Y. Kivshar, "Hyperbolic metamaterials," *Nature Photonics*, vol. 7, pp. 948–957, 2013.

[18] M. G. Silveirinha, "Anomalous Refraction of Light Colors by a Metamaterial Prism," *Physical Review Letters*, vol. 102, p. 193903, 2009.

[19] T. A. Morgado, J. S. Marcos, J. R. C. J. T. Costa, C. A. Fernandes, and M. G. Silveirinha, "Reversed rainbow with a nonlocal metamaterial," *Physical Review Letters*, vol. 105, p. 264101, 2014.

[20] P. A. Belov, Y. Hao, and S. Sudhakaran, "Subwavelength microwave imaging using an array of parallel conducting wires as a lens," *Physical Review B*, vol. 73, p. 033108, 2006.

[21] M. G. Silveirinha, P. A. Belov, and C. R. Simovski, "Subwavelength imaging at infrared frequencies using an array of metallic nanorods," *Physical Review B*, vol. 75, p. 035108, 2007.

[22] P. A. Belov, Y. Zhao, S. Tse, P. Ikonen, M. G. Silveirinha, C. R. Simovski, S. Tretyakov, Y. Hao, and C. Parini, "Transmission of images with subwavelength resolution to distances of several wavelengths in the microwave range," *Physical Review B*, vol. 77, p. 193108, 2008.

[23] P. Ikonen, C. Simovski, and S. Tretyakov, "Magnification of subwavelength field distributions at microwave frequencies using a wire medium slab operating in the canalization regime," *Applied Physics Letters*, vol. 91, p. 104102, 2007.

[24] G. Shvets, S. Trendafilov, J. B. Pendry, and A. Sarychev, "Guiding, Focusing and Sensing on the Subwavelength Scale Using Metallic Wire Arrays," *Physical Review Letters*, vol. 99, p. 053903, 2007.

[25] T. A. Morgado and M. G. Silveirinha, "Transport of an arbitrary near-field component with an array of tilted wires," *New Journal of Physics*, vol. 11, no. 8, p. 083023, 2009.

[26] T. A. Morgado, J. S. Marcos, M. G. Silveirinha, and S. I. Maslovski, "Experimental verification of full reconstruction of the near-field with a metamaterial lens," *Applied Physics Letters*, vol. 97, p. 144102, 2010.

[27] M. G. Silveirinha and C. A. Fernandes, "Nonresonant structured material with extreme effective parameters," *Physical Review B*, vol. 78, p. 033108, 2008.

[28] M. G. Silveirinha, C. A. Fernandes, J. R. Costa, and C. R. Medeiros, "Experimental demonstration of a structured material with extreme effective parameters at microwaves," *Applied Physics Letters*, vol. 93, p. 174103, 2008.

[29] T. A. Morgado, J. S. Marcos, M. G. Silveirinha, and S. I. Maslovski, "Ultraconfined Interlaced Plasmons," *Physical Review Letters*, vol. 107, no. 6, p. 06390, 2011.

[30] Y. Liu, G. Bartal, and X. Zhang, "All-angle negative refraction and imaging in a bulk medium made of metallic nanowires in the visible region," *Optics Express*, vol. 16, p. 15439, 2008.

[31] J. Yao, Z. Liu, Y. Liu, Y. Wang, C. Sun, G. Bartal, A. M. Stacy, and X. Zhang, "Optical Negative Refraction in Bulk Metamaterials of Nanowires," *Science*, vol. 321, no. 5891, p. 930, 2008.

[32] M. G. Silveirinha, "Broadband negative refraction with a crossed wire mesh," *Physical Review B*, vol. 79, p. 153109, 2009.

[33] T. A. Morgado, J. S. Marcos, S. I. Maslovski, and M. G. Silveirinha, "Negative Refraction and Partial Focusing with a Crossed Wire Mesh: Physical Insights and Experimental Verification," *Applied Physics Letters*, vol. 101, p. 021104, 2012.

[34] M. G. Silveirinha, C. A. Fernandes, and J. R. Costa, "Superlens made of a metamaterial with extreme effective parameters," *Physical Review B*, vol. 78, p. 195121, 2008.

[35] M. G. Silveirinha, C. R. Medeiros, C. A. Fernandes, and J. R. Costa, "Experimental verification of broadband superlensing using a metamaterial with an extreme index of refraction," *Physical Review B*, vol. 81, p. 033101, 2010.

[36] M. G. Silveirinha, "Artificial plasma formed by connected metallic wires at infrared frequencies," *Physical Review B*, vol. 79, p. 035118, 2009.

[37] F. Lemoult, G. Lerosey, J. Rosny, and M. Fink, "Resonant metalenses for breaking the diffraction barrier," *Physical Review Letters*, vol. 104, p. 203901, 2010.

[38] F. Lemoult, M. Fink, and G. Lerosey, "A polychromatic approach to far-field superlensing at visible wavelengths," *Nature Communications*, vol. 3, p. 889, 2012.

[39] J. T. Costa and M. G. Silveirinha, "Achromatic lens based on a nanowire material with anomalous dispersion," *Optics Express*, vol. 20, no. 13, pp. 13915–13922, 2012.

[40] S. I. Maslovski and M. G. Silveirinha, "Ultralong-range Casimir-Lifshitz forces mediated by nanowire materials," *Physical Review A*, vol. 82, p. 022511, 2010.

[41] I. S. Nefedov and C. R. Simovski, "Giant radiation heat transfer through micron gaps," *Physical Review B*, vol. 84, p. 195459, 2011.

[42] S. I. Maslovski, S. A. Tretyakov, and P. A. Belov, "Wire media with negative effective permittivity: A quasi-static model," *Microwave and Optical Technology Letters*, vol. 35, pp. 47–51, 2002.

[43] P. A. Belov and M. G. Silveirinha, "Resolution of subwavelength transmission devices formed by a wire medium," *Physical Review E*, vol. 73, p. 056607, 2006.

[44] F. Lemoult, N. Kaina, M. Fink, and G. Lerosey, "Wave propagation control at the deep subwavelength scale in metamaterials," *Nature Physics*, vol. 9, pp. 55–60, 2012.

[45] F. Lemoult, M. Fink, and G. Lerosey, "Revisiting the wire medium: an ideal resonant metalens," *Waves Random Complex Media*, vol. 21, p. 591–613, 2011.

[46] Y. Tyshetskiy, S. V. Vladimirov, A. E. Ageyskiy, I. I. Iorsh, A. Orlov, and P. Belov, "Guided modes in a spatially dispersive wire medium slab," *Journal of the Optical Society of America B*, vol. 31, no. 8, pp. 1753–1760, 2014.

[47] J. S. Brownless, B. C. P. Sturmberg, A. Argyros, B. T. Kuhlmey, and C. M. de Sterke, "Guided modes of a wire medium slab: Comparison of effective medium approaches with exact solutions," *Physical Review B*, vol. 91, p. 155427, 2015.

[48] P. A. Belov, R. Dubrovka, I. Iorsh, I. Yagupov, and Y. S. Kivshar, "Single-mode subwavelength waveguides with wire metamaterials," *Applied Physics Letters*, vol. 103, p. 161103, 2013.

[49] M. G. Silveirinha and C. A. Fernandes, "Homogenization of Metamaterial Surfaces and Slabs: The Crossed Wire Mesh Canonical Problem," *IEEE Transactions on Antennas and Propagation*, vol. 53, pp. 59–69, 2005.

[50] M. G. Silveirinha and C. A. Fernandes, "Transverse-average field approach for the characterization of thin metamaterial slabs," *Physical Review E*, vol. 75, p. 036613, 2007.

[51] I. S. Nefedov, A. J. Viitanen, and S. A. Tretyakov, "Electromagnetic wave refraction at an interface of a double wire medium," *Physical Review B*, vol. 72, p. 245113, 2005.

[52] P. A. Belov, C. R. Simovski, , and P. Ikonen, "Canalization of subwavelength images by electromagnetic crystals," *Physical Review B*, vol. 71, p. 193105, 2005.

[53] M. G. Silveirinha, C. A. Fernandes, and J. R. Costa, "Additional boundary condition for a wire medium connected to a metallic surface," *New Journal of Physics*, vol. 10, p. 053011, 2008.

[54] M. G. Silveirinha, "Additional Boundary Conditions for Nonconnected Wire Media," *New Journal of Physics*, vol. 11, p. 113016, 2009.

[55] Dassault Systèmes, "2018 CST Microwave Studio."

CHAPTER 5

Trapped light modes in topological photonic systems

5.1 Introduction

As discussed in the general introduction, topology has recently emerged as a new tool to characterize global properties of physical systems, e.g., physical responses that are robust to perturbations of the system parameters [1–11]. There are different classes of topological platforms. Usually a nontrivial topology is rooted in some particular symmetry or combination of symmetries of the system, e.g., invariance under discrete translations, time-reversal, parity, etc. For systems with a Chern-type classification the topological analysis relies on the spectrum of some family of Hermitian operators $\hat{H}_{\mathbf{q}}$ parameterized by a two-component label $\mathbf{q} = (q_1, q_2)$ [12, 13]. The Hermitian property is not essential [13–21]. Provided the two-parameter space is a closed surface with no boundary and $\hat{H}_{\mathbf{q}}$ varies smoothly with $\mathbf{q}$, then it is possible to assign a topological number $\mathcal{C}$ to each band of eigenfunctions. This result is known as the Chern theorem. The number $\mathcal{C}$ is an integer and its value is insensitive to perturbations of $\hat{H}_{\mathbf{q}}$ that do not close the band-gap.

In most studies so far, the topological properties are inherited from the periodicity of the system along two-directions of space and $\mathbf{q}$ is identified with a Bloch wave vector. The corresponding two-parameter space is a Brillouin zone, which is effectively a closed surface with no boundary (a torus) due to its cyclic nature, as required by the Chern theorem. Thus, topological mate-

rials are characterized by integer Chern numbers. Here, we depart away from this paradigm and present an example of a photonic-type topological system with a synthetic dimension and fractional Chern numbers. Our analysis unveils that "fractional" topological numbers can emerge when $\hat{H}_{\mathbf{q}}$ is discontinuous in the $\mathbf{q}$-space. It is shown that a spatial displacement in real-space "pumps" topological charge into the system with the synthetic dimension. It should be noted that fractional Chern insulators have been widely discussed in condensed-matter systems [22–24]. However, the emergence of fractional Chern numbers in such platforms is rooted in many-body effects, and, in our understanding, there is no obvious link between our theory and these systems.

This chapter is organized as follows. In Section 5.2 it is shown that in 1D-type periodic systems the number of photonic bands below the gap can be understood as a topological number. In Section 5.3, we link the gap Chern number to the number of edge states supported by an extended system with a synthetic dimension. It is demonstrated that in real-space the topological number determines the number of gapless trapped-state branches that are created when the geometry of the 1D-periodic system is continuously displaced by one spatial period. In Section 5.4, we show that fractional gap Chern numbers may arise in 1D-periodic systems with inversion-symmetry due to a discontinuity of $\hat{H}_{\mathbf{q}}$ in the $\mathbf{q}$-space. The conclusions are drawn in Section 5.5.

5.2 Topological band count

We consider a generic platform that is formed by a 1D real-space periodic system, which we shall designate as "waveguide". The "waveguide" can be visualized as some periodic (possibly three-dimensional (3D)) structure that only allows propagation (waveguiding) along the x-direction. For example, it can be a hollow metallic structure, with the metal walls invariant to translations along the x-axis, and with the guide periodically loaded with dielectric inclusions $\varepsilon(x, y, z) = \varepsilon(x+a, y, z)$; here a is the lattice period. For simplicity, in most examples we shall take the "waveguide" as a genuinely 1D photonic crystal formed by a periodic stack of dielectric slabs ($\varepsilon(x) = \varepsilon(x+a)$) and restrict our attention to propagation along the x axis. However, it is underlined that it can be fully three-dimensional.

We admit that the wave propagation in the structure is determined by

76

some operator $\hat{H}(\mathbf{r}, -i\Delta)$ such that the time evolution of the system state vector Ψ, e.g., the electromagnetic field, is described by a Schrödinger-type dynamics $i\partial_t \Psi = \hat{H}\Psi$. The time evolution of any (eventually dispersive) electromagnetic platform can always be expressed in such a manner [9, 12, 25, 26]. For convenience, we designate $\hat{H}$ as the Hamiltonian.

Due to the periodicity along the x-direction, the eigenstates are Bloch waves labeled by a Bloch wave number q_x. The corresponding envelopes u_{q_x} (defined such that $\Psi_{q_x} = u_{q_x} e^{iq_x x}$) satisfy $\hat{H}(x, -i\partial_x + q_x)u_{q_x} = \omega_{q_x} u_{q_x}$ with ω_{q_x} the eigenfrequencies. Note that u_{q_x} can be a multi-component vector. The parameters y, z, $-i\partial_y$, $-i\partial_z$ are omitted from now on in the argument of the operator $\hat{H}$ as they are not relevant for the discussion.

Let us now add a second label (q_s) to the Hamiltonian related to a translation in space $s \to x - x_0$:

$$\hat{H}_{\mathbf{q}} \equiv \hat{H}_{q_x,q_s} = \hat{H}(x - x_0(q_s), -i\partial_x + q_x). \tag{5.1}$$

The coordinate shift x_0 is parameterized by q_s. In section 5.3, it will be shown that q_s may be understood as a "momentum" determined by a synthetic dimension. It is assumed that $x_0(q_s)$ is continuous and that $x_0(q_s + 2\pi) - x_0(q_s) = Na$, with a the spatial period of the waveguide and N some integer number. Since $\hat{H}(x, -i\partial_x + q_x) = \hat{H}(x - a, -i\partial_x + q_x)$, it follows that $\hat{H}_{q_x,q_s}$ is a periodic function of q_s with period 2π. In a full cycle, as q_s varies from $q_s = -\pi$ to $q_s = \pi$, the waveguide is displaced by N complete spatial periods towards the $+x$-direction.

Since the spectrum of $\hat{H}_{q_x,q_s}$ is cyclic in both q_x and q_s one can characterize its topological phases. To this end, consider a generic band of eigenfunctions $(\Psi_{q_x}(x))$ of the "waveguide": $\hat{H}(x, -i\partial_x)\Psi_{q_x}(x) = \omega_{q_x}\Psi_{q_x}(x)$. Then, it is obvious that $\hat{H}_{\mathbf{q}} u_{\mathbf{q}} = \omega_{\mathbf{q}} u_{\mathbf{q}}$ with $\mathbf{q} = (q_x, q_s)$, $\omega_{\mathbf{q}} = \omega_{q_x}$ and the envelope

$$u_{\mathbf{q}}(x) = \Psi_{q_x}(x - x_0(q_s))e^{-iq_x x} = u_{q_x}(x - x_0(q_s))e^{-iq_x x_0(q_s)}. \tag{5.2}$$

This property shows that the eigenvalues of $\hat{H}_{\mathbf{q}}$ are independent of q_s, and thereby the band-gaps of $\hat{H}_{\mathbf{q}}$ are the same as the band-gaps of the "waveguide". In other words, a translation in space does not alter the band structure.

The Bloch eigenmodes Ψ_{q_x} of $\hat{H}$ can be taken as smooth periodic functions of q_x in the 1D-Brillouin zone $-\pi/a \leq q_x \leq \pi/a$. The Chern number $\mathcal{C}$ associated with a given band of $\hat{H}_{\mathbf{q}}$ can be found in a standard way from the

Berry potential $\mathcal{A}_\mathbf{q} = i\langle u_\mathbf{q}|\partial_\mathbf{q} u_\mathbf{q}\rangle$ using $\mathcal{C} = \frac{1}{2\pi}\int_{-\pi/a}^{\pi/a} dq_1 \int_{-\pi}^{\pi} dq_2 \left(\frac{\partial \mathcal{A}_{2,\mathbf{q}}}{\partial q_1} - \frac{\partial \mathcal{A}_{1,\mathbf{q}}}{\partial q_2}\right)$ with $(q_1, q_2) \equiv (q_x, q_s)$. The eigenfunctions are normalized as $\langle u_\mathbf{q}|u_\mathbf{q}\rangle = 1$ with $\langle .|.\rangle$ the canonical inner product. Since the Berry potential is a smooth function in the interior of the integration domain, from the Stokes theorem the Chern number is:

$$
\begin{aligned}
\mathcal{C} =& \frac{1}{2\pi}\int_{-\pi/a}^{\pi/a} dq_x \left(\mathcal{A}_{1,\mathbf{q}}|_{q_s=-\pi} - \mathcal{A}_{1,\mathbf{q}}|_{q_s=+\pi}\right) \\
& + \frac{1}{2\pi}\int_{-\pi}^{\pi} dq_x \left(\mathcal{A}_{2,\mathbf{q}}|_{q_s=-\pi/a} - \mathcal{A}_{2,\mathbf{q}}|_{q_s=+\pi/a}\right).
\end{aligned}
\tag{5.3}
$$

Using $u_\mathbf{q}(x) = \Psi_{q_x}(x - x_0(q_s))e^{-iq_x x}$ one finds that $\mathcal{A}_{2,\mathbf{q}} = i\langle \Psi_\mathbf{q}|\partial_{q_s} \Psi_\mathbf{q}\rangle$ with $\Psi_\mathbf{q} \equiv \Psi_{q_x}(x - x_0(q_s))$. Noting that $i\langle \Psi_\mathbf{q}|\partial_{q_s} \Psi_\mathbf{q}\rangle$ is a periodic function of q_x, it follows that the second integral in the right-hand side of Eq. (5.3) vanishes. On the other hand, using $u_\mathbf{q}(x) = u_{q_x}(x - x_0(q_s))e^{-iq_x x_0(q_s)}$, we get

$$
\mathcal{A}_{1,\mathbf{q}} = i\langle u_{q_x}(x - x_0(q_s))|\partial_{q_x}[u_{q_x}(x - x_0(q_s))]\rangle + x_0(q_s).
\tag{5.4}
$$

We used $\langle u_\mathbf{q}|u_\mathbf{q}\rangle = 1$ and the periodicity of the envelope in x. The first term in the right-hand side of Eq. (5.4) is a periodic function of q_s because of the periodicity of the envelope in x. Thus, it does not contribute to the first integral in Eq. (5.3). Taking this into account, we obtain the first key result of the chapter

$$
\mathcal{C} = \frac{1}{2\pi}\int_{-\pi/a}^{\pi/a} dq_x(x_0(-\pi) - x_0(+\pi)) = -\frac{1}{a}[x_0(\pi) - x_0(-\pi)] = -N.
\tag{5.5}
$$

We used $x_0(q_s + 2\pi) - x_0(q_s) = Na$ in the last identity. The above formula proves that each photonic band of $\hat{H}_\mathbf{q}$ has a topological charge of "$-N$", i.e., identical to minus the number of displaced unit cells towards $+x$. Note that $\mathcal{C}$ has an integer value because $\hat{H}_\mathbf{q}$ satisfies the conditions of the Chern theorem. In particular, the gap Chern number of a given band-gap is identical to the number of bands (n_{bands}) below the gap multiplied by the number of shifted cells (N) in one q_s-cycle:

$$
\mathcal{C}_{\text{gap}} = -n_{\text{bands}} \times N.
\tag{5.6}
$$

Therefore, the number of photonic bands below the gap of a generic 1D-type photonic crystal can be understood as a topological number. The

topological charge of each band is acquired from the translational shift suffered by the waveguide. In other words, a translation in space effectively "pumps" topological charge into the system described by $\hat{H}_{\mathbf{q}}$. This property and its consequences are discussed in Section 5.3.

5.3 The synthetic dimension and bulk-edge correspondence

5.3.1 The synthetic dimension

Next, it is shown that $\hat{H}_{\mathbf{q}}$ can be regarded as the momentum-space operator of a system that consists of the original 1D-type waveguide (which as previously mentioned can be embedded in a three-dimensional space) with an additional synthetic dimension. Systems with synthetic dimensions were recently discussed in the literature to emulate physical and topological phenomena in higher dimensions (see e.g., [27–29]).

Consider a generic family of operators $\hat{H}_{\mathcal{K}} = (x, -i\partial_x)$ periodic both in $\mathcal{K}$ and x: $\hat{H}_{\mathcal{K}} = \hat{H}_{\mathcal{K}+2\pi}$ and $\hat{H}_{\mathcal{K}}(x, -i\partial_x) = \hat{H}_{\mathcal{K}}(x + a, -i\partial_x)$. The operator $\hat{H}_{\mathcal{K}}(x, -i\partial_x)$ may also depend on other space coordinates (y, z, etc) and space derivatives, but as they are not relevant for the analysis they are omitted. We introduce a matrix operator ($\hat{\mathcal{H}}_e$) that acts on a column state vector of the form $\Psi = [\Psi_m(x)] = [... \Psi_{-1} \quad \Psi_0 \quad \Psi_1 ...]^T$, $m = 0, \pm 1, \pm 2,...$, through a convolution:

$$\Psi \to \hat{\mathcal{H}}_e \Psi = [(\hat{H}_e \Psi)_n] \quad \text{where} \quad (\hat{\mathcal{H}}_e \Psi)_n = \sum_m \hat{H}_{n-m}(x, -i\partial_x) \Psi_m(x), \quad (5.7)$$

with $n = 0, \pm 1, \pm 2,...$. The matrix elements of $\hat{\mathcal{H}}_e$ are defined as:

$$\hat{H}_m(x, -i\partial_x) = \frac{1}{2\pi} \int_0^{2\pi} d\mathcal{K} \hat{H}_{\mathcal{K}}(x, -i\partial_x) e^{i\mathcal{K}m}. \qquad (5.8)$$

The state vector $\Psi = [\Psi_m(x)]$ has two space-type coordinates: x which corresponds to a continuous real-space coordinate, and m which corresponds to a discrete (lattice) coordinate. The coordinate m determines the synthetic dimension. The Bloch eigenfunctions are characterized by a state vector of the form $\Psi = [\Psi_m(x)]$ with $\Psi_m(x) = u_{k,\mathcal{K}}(x) e^{ikx} e^{im\mathcal{K}}$ and satisfy $\hat{\mathcal{H}}_e \Psi =$

$\omega_{k,\mathcal{K}}\Psi$, where $(k,\mathcal{K})$ is the two-dimensional Bloch wave vector $(-\pi/a \leq k \leq \pi/a$ and $-\pi \leq \mathcal{K} \leq \pi)$. Substituting $\Psi = [u_{k,\mathcal{K}}(x)e^{ikx}e^{im\mathcal{K}}]$ into Eq. (5.7) and using the Fourier synthesis relation $\hat{H}_{\mathcal{K}}(x, -i\partial_x) = \sum_n \hat{H}_n(x, -i\partial_x)e^{-in\mathcal{K}}$, it is found that the secular equation $\hat{\mathcal{H}}_e\Psi = \omega_{k,\mathcal{K}}\Psi$ reduces to:

$$\hat{H}_{\mathcal{K}}(x, -i\partial_x + k)u_{k,\mathcal{K}} = \omega_{k,\mathcal{K}}u_{k,\mathcal{K}}. \tag{5.9}$$

Thus, the operator $\hat{H}_{\mathcal{K}}(x, -i\partial_x + k)$ is the momentum-space version of $\hat{\mathcal{H}}_e$.

The previous theory can be readily applied to the family of operators $\hat{H}_{\mathbf{q}} = \hat{H}(x - x_0(q_s), -i\partial_x + q_x)$ considered in Sect. 5.2, with the obvious correspondence $(q_x, q_s) \leftrightarrow (k, \mathcal{K})$. In particular, $\hat{H}_{\mathbf{q}}$ is the momentum-space version of some operator $\hat{\mathcal{H}}_e$ defined on an extended-space determined by the continuous coordinate x (which varies in the "real-space") and by the discrete coordinate m (which varies along the synthetic lattice-type dimension). This property is important as it guarantees that the gap-Chern number can be linked to the number of edge-states through a bulk-edge correspondence [13, 30–34].

5.3.2 The bulk-edge correspondence

The bulk-edge correspondence establishes a precise relation between the gap Chern numbers of two topological materials and the net number of unidirectional edge states supported by a material interface [30–34]. There is a simple argument that justifies the emergence of edge-states at the interface of a topological system terminated with an "opaque" (impenetrable) electromagnetic boundary [13, 34]. Interestingly, the gap Chern number can be written as a volume integral of the Green's function of a large cavity terminated with periodic boundaries [13, 34]. The key point is that in a band-gap the Green's function evaluated in the interior of the cavity is insensitive to the boundary conditions on the walls. This is so because in a band-gap the radiation from a point-source in the interior of the cavity is unable to reach the walls. However, it turns out that if the cavity walls are "opaque", the integral that determines the Chern number (evaluated with the Green's function that satisfies the opaque-type boundary conditions) vanishes. The sensitivity of the Chern number integral to the boundary conditions forcibly implies the emergence of gapless edge states at "opaque"-type interfaces. For detailed arguments a reader is referred to Refs. [13,34] (see also Refs. [35,36]).

From the previous discussion, the Chern invariants of the operator $\hat{\mathcal{H}}_e$ determine a bulk-edge correspondence in the extended space with a synthetic dimension. Are there any consequences of this bulk-edge correspondence in real-space? To answer this question, consider two 1D-type periodic "waveguides", described by the (real-space) Hamiltonians $\hat{H}_1$ and $\hat{H}_2$, respectively. Suppose that the waveguides have a common band-gap. Furthermore, let us add a synthetic (discrete) dimension to each waveguide, such that the extended-space Hamiltonians are $\hat{\mathcal{H}}_{e1}$ and $\hat{\mathcal{H}}_{e2}$, with each of them described by a momentum-space Hamiltonian of the form $\hat{H}_{\mathbf{q},i} = \hat{H}_i(x - x_0^{(i)}(q_s), -i\partial_x + q_x)$, $i = 1, 2$. For definiteness, we take $x_0^{(i)}(q_s) \equiv N_i\Delta$, with N_i an integer and $\Delta = \frac{q_s}{2\pi}a$. Then, from Eq. (5.6) the gap Chern number difference in a common gap is:

$$\delta\mathcal{C}_{\text{gap}} \equiv \mathcal{C}_{gap,1} - \mathcal{C}_{\text{gap},2} = n_{\text{bands},2} \times N_2 - n_{\text{bands},1} \times N_1. \tag{5.10}$$

Here, $n_{\text{bands,i}}$ is the number of bands below the gap for the i-th waveguide. In particular, when the number of shifted cells in both waveguides is $N_2 = N_1 = 1$, the gap Chern number difference is given by the difference of the number of bands below the gap, which thereby is a topological quantity.

The bulk-edge correspondence implies that an interface of the two topological platforms supports $|\delta\mathcal{C}_{\text{gap}}|$ unidirectional gapless edge states. A generic interface in the extended space does not have an obvious real-space geometric interpretation. The exceptions are the *x=const.* interfaces, which correspond to standard real-space interfaces between the two waveguides (when the waveguides are embedded in 3D space, it is implicit that their cross-sections are identical).

Let us investigate the consequences of the bulk-edge correspondence for an interface *x=const.*, let us say $x = 0$. By definition, the edge states in the extended space must be localized near $x = 0$ and have a variation along the synthetic dimension (coordinate n) of the form e^{inq_s} with q_s the wave number of the edge state in the synthetic dimension: $\Psi = [\Psi_n(x)]$ with $\Psi_n(x) = \Psi(x)e^{inq_s}$ ($n = 0, \pm 1, \pm 2, ...$). Evidently, the edge states projection into real-space ($\Psi_0(x) = \Psi(x)$) corresponds to a wave trapped at the interface $x = 0$ of the two waveguides. A fixed q_s in extended space corresponds to a spatial shift $x_0^{(i)} = N_i\frac{q_s}{2\pi}a$ in real-space. Thus, as q_s varies from 0 to 2π the internal structure of the i-th waveguide is displaced by N_i cells. For some particular combinations of the shifts the $x = 0$ interface can support trapped (localized) states. The bulk-edge correspondence establishes that the number

of gapless "trapped states" branches in real-space is precisely $|\delta\mathcal{C}_{\text{gap}}|$, which is another of the key results of the chapter.

5.3.3 Numerical examples

To illustrate the developed ideas, we consider the case where the "waveguides" are 1D photonic crystals formed by stacked dielectric slabs (see Fig. 5.1(ai) for the geometry of a generic binary photonic crystal). The band structure of a 1D photonic crystal can be calculated by using an equivalence with transmission lines (see Appendix A). The unit cell of the crystal is formed by an arbitrary number (N) of layers (see Fig. 5.7(a), left for the case $N = 3$).

Consider now the scenario where two photonic crystals are paired to form an interface at $x = 0$ (Fig. 5.2(ai)). The semi-space $x < 0$ is filled with a photonic crystal modeled by $\hat{H}_1(x - x_0^{(1)}(q_s), -i\partial_x)$, and the semi-space $x > 0$ by a photonic crystal modeled by $\hat{H}_2(x - x_0^{(2)}(q_s), -i\partial_x)$ with $x_0^{(i)} = N_i\Delta$. The trapped states at an interface ($x = 0$) between two semi-infinite photonic crystals are forcibly decaying in space Bloch modes of the infinite photonic crystals in the regions $x > 0$ and $x < 0$. Thereby, since the current and voltage of the equivalent circuit are continuous at the interface $x = 0$, the localized trapped states must satisfy [39]:

$$Z_{\text{L}}^{(1)}(-N_1\Delta, \omega) + Z_{\text{R}}^{(2)}(-N_2\Delta, \omega) = 0. \tag{5.11}$$

Here, $Z_{\text{L}}^{(i)}$ and $Z_{\text{R}}^{(i)}$ are the left- and right- Bloch impedances of the i-th photonic crystal. Each value of $\Delta = \frac{q_s}{2\pi}a$ corresponds to a specific spatial-shift of the inner structure of the photonic crystals. In one full q_s-cycle, the parameter Δ varies from $\Delta = 0$ to $\Delta = a$. The effect of shifting the geometry of a generic photonic crystal is illustrated in Figs. 5.1(a*ii*) and 5.1(aiii).
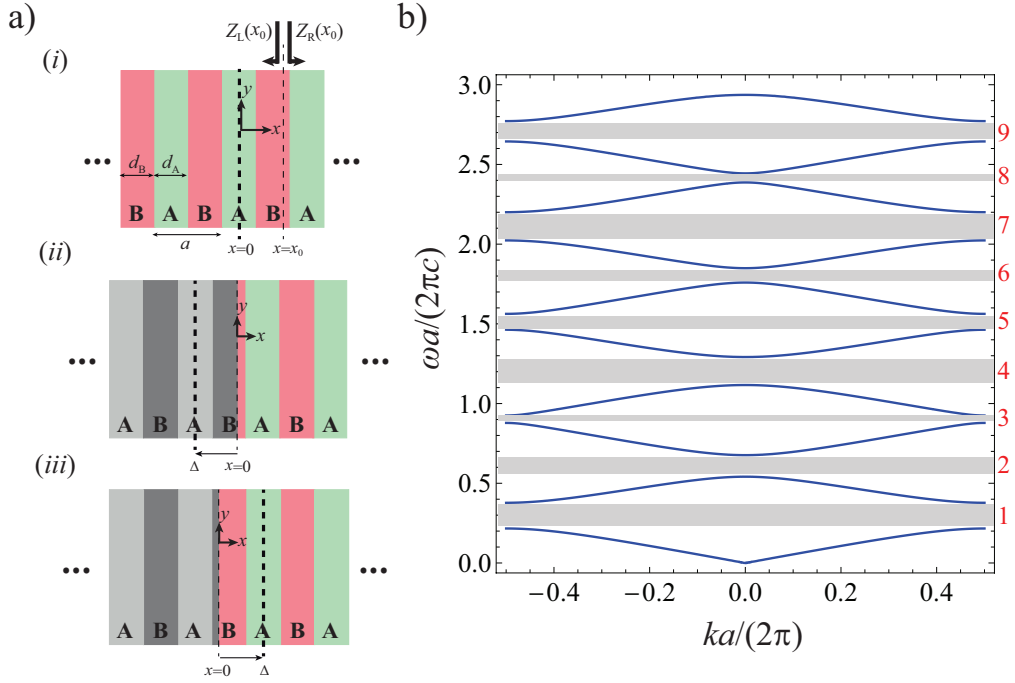
Figure 5.1: (a) (*i*) Structure of a binary photonic crystal formed by two phases A and B. The left and right Bloch surface impedances calculated at the generic plane $x = x_0$ are indicated in the figure. The $x = 0$ plane is placed at the middle of slab A (center of symmetry). (*ii*) Representation of a negative displacement of the geometry of the photonic crystal. (*iii*) Representation of a positive displacement of the geometry. The areas shaded in grey are cut-way from the structure when another photonic crystal is inserted into the region $x < 0$. (b) Band structure of a photonic crystal (blue solid curves) with parameters $\varepsilon_a = 7$, $\varepsilon_B = 1$, $\mu_A = \mu_B = 1$, $d_A = 0.4a$ and $d_B = 0.6a$. The grey strips represent the band gaps. Each band gap is numbered with a red label.

In the first example, we suppose that the semi-space $x < 0$ is a perfectly electric conducting (PEC) wall, so that $Z_{\mathrm{L}}^{(1)} = 0$. The semi-space $x > 0$ is filled with a binary photonic crystal with a unit cell formed by two dielectric slabs A and B of thickness d_{A} and d_{B}, and relative dielectric permittivity and permeability ε_{A}, μ_{A} and ε_{B}, μ_{B}, respectively [see Fig. 5.1(a)]. The structural parameters are taken as $\varepsilon_{\mathrm{A}} = 7$, $\varepsilon_{\mathrm{B}} = 1$, $\mu_{\mathrm{A}} = \mu_{\mathrm{B}} = 1$, $d_{\mathrm{A}} = 0.4a$ and $d_{\mathrm{B}} = 0.6a$. Figure 5.1(b) shows the numerically calculated band structure (ω vs $k \equiv q_x$) with the band gaps shaded in grey. Since for the PEC semi-space $\mathcal{C}_{\mathrm{gap},1} = 0$, it follows that the gap-Chern number difference is $\mathcal{C}_{\mathrm{gap}} = n_{\mathrm{bands},2} \times N_2$ [Eq. (5.10)]. Note that the gap Chern number of the dielectric photonic crystal with the synthetic dimension is nonzero, even though the structure in real-space is reciprocal. In fact, the time-reversal symmetry in real-space does not imply a time-reversal symmetry in the extended space.

Suppose that $N_2 = -1$ so that the photonic crystal is displaced by a complete period along the negative x-axis in a full Δ-cycle [Fig. 5.1(aii)]. The dispersion of the interface states as a function of the spatial shift Δ is determined by $Z_{\mathrm{R}}^{(2)}(\Delta, \omega) = 0$. The corresponding solutions in the band-gaps are plotted in Fig. 5.2(b) (blue curves). As seen, in agreement with the bulk-edge correspondence, $\delta\mathcal{C}_{\mathrm{gap}} = -n_{\mathrm{bands},2}$, the number of branches $\omega = \omega_n(\Delta)$ in each gap is exactly coincident with the number of bands below the gap. Each branch $\omega_n(\Delta)$ crosses completely the band-gap, and all the branches have a positive slope vs. Δ indicating that they are unidirectional gapless states in the extended space with the synthetic dimension. Our formalism enables to predict in a simple manner how many (defect-type) trapped states occur in real-space for a fixed frequency in the band-gap, when the geometry of the crystal is displaced by one period. The number of trapped states is exactly the number of bands below the gap. The operation of a "spatial shift" by one period may be regarded as a "topological pump" that inserts topological charge into the system. The topological charge is identical to the number of bands below the gap. The topological invariant manifests itself as the number of trapped states branches at the interface in a band gap.
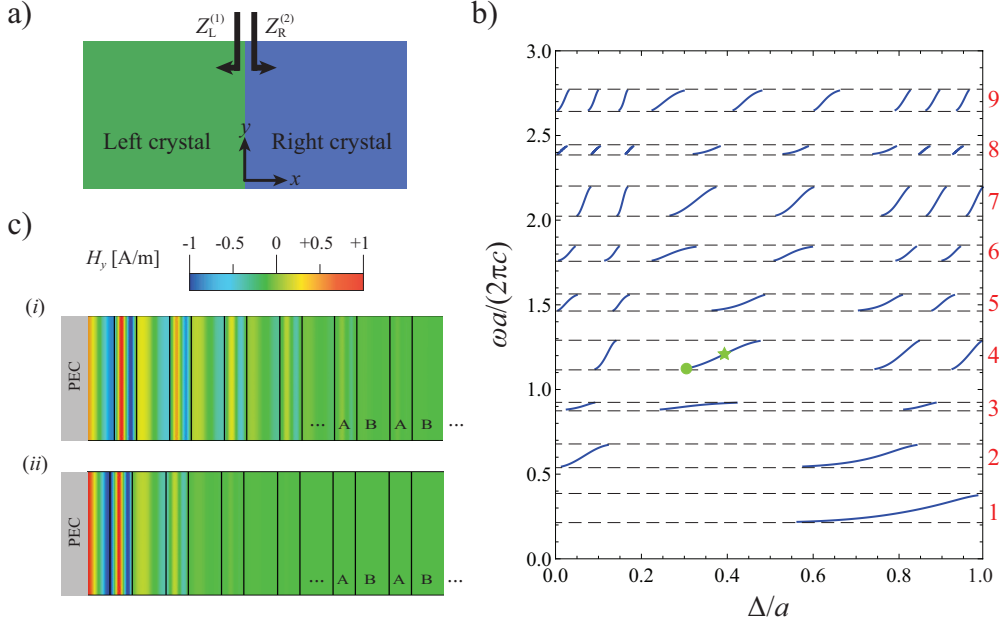
Figure 5.2: (a) Representation of the pairing of two different photonic crystals. (b) Interface state solutions for a photonic crystal with the same parameters as in Fig. 5.1(b) in the right semi-space, and a PEC material in the left semi-space. The grey horizontal dashed lines delimit the band gaps which are numbered by the red labels. (c) Time-snapshot of the magnetic field of the interface state in the fourth gap for (i) the solution marked by the green circle with $\Delta/a = 0.3$, and (ii) the solution marked by the green star with $\Delta/a = 0.38$.

The profile of two trapped states in the fourth band gap are represented in Fig. 5.2(c). The field profiles were obtained using CST Microwave Studio [40]. As seen, the trapped states are confined to the interface of the photonic crystal and of the PEC, and decay exponentially into the bulk region. As could be expected, the trapped mode in the center of the band gap (Fig. 5.2(c)(ii) for $\Delta = 0.38$) is much more confined to the interface than the one near the bottom edge of the band gap (Fig. 5.2(c)i for $\Delta = 0.30$).

In the second example, the PEC region in the semi-space $x < 0$ is replaced by a binary photonic crystal with parameters $\varepsilon_{A,l} = 2$, $\varepsilon_{B,l} = 1$, $\mu_{A,l} = \mu_{B,l} = 1$, $d_{A,l} = 0.4a$ and $d_{B,l} = 0.6a$, with the photonic crystal in the semi-space

$x > 0$ the same as before. Figure 5.3(a) shows the band structures of the right (blue solid curve) and left (green dashed curve) crystals. There are two common frequency band gaps highlighted with the shaded grey strips. Consider first the situation wherein one of the photonic crystals is held fixed, while the other crystal is displaced by one cell period to the negative x direction. Figure 5.3(b) depicts the interface states dispersion $\omega = \omega_n(\Delta)$ in the two common gaps for the two possible displacements: i) the left crystal is held fixed and the right crystal slides to the left [blue solid curves; $N_1 = 0$ and $N_2 = -1$ in Eq. (5.11)], ii) the right crystal is held fixed and the left crystal slides to the left [green dashed curves; $N_1 = -1$ and $N_2 = 0$ in Eq. (5.11)]. For the case i) [case ii)] the number of solution branches is identical to the number of bands of the right [left] crystal below the gap, consistent with the bulk-edge correspondence [see Eq. (5.10)]. The slope of the curves $\omega = \omega_n(\Delta)$ is different in the two cases. This property is explained by the fact that $\delta \mathcal{C}_{\text{gap}}$ has a different sign in each case. Indeed, the sign of $\delta \mathcal{C}_{\text{gap}}$ is linked to the angular momentum of the edge modes in a closed system [34, 41, 42]. Thereby, the direction of the energy flow in the extended space must change when the gap Chern number sign changes.

We also studied the situations where the materials inner structures are simultaneously displaced to the negative x-direction $N_1 = N_2 = -1$ (blue solid curves in Fig. 5.3(c), or, alternatively, the right crystal is displaced to the negative x-direction and the left crystal to the positive x-direction ($N_1 = 1$ and $N_2 = -1$) (green dashed curves in Fig. 5.3(c)). In both cases, it is observed that the number of trapped states branches in a common band gap is identical to $|\delta \mathcal{C}_{\text{gap}}| \equiv |n_{\text{bands},2} \times N_2 - n_{\text{bands},1} \times N_1|$. For example, for the lowest frequency gap $n_{\text{bands},2} = 4$ and $n_{\text{bands},1} = 3$. Consistent with this property, one observes a single gapless trapped state branch when $N_1 = N_2 = -1$ and 7 gapless trapped states branches when $N_1 = -N_2 = 1$.
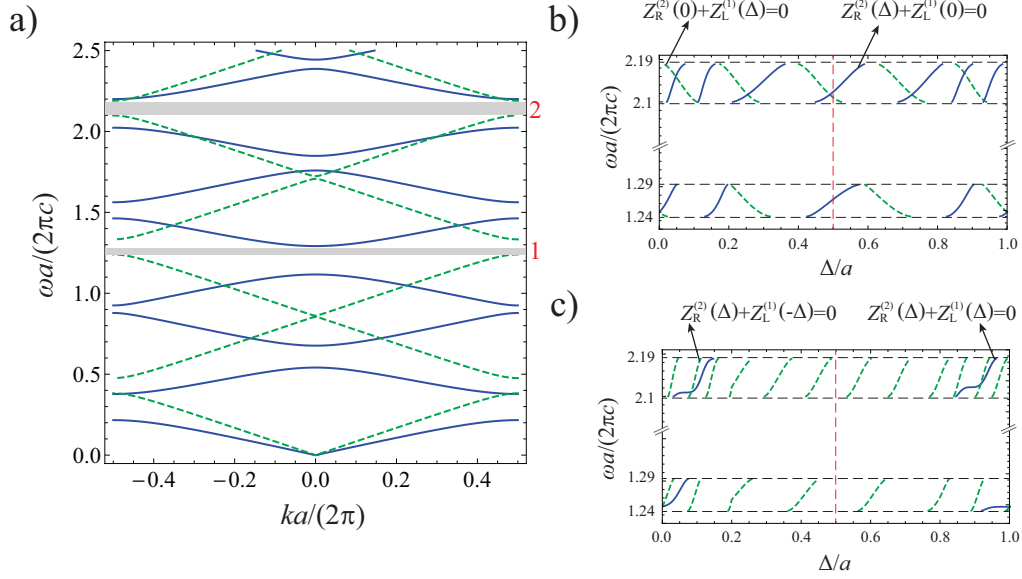
Figure 5.3: (a) Green dashed curves: band structure of binary photonic crystal with parameters $\varepsilon_{A,l} = 2$, $\varepsilon_{B,l} = 1$, $\mu_{A,l} = \mu_{B,l} = 1$, $d_{A,l} = 0.4a$ and $d_{B,l} = 0.6a$. Blue curves: band structure of the same photonic crystal as in Fig. 5.1. The grey strips indicate the common band gaps and the red labels the gap number. (b) Dispersion of the interface states in the common band gaps for a negative displacement of one of the crystals with the other held fixed. Blue solid curves: right photonic crystal slides one cell to the left; green dashed curves: left photonic crystal slides one cell to the left. (c) Similar to (b) but for a situation where both crystals geometries suffer a negative spatial shift (blue solid curves, $N_1 = N_2 = -1$), or alternatively the left crystal suffers a positive spatial shift and the right crystal a negative spatial shift (green dashed curves, $N_1 = 1$ and $N_2 = -1$).

We verified that the bulk-edge correspondence also holds true in other more complex 1D photonic crystal geometries. For example, consider the case where the left photonic crystal of the previous example is replaced by a ternary layered structure with parameters $\varepsilon_{A,l} = 2$, $\varepsilon_{B,l} = 1$, $\varepsilon_{C,l} = 3$, $\mu_{A,l} = \mu_{B,l} = \mu_{C,l} = 1$, $d_{A,l} = 0.3a$, $d_{B,l} = 0.6a$ and $d_{C,l} = 0.1a$. Different from the binary crystals considered in the previous examples, the ternary crystal does not have inversion (parity) symmetry. Figure 5.4 reports a study identical to that of Fig. 5.3, when the ternary photonic crystal (region $x < 0$) is paired with the same binary photonic crystal as in Fig. 5.2. The results are qualitatively analogous to those of Fig. 5.3 and again confirm that it is possible to predict the number of trapped states from the knowledge of the number of bands below the band-gap.

Furthermore, we also studied the emergence of interface states in 1D-type waveguides embedded in a two-dimensional real-space. Specifically, consider a waveguide with metallic lateral walls constructed from a 2D photonic crystal with the unit cell represented in Fig. 5.5(a). The lateral width of the guide is $N_y a$ and the electric field is oriented along the z-direction. The corresponding band-diagram for propagation along the x-direction is represented in Figs. 5.5(b) and 5.5(c) for the cases $N_y = 5$ and $N_y = 6$, respectively. The band diagram is numerically calculated with CST Microwave Studio [40]. The band-gaps are shaded in gray. We terminated this waveguide (positioned in the semi-space $x > 0$) with a metallic plate placed at $x = 0$, and numerically found the edge states for different shifts of the waveguide geometry. The trapped states dispersion $\omega = \omega_n(\Delta)$ is shown in Figs. 5.5(d) and 5.5(e). We consider displacements along the negative ($N_2 = -1$, blue curves) and positive ($N_2 = 1$, green dashed curves) x-axis. As seen, also for this more complex system, the number of branches agrees with the number of bands of the waveguide below the gap. Furthermore, as expected, the slope of the curves $\omega = \omega_n(\Delta)$ depends on the displacement direction.
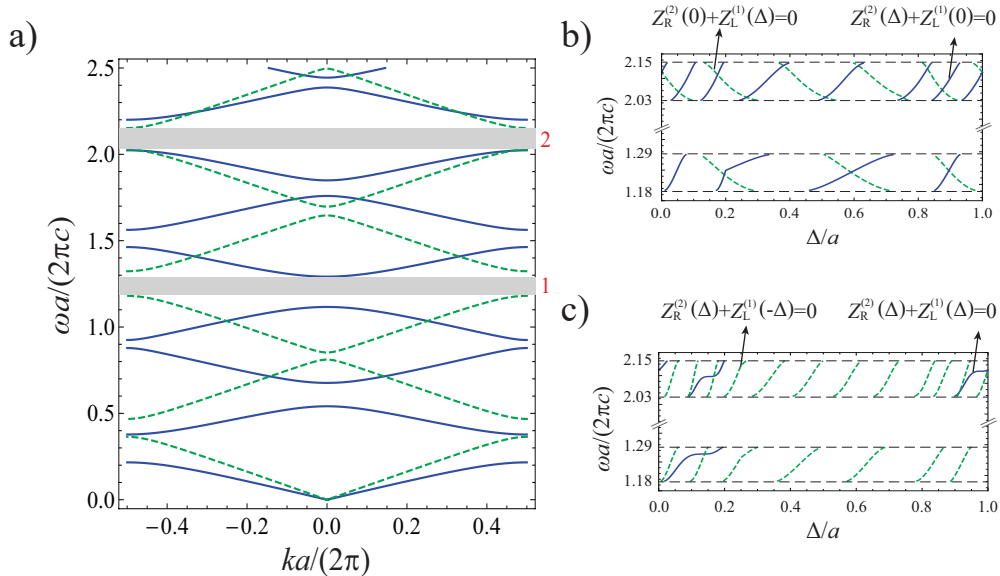
Figure 5.4: Analogous to Fig. 5.3(a) for the case where the photonic crystal in the semi-space $x < 0$ is replaced by a ternary photonic crystal with parameters $\varepsilon_{A,l} = 2$, $\varepsilon_{B,l} = 1$, $\varepsilon_{C,l} = 3$, $\mu_{A,l} = \mu_{B,l} = \mu_{C,l} = 1$, $d_{A,l} = 0.3a$, $d_{B,l} = 0.6a$ and $d_{C,l} = 0.1a$. The band structure of the ternary photonic crystal is represented with green dashed curves in panel (a).
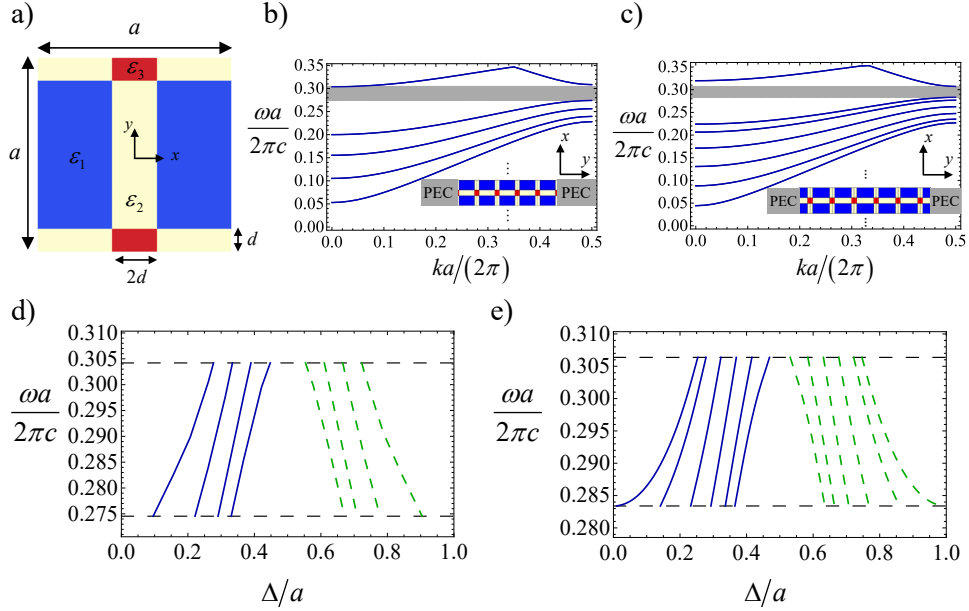
Figure 5.5: (a) Unit cell of a 2D photonic crystal with $\varepsilon_1 = 1$, $\varepsilon_2 = 6.5$ and $\varepsilon_3 = 12$. The unit cell period is a. The geometrical parameter represented in the figure is $d = 0.115a$. (b) Band diagram of the waveguide with metallic lateral walls constructed from a 2D photonic crystal with 5 unit cells along the y-direction. The shaded grey strip indicates the band gap of the waveguide. (c) Similar to (b) but for a waveguide constructed from a 2D photonic crystal with 6 unit cells along the y-direction. (d) Dispersion of the interface states in the band gap for a waveguide constructed from a 2D photonic crystal with 5 unit cells along the y-direction, placed in the semi space $x > 0$ and terminated with a metallic plate placed at $x = 0$. The waveguide geometry is continuously displaced by one lattice period along the x-direction. Blue solid curves: negative displacement ($N_2 = -1$). Green dashed curves: positive displacement ($N_2 = 1$). (e) Similar to (d) but for a waveguide constructed from a 2D photonic crystal with 6 unit cells along the y-direction.

90

5.4 Fractional Chern systems

5.4.1 Non-integer Chern numbers

Consider now some 1D-type "waveguide" system with inversion symmetry described by a real-space Hamiltonian $\hat{H}(x, -i\partial_x)$. Different from the previous section, here it is supposed that the state vector Ψ (in real-space) is a scalar function.

We consider again the Hamiltonian $\hat{H}_\mathbf{q} = \hat{H}(x - x_0(q_s), -i\partial_x + q_x)$ with eigenfunctions $u_\mathbf{q}(x) = \Psi_{q_x}(x - x_0(q_s))e^{-iq_x x}$ [Eq. (5.2)]. However, different from Sect. 5.2, here it is assumed that $x_0(q_s + 2\pi) - x_0(q_s) = N \times a/2$, so that the number of displaced cells in one cycle is *half* of an integer, which is a fractional number when N is odd. In particular, it follows that $\hat{H}_\mathbf{q}$ is a *discontinuous* function in the $\mathbf{q}$-parameter space when N is odd.

Following the same steps as in Sect. 5.2, still assuming that $\Psi_{q_x}(x)$ is picked as a smooth periodic function of q_x, one can show that the Chern number of a given band of $\hat{H}_\mathbf{q}$ is determined by the first term in the right-hand side of Eq. (5.3):

$$\mathcal{C} = \frac{1}{2\pi} \int_{-\pi/a}^{\pi/a} dq_x (\mathcal{A}_{1,\mathbf{q}}|_{q_s=-\pi} - \mathcal{A}_{1,\mathbf{q}}|_{q_s=+\pi}). \tag{5.12}$$

Suppose without loss of generality that $x_0(-\pi) = 0$. Then, it is seen that $\mathcal{A}_{1,\mathbf{q}}|_{q_s=-\pi} = \mathcal{A}_{q_x}$ and $\mathcal{A}_{1,\mathbf{q}}|_{q_s=\pi} = \tilde{\mathcal{A}}_{q_x}$ with $\mathcal{A}_{q_x} = i\langle u_{q_x}|\partial_{q_x} u_{q_x}\rangle$ and $\tilde{\mathcal{A}}_{q_x} = i\langle \tilde{u}_{q_x}|\partial_{q_x} \tilde{u}_{q_x}\rangle$ with $u_{q_x}(x) \equiv \Psi_{q_x}(x)e^{-iq_x x}$ and $\tilde{u}_{q_x}(x) \equiv \Psi_{q_x}(x - Na/2)e^{-iq_x x}$. The integrals $\theta_{\text{Zak}} = \int_{-\pi/a}^{\pi/a} dq_x \mathcal{A}_{q_x}$ and $\tilde{\theta}_{\text{Zak}} = \int_{-\pi/a}^{\pi/a} dq_x \tilde{\mathcal{A}}_{q_x}$ are by definition the Zak phases determined by the symmetry centers $x = 0$ and $x = Na/2$ of the original periodic 1D system [39]. Thereby, from Eq. (5.12) we get:

$$\mathcal{C} = \frac{1}{2\pi}(\theta_{\text{Zak}} - \tilde{\theta}_{\text{Zak}}). \tag{5.13}$$

The Zak phase is gauge dependent, i.e. it can vary modulo 2π with Ψ_{q_x}. Interestingly, it is shown in the Appendix B that for a scalar Hamiltonian the difference of the Zak phases $\tilde{\theta}_{\text{Zak}} - \theta_{\text{Zak}}$ is gauge independent, when both $\tilde{\theta}_{\text{Zak}}, \theta_{\text{Zak}}$ are evaluated using the same gauge. Specifically, it turns out that $\tilde{\theta}_{\text{Zak}} = \theta_{\text{Zak}} + N\pi$ [Eq. (5.33)]. This proves that:

$$\mathcal{C} = -\frac{1}{2}N. \tag{5.14}$$

91

Thereby, a half-of-cycle pump yields a *fractional gap* Chern number that is identical to the number of bands below the gap multiplied by $N/2$:

$$\mathcal{C}_{\text{gap}} = -\frac{n_{\text{bands}}}{2}N. \qquad (5.15)$$

This is another key finding of the paper. Evidently, the non-integer gap Chern number is insensitive to any perturbations of the system that do not close the band-gap. The fractional Chern number occurs because the operator $\hat{H}_{\mathbf{q}}$ is discontinuous: $\hat{H}_{q_x,q_s} \neq \hat{H}_{q_x,q_s+2\pi}$ when N is odd. The quantization of the Chern number is rooted in the parity symmetry of the system.

5.4.2 Fractional bulk-edge correspondence

Similar to Sect. 5.3, it is possible to add a synthetic dimension to the system so that $\hat{H}_{\mathbf{q}}$ is the momentum-space version of some $\hat{\mathcal{H}}_e$ operator defined in an extended space of coordinates. Is there any manifestation of the fractional topological number $\mathcal{C}_{\text{gap}}$ in the real-space?

Unfortunately, the standard bulk-edge correspondence is not directly applicable to systems with a fractional Chern number [13, 30–34]. However, motivated by the findings of the previous section, we conjecture that an interface of inversion-symmetric systems with a fractional (half-integer) Chern numbers supports a number of edge state branches equal to $|\delta\mathcal{C}_{\text{gap}}| = |\mathcal{C}_{\text{gap},1} - \mathcal{C}_{\text{gap},2}| = |n_{\text{bands},2} \times N_2 - n_{\text{bands},1} \times N_1|$ when $x_0^{(i)} = N_i\Delta$ and Δ varied in half-cycle $0 \leq \Delta \leq a/2$. The counting of the edge mode branches is done with the following rules i) if an edge-mode branch is completely contained in $0 \leq \Delta \leq a/2$ it counts as "one" branch. ii) if the edge-mode branch intersects the "momentum" boundaries $\Delta = 0$ and $\Delta = a/2$ it counts as half-branch. Note that in case ii) the edge modes are not gapless with respect to the momentum domain $0 \leq \Delta \leq a/2$. This is a consequence of the discontinuous nature of $\hat{H}_{\mathbf{q}}$ at $\Delta = 0$ and $\Delta = a/2$. It is underlined that $\Delta = 0$ and $\Delta = a/2$ correspond to the configurations for which the system has inversion symmetry with respect to the origin ($x = 0$). Importantly, the notion of parity-symmetry cannot be unambiguously applied to a PEC boundary or to other opaque-type boundaries. Thus, such opaque-type boundaries are excluded from the proposed fractional bulk-edge correspondence.

We did extensive numerical simulations to test the conjectured bulk-edge correspondence for fractional Chern systems formed by dielectric photonic

crystals. Here, we report the results obtained for two representative configurations: an interface formed by pairing two binary crystals [example of Fig. 5.3 discussed previously] and an interface formed by pairing a binary photonic crystal with a quaternary inversion symmetric crystal [Fig. 5.6]. Note that binary photonic crystals are always inversion symmetric.
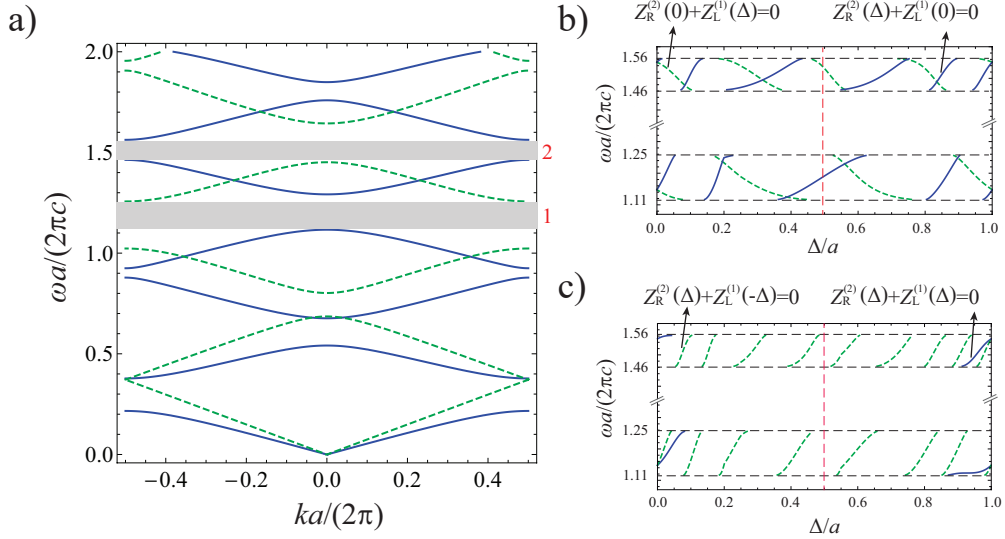

Figure 5.6: (a) Green dashed curves: band structure of a quaternary photonic crystal with inversion symmetry and parameters $\varepsilon_{A,l} = 2$, $\varepsilon_{B,l} = 1$, $\varepsilon_{C,l} = 4$, $\varepsilon_{D,l} = 1$, $\mu_{A,l} = \mu_{B,l} = \mu_{C,l} = \mu_{D,l} = 1$, $d_{A,l} = 0.5a$, $d_{B,l} = 0.2a$, $d_{C,l} = 0.1a$ and $d_{D,l} = 0.2a$. Blue curves: band structure of the same photonic crystal as in Fig. 5.1. The grey strips indicate the common band gaps and the red labels the gap number. (b)-(c) Same legend as in Fig. 5.3 with the quaternary photonic crystal in the semi-space $x < 0$ and the binary photonic crystal in the semi-space $x > 0$. The number of trapped-states branches in half-cycle $(0 < \Delta/a < 0.5)$ is determined by a fractional Chern number.

In both examples, we computed the trapped states for a full-cycle spatial shift $(0 \leq \Delta \leq a/2)$. The relevant part of the dispersion diagram for fractional Chern insulators is the range $0 \leq \Delta \leq a/2$. The simplest way to check that the proposed bulk edge correspondence works is to verify that the number of branches on the left-hand side of the line $\Delta = a/2$ (marked by the dashed red vertical line in Figs. 5.3 and 5.6 is exactly the same as the

number of branches on the right-hand side of the line $\Delta = a/2$. Evidently, the trapped states dispersions plotted in Figs. 5.3 and 5.6 have this property. Note that similar to Sect. 5.3 we consider systems with $N_1 = 0$ and $N_2 = -1$, with $N_1 = -1$ and $N_2 = 0$, with $N_1 = N_2 = -1$, and with $N_1 = -N_2 = 1$. For example, in Fig. 5.6(c), $|\delta\mathcal{C}_{\mathrm{gap}}| = 7/2$ for the low-frequency gap and $|\delta\mathcal{C}_{\mathrm{gap}}| = 9/2$ for the high-frequency gap, for the case $N_1 = -N_2 = 1$ (dashed green lines). Consistent with the value of $|\delta\mathcal{C}_{\mathrm{gap}}|$, the low (high) frequency gap contains 3 (4) gapless trapped state branches and 1 gapped trapped state branch at $\Delta = 0$ in the momentum range $0 \leq \Delta \leq a/2$ (half-cycle pumping). The gapped (at $\Delta = 0$) trapped state gives the contribution $1/2$ to $|\delta\mathcal{C}_{\mathrm{gap}}|$. It can be checked that all the other plots are consistent with the conjectured bulk-edge correspondence.

It should be noted that our theory is totally different from that of Ref. [39], which predicts the emergence of interface states in one-dimensional inversion-symmetric photonic crystals from the sign of the imaginary part of the Bloch impedance calculated at an inversion symmetry plane. The sign of the Bloch impedance depends on the gap Zak phase and on the number of passbands below the gap. Different from [39], our theory predicts the precise number of edge state branches created when the crystals are displaced by a half-integer number of lattice periods.

For half-cycle pumping of a single crystal, let us say of the left crystal ($N_1 = \pm 1$ and $N_2 = 0$), the gap Chern number is $|\delta\mathcal{C}_{\mathrm{gap}}| = n_{1,\mathrm{bands}}/2$. Thus, in this scenario, the gap Chern number is non-integer when the displaced crystal has an *odd* number of bands below gap. Clearly, for $|\delta\mathcal{C}_{\mathrm{gap}}|$ non-integer the proposed fractional bulk-edge correspondence implies the emergence of a trapped state at one and only one of the symmetry centers $\Delta = 0$ and $\Delta = a/2$ (e.g., see the green dashed lines in the first common gap in Fig. 5.3(b)). In contrast, when is an integer (number of bands of the displaced crystal below the gap is an even number) the fractional bulk-edge correspondence implies that either both or none of the symmetry centers $\Delta = 0$ and $\Delta = a/2$ supports trapped edge states. The enunciated results are rather general and apply to arbitrary values of N_1, N_2.

5.5 Conclusions

In summary, it was shown that in one-dimensional periodic systems the number of bands below a gap can be understood as a Chern topological number

of an extended system with a synthetic dimension. This topological number determines the number of edge states in the extended space with the synthetic dimension. The real-space projection of the edge states are modes localized at the boundary of the 1D crystal, for some shift of the unit cell. The number of trapped states branches "pumped" by a full-lattice period displacement equals the number of bands below the gap. This result does not require any particular symmetry, and establishes a rigorous and simple bulk-edge correspondence for interfaces of one-dimensional systems.

Moreover, it was shown that in inversion-symmetric systems a displacement by a half-lattice period in real-space determines an extended space Hamiltonian with a fractional Chern number equal to the number of bands below the gap divided by two. The non-integer Chern number is due to the discontinuous nature of the Hamiltonian associated with the half-cycle topological pump. We conjecture that dielectric systems with a fractional topological charge obey a fractional bulk-edge correspondence that links the number of trapped-states branches with the fractional Chern number. Thereby, our work determines an entirely novel and intriguing class of topological systems with fractional topological charge, which may lead to rather unique physical effects and phenomena.

Appendix A: Dispersion equation and Bloch impedance of a 1D photonic crystal

As is well-known, the wave propagation in a 1D photonic crystal is formally equivalent to the propagation in a periodic transmission line (Fig. 5.7(a)). Thus, the characteristic equation for the Bloch waves can be easily found using the ABCD-matrix formalism [38]. To this end, one needs to find the ABCD-matrix for a unit cell, which links the input and output voltages and currents as:

$$\begin{pmatrix} V1 \\ I1 \end{pmatrix} = \begin{pmatrix} A & B \\ C & D \end{pmatrix}_{\text{global}} \begin{pmatrix} V2 \\ I2 \end{pmatrix}. \qquad (5.16)$$

From the theory of microwave networks, the global ABCD matrix is given by the product of the ABCD matrices of the uniform line sections:

$$\mathbf{M} \equiv \begin{pmatrix} A & B \\ C & D \end{pmatrix}_{\text{global}} = \begin{pmatrix} A & B \\ C & D \end{pmatrix}_1 \cdots \begin{pmatrix} A & B \\ C & D \end{pmatrix}_N. \tag{5.17}$$

In the above,

$$\begin{pmatrix} A & B \\ C & D \end{pmatrix}_i = \begin{pmatrix} \cosh(\gamma_i d_i) & Z_{c,i} \sinh(\gamma_i d_i) \\ Z_{c,i}^{-1} \sinh(\gamma_i d_i) & \cosh(\gamma_i d_i) \end{pmatrix}, \quad i = 1, 2, 3, ..., N \tag{5.18}$$

is the ABCD matrix of the ith section, $Z_{c,i} = \eta_0 \sqrt{\mu_i/\varepsilon_i}$ is the wave impedance and $\gamma_i = -i\frac{\omega}{c}\sqrt{\mu_i \varepsilon_i}$ is the propagation constant. Here, η_0 is the free-space impedance and c is the speed of light in vacuum. The permittivity and permeability ε_i, μ_i are normalized to the free-space values.

For Bloch waves the input and output voltages are linked by $(V2 \quad I2)^T = e^{\gamma a}(V1 \quad I1)^T$ with $\gamma = \alpha - ik$ the (complex) propagation constant of the Bloch mode. Thus, using Eq. (5.16) one finds that the "output" voltages and currents satisfy the homogeneous equation:

$$\left(\mathbf{M} - \mathbf{1}e^{+\gamma a}\right) \cdot \begin{pmatrix} V2 \\ I2 \end{pmatrix} = 0, \tag{5.19}$$

with $\mathbf{M}$ the global ABCD matrix defined as in Eq. (5.17). This result implies that $det(\mathbf{M} - \mathbf{1}\lambda) = 0$, or equivalently $\lambda^2 - \lambda tr(\mathbf{M}) + det(\mathbf{M}) = 0$, with $\lambda = e^{+\gamma a}$. Since the system under analysis is reciprocal, one has $det(\mathbf{M}) = 1$ [38]. The solutions of the second degree equation are $\lambda_{1,2} = \frac{tr(\mathbf{M})}{2} \pm \sqrt{[\frac{tr(\mathbf{M})}{2}]^2 - 1}$. Because of $\lambda_{1,2} = e^{\pm\lambda a}$, one has $e^{+\lambda a} + e^{-\lambda a} = \lambda_1 + \lambda_2 = tr(\mathbf{M})$. This implies that the characteristic equation for the Bloch waves is

$$\cosh(\gamma a) = \frac{tr(\mathbf{M})}{2}. \tag{5.20}$$

Finally, the photonic band structure of the crystal is found by looking for solutions of the eq. (5.20) with $\gamma = -ik$ a purely imaginary number.
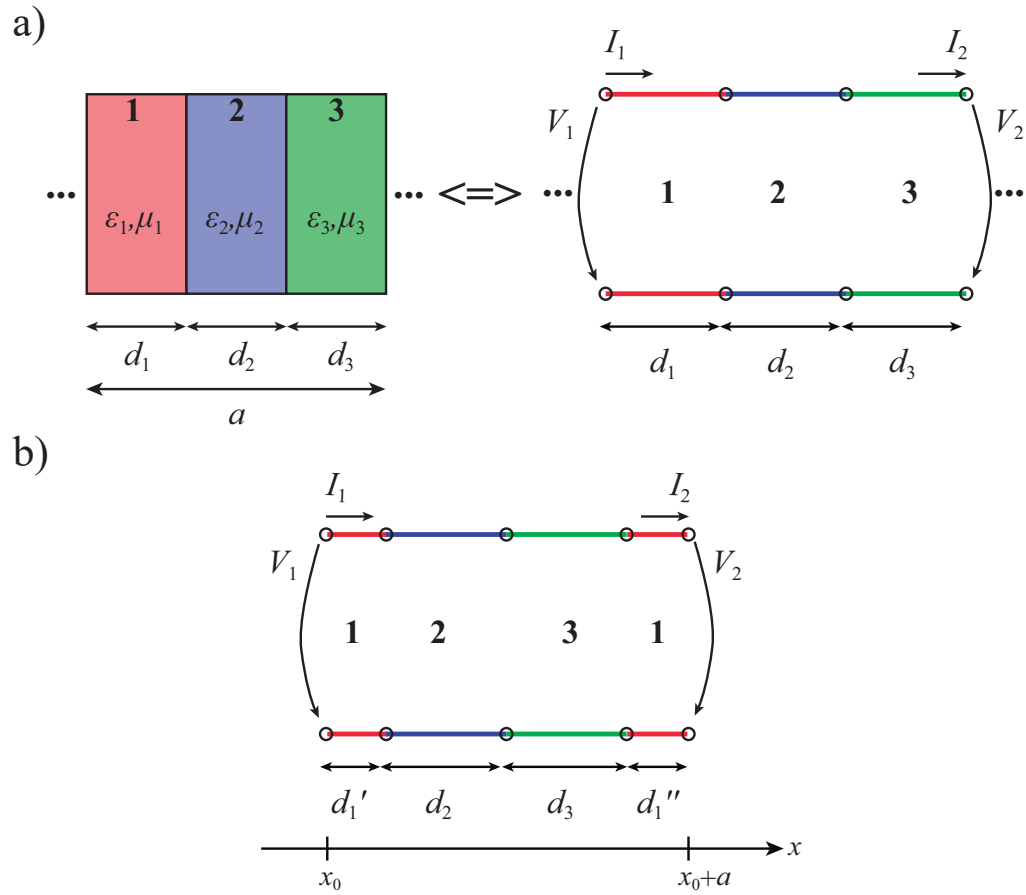
Figure 5.7: (a) Equivalence between a multi-layered photonic crystal and a periodic transmission line. (b) Geometry used in the calculation of the Bloch impedance.

We denote $Z_{\mathrm{L}}(x_0, \omega)$ and $Z_{\mathrm{R}}(x_0, \omega)$ as the Bloch impedances of the (unbounded) photonic crystal calculated at the plane $x = x_0$ when looking at the left or right, respectively (Fig. 5.1(ai)). To derive the formulas of the Bloch impedances we also use the analogy with transmission lines as before. Let us suppose without loss of generality that $x = x_0$ lies in the first line section of the equivalent transmission line, as illustrated in Fig. 5.7(b). It is convenient to obtain the global ABCD matrix ($\mathbf{M}(x_0)$) for one period, with the input and output voltages and currents referred to the planes $x = x_0$ and $x = x_0 + a$, respectively (Fig. 5.7(b). This is done as before by multiplying the ABCD matrices of the uniform line sections. For the example, for the geometry shown in Fig. 5.7(b) one has:

$$\mathbf{M}(x_0) = \begin{pmatrix} A & B \\ C & D \end{pmatrix}_{1,d_1'} \begin{pmatrix} A & B \\ C & D \end{pmatrix}_{2,d_2} \begin{pmatrix} A & B \\ C & D \end{pmatrix}_{3,d_3} \begin{pmatrix} A & B \\ C & D \end{pmatrix}_{1,d_1''}.$$
(5.21)

Note that d_1' and d_1'' depend on x_0. Similar to Eq. (5.19), for Bloch waves associated with a propagation factor $e^{-(\pm\gamma)x}$ the output voltage and current satisfy:

$$(\mathbf{M}(x_0) - \mathbf{1}e^{\pm\gamma a}) \cdot \begin{pmatrix} V_2 & I_2 \end{pmatrix}^T = 0.$$
(5.22)

Note that $\gamma = \gamma(\omega)$ depends exclusively on the frequency and can be found from Eq. (5.20). In the band-gaps γ is complex-valued and it is implicit that $\mathrm{Re}\{\gamma\} > 0$. Denoting $\mathbf{M}(x_0) = \begin{pmatrix} A & B \\ C & D \end{pmatrix}$ it follows from Eq. (5.22) that:

$$\begin{pmatrix} V2 \\ I2 \end{pmatrix} \sim \begin{pmatrix} -B \\ A - e^{\pm\gamma a} \end{pmatrix} \sim \begin{pmatrix} D - e^{\pm\gamma a} \\ -C \end{pmatrix}.$$
(5.23)

Hence, the Bloch impedance for a wave that propagates towards the positive x-direction is

$$Z_{\mathrm{R}}(x_0) = \frac{V_2}{I_2} = \frac{-B}{A - e^{\gamma a}} = \frac{D - e^{\gamma a}}{-C},$$
(5.24)

whereas the Bloch impedance for a wave that propagates towards the negative x-direction is:

$$Z_{\mathrm{L}}(x_0) = \frac{V_2}{-I_2} = \frac{B}{A - e^{-\gamma a}} = \frac{D - e^{-\gamma a}}{C}.$$
(5.25)

We used the fact that the Bloch impedances are periodic: $Z_{\mathrm{R}}(x_0) = Z_{\mathrm{R}}(x_0 + a)$, etc.

Appendix B: Relation between the Zak phases of two symmetry centers

Here, we consider a generic scalar Hamiltonian $\hat{H}(x, -i\partial_x)$ with inversion symmetry $(\hat{H}(x, -i\partial_x) = \hat{H}(-x, i\partial_x))$ and periodic in x, so that $\hat{H}(x, -i\partial_x) = \hat{H}(x+a, -i\partial_x)$. Next, it is shown that the Zak phases of two generic symmetry centers $(x = Na/2$ and $x = 0)$ are unambiguously related as $\tilde{\theta}_{\mathrm{Zak}} = \theta_{\mathrm{Zak}} + N\pi$.

As already discussed in Sect. 5.2, the Bloch eigenmodes Ψ_k of $\hat{H}$ can be picked in such a way that $\Psi_k(x) = u_k(x)e^{ikx}$ is a globally defined smooth periodic function of k. Since the system has inversion (parity) symmetry, it follows that $\Psi_k(-x)$ is also an eigenmode, but associated with the wave number $-k$. Let θ_k be such that

$$\Psi_k(x) = \Psi_{-k}(-x)e^{i\theta_k}, \tag{5.26}$$

for all k, or equivalently $e^{i\theta_k} = \Psi_k(x)/\Psi_{-k}(-x)$. The division is defined only because the state vector is a scalar; the normalization $\langle \Psi_k | \Psi_k \rangle = 1$ is implicit and guarantees that θ_k is real-valued. Evidently, $e^{i\theta_k}$ is periodic, smooth and globally defined because $\Psi_k(x)$ also is. This implies that θ_k can also be globally defined as a smooth function; θ_k is uniquely defined modulo 2π for a given $\Psi_k(x)$. Different from $\Psi_k(x)$, θ_k does not need to be periodic. However $e^{i\theta_k}$ is forcibly periodic, and thereby we must have:

$$\theta_{k+\frac{2\pi}{a}} - \theta_k = 2\pi n, \tag{5.27}$$

for some n integer (independent of k).

Let us now introduce a 1D Berry potential defined as

$$\mathcal{A}_k = i\langle u_k | \partial_k u_k \rangle, \tag{5.28}$$

with $u_k(x) = \Psi_k(x)e^{-ikx}$ the state vector envelope. Noting that $e^{i\theta_k} = u_k(x)/u_{-k}(-x)$ and using $\mathcal{A}_{-k} = -i\langle u_{-k} | \partial_k(u_{-k}) \rangle = -\mathcal{A}_k - \partial_k \theta_k$ it follows that

$$\mathcal{A}_{-k} + \mathcal{A}_k = -\partial_k \theta_k. \tag{5.29}$$

Hence, by integrating both sides of the formula we get

$$\theta_{\text{Zak}} \equiv \int_{-\pi/a}^{\pi/a} \mathcal{A}_k dk = -\frac{1}{2}(\theta_{\pi/a} - \theta_{-\pi/a}). \tag{5.30}$$

Here, θ_{Zak} is the so-called Zak phase [39], which from Eq. (5.27) is necessarily an integer multiple of π.

Because of the inversion symmetry and of the periodicity, $x = Na/2$ is also a center of symmetry. Thus, it is also possible to write $\Psi_k(x - Na/2) = \Psi_{-k}(-x - Na/2)e^{i\tilde{\theta}}_k$ for some $\tilde{\theta}_k$. From Eq. (5.26), one finds $\Psi_k(x - Na/2) = \Psi_k(x + Na/2)e^{-i\theta_k}e^{i\tilde{\theta}_k}$ or equivalently, using the Bloch property $\Psi_k(x - Na/2) = \Psi_k(x + Na/2)e^{-i\theta_k}e^{i\tilde{\theta}_k}e^{ikNa}$. This proves that

$$\tilde{\theta}_k = \theta_k - kNa + 2\pi l, \tag{5.31}$$

with l an integer independent of k. From $\Psi_k(x-Na/2) = \Psi_{-k}(-x-Na/2)^{i\tilde{\theta}_k}$ we get $\tilde{u}_k(x) = \tilde{u}_{-k}(-x)^{i\tilde{\theta}_k}$ with $\tilde{u}_k(x) = \Psi_k(x - Na/2)e^{-ikx}$. Hence, the 1D Berry potential for the second center of symmetry $\tilde{\mathcal{A}}_k = i\langle \tilde{u}_k | \partial_k \tilde{u}_k \rangle$ satisfies a formula analogous to Eq. (5.30):

$$\tilde{\mathcal{A}}_{-k} + \tilde{\mathcal{A}}_k = -\partial_k \tilde{\theta}_k. \tag{5.32}$$

From Eq. (5.31) it is now evident that the Zak phase for the second center of symmetry is such that:

$$\tilde{\theta}_{\text{Zak}} = \theta_{\text{Zak}} + N\pi. \tag{5.33}$$

The above formula is consistent with the well-known fact that the Zak phase depends on the center of symmetry [39].

Bibliography

[1] M. Z. Hasan, , and C. L. Kane, "Colloquium: Topological insulators," *Rev. Mod. Phys.*, vol. 82, p. 3045, 2010.

[2] X. L. Qi and S. C. Zhang, "Topological insulators and superconductors," *Rev. Mod. Phys.*, vol. 83, 2011.

[3] F. D. M. Haldane, "Nobel lecture: Topological quantum matter," *Rev. Mod. Phys.*, vol. 89, p. 040502, 2017.

[4] F. D. M. Haldane and S. Raghu, "Possible realization of directional optical waveguides in photonic crystals with broken time-reversal symmetry," *Phys. Rev. Lett.*, vol. 100, p. 013904, 2008.

[5] Y. C. Z. Wang, J. D. Joannopoulos, and M. Soljačić, "Observation of unidirectional backscattering immune topological electromagnetic states," *Nature*, vol. 461, p. 772, 2009.

[6] A. B. Khanikaev, S. H. Mousavi, W. K. Tse, M. Kargarian, A. H. MacDonald, , and G. Shvets, "Photonic topological insulators," *Nat. Mater.*, vol. 12, p. 233, 2012.

[7] M. C. Rechtsman, J. M. Zeuner, Y. Plotnik, Y. Lumer, D. Podolsky, F. Dreisow, S. Nolte, M. Segev, and A. Szameit, "Photonic floquet topological insulators," *Nature*, vol. 496, p. 196, 2013.

[8] L. Lu, J. D. Joannopoulos, and M. Soljačić, "Topological photonics," *Nat. Photonics*, vol. 8, p. 821, 2014.

[9] M. G. Silveirinha, "Chern invariants for continuous media," *Phys. Rev. B*, vol. 92, p. 125153, 2015.

[10] S. A. H. Gangaraj, M. G. Silveirinha, and G. W. Hanson, "Berry phase, berry connection, and chern number for a continuum bianisotropic material from a classical electromagnetics perspective," *IEEE J. Multiscale and Multiphys. Comput. Techn.*, vol. 2, p. 3, 2017.

[11] T. Ozawa, H. M. Price, A. Amo, N. Goldman, M. Hafezi, L. Lu, M. C. Rechtsman, D. Schuster, J. Simon, O. Zilberberg, and I. Carusotto, "Topological photonics," *Rev. Mod. Phys.*, vol. 91, p. 015006, 2019.

[12] M. G. Silveirinha, "Topological classification of chern-type insulators by means of the photonic green function," *Phys. Rev. B*, vol. 97, p. 115146, 2018.

[13] M. G. Silveirinha, "Topological theory of non-hermitian photonic systems," *Phys. Rev. B*, vol. 99, p. 125155, 2019.

[14] V. M. M. Alvarez, J. Vargas, M. Berdakin, and L. E. F. F. Torres, "Topological states of non-hermitian systems," *Eur. Phys. J. Special Topics*, 2018.

[15] V. Peano, M. Houde, F. Marquardt, and A. A. Clerk, "Topological quantum fluctuations and traveling wave amplifiers," *Phys. Rev. X*, vol. 6, p. 041026, 2016.

[16] D. Leykam, K. Y. Bliokh, C. Huang, Y. D. Chong, and F. Nori, "Edge modes, degeneracies, and topological numbers in non-hermitian systems," *Phys. Rev. Lett.*, vol. 118, p. 040401, 2017.

[17] H. Shen, B. Zhen, , and L. Fu, "Topological band theory for non-hermitian hamiltonians," *Phys. Rev. Lett.*, vol. 120, p. 146402, 2018.

[18] S. Yao and Z. Wang, "Edge states and topological invariants of non-hermitian systems," *Phys. Rev. Lett.*, vol. 121, p. 086803, 2018.

[19] S. Yao, F. Song, and Z. Wang, "Non-hermitian chern bands," *Phys. Rev. Lett.*, vol. 121, p. 136802, 2018.

[20] F. K. Kunst, E. Edvardsson, J. C. Budich, and E. J. Bergholtz, "Biorthogonal bulk-boundary correspondence in non-hermitian systems," *Phys. Rev. Lett.*, vol. 121, p. 026808, 2018.

[21] Z. Gong, Y. Ashida, K. Kawabata, K. Takasan, S. Higashikawa, and M. Ueda, "Topological phases of non-hermitian systems," *Phys. Rev. X*, vol. 8, p. 031079, 2018.

[22] Z. Liu, E. J. Bergholtz, H. Fan, and A. M. Laeuchli, "Fractional chern insulators in topological flat bands with higher chern number," *Phys. Rev. Lett.*, vol. 109, p. 186805, 2012.

[23] J. Behrmann, Z. Liu, and E. J. Bergholtz, "Model fractional chern insulators," *Phys. Rev. Lett.*, vol. 116, p. 216802, 2016.

[24] A.-L. He, W.-W. Luo, Y.-F. Wang, and C.-D. Gong, "Fractional chern insulators in singular geometries," *Phys. Rev. B*, vol. 99, p. 165105, 2019.

[25] A. Raman and S. Fan, "Photonic band structure of dispersive metamaterials formulated as a hermitian eigenvalue problem," *Phys. Rev. B*, vol. 104, p. 087401, 2010.

[26] M. G. Silveirinha, *Advances in Mathematical Methods for Electromagnetics*, ch. Modal expansions in dispersive material systems with application to quantum optics and topological photonics. IET, 2019.

[27] L. Yuan, Q. Lin, M. Xiao, and S. Fan, "Synthetic dimension in photonics," *Optica*, vol. Optica, p. 1396, 2018.

[28] T. Ozawa and H. M. Price, "Topological quantum matter in synthetic dimensions," *Nat. Rev. Phys.*, vol. 1, p. 349, 2019.

[29] E. Lustig, S. Weimann, Y. Plotnik, Y. Lumer, M. A. Bandres, A. Szameit, and M. Segev, "Photonic topological insulator in synthetic dimensions," *Nature*, vol. 567, p. 356, 2019.

[30] Y. Hatsugai, "Chern number and edge states in the integer quantum hall effect," *Phys. Rev. Lett.*, vol. 71, p. 3697, 1993.

[31] *The Universe in a Helium Droplet*. Oxford, UK: Oxford University Press, 2003.

[32] V. Peano and H. Schulz-Baldes, "Topological edge states for disordered bosonic systems," *J. Math. Phys.*, vol. 59, p. 031901, 2018.

[33] M. G. Silveirinha, "Bulk edge correspondence for topological photonic continua," *Phys. Rev. B*, vol. 94, p. 205105, 2016.

[34] M. G. Silveirinha, "Proof of the bulk-edge correspondence through a link between topological photonics and fluctuation-electrodynamics," *Phys. Rev. X*, vol. 9, p. 011037, 2019.

[35] R. Bianco and R. Resta, "Mapping topological order in coordinate space," *Phys. Rev. B*, vol. 84, p. 241106(R), 2011.

[36] M. D. Caio, G. Möller, N. R. Cooper, and M. J. Bhaseen, "Topological marker currents in chern insulators," *Nat. Phys.*, vol. 15, p. 257, 2019.

[37] J. D. Joannopoulos, S. G. Johnson, J. N. Winn, and R. D. Meade, *Photonic Crystals: Molding the Flow of Light.* 2008.

[38] D. M. Pozar, *Microwave Engineering.* 2011.

[39] M. Xiao, Z. Q. Zhang, and C. T. Chan, "Surface impedance and bulk band geometric phases in one-dimensional systems," *Phys. Rev. X*, vol. 4, p. 021017, 2014.

[40] "Cst gmbh 2019 cst microwave studio."

[41] M. G. Silveirinha, "Quantized angular momentum in topological optical systems," *Nat. Comm.*, vol. 10, p. 349, 2019.

[42] M. G. Silveirinha, "Topological angular momentum and radiative heat transport in closed orbits," *Phys. Rev. B*, vol. 95, p. 115103, 2017.

CHAPTER 6

Conclusions

In this thesis I extensively studied theoretically and numerically three different mechanisms to achieve light localization with plasmonic materials, wire metamaterials and photonic crystals.

In chapter II, we studied the formation of embedded eigenstates in two-dimensional open core-shell plasmonic particles with arbitrary shape. Through theoretical and numerical analysis, we determined the geometrical conditions for each particular cross-section that have to be satisfied so that the meta-atom supports embedded eigenstates with infinite lifetimes. To circumvent the restrictions imposed by the Lorentz reciprocity theorem that forbids the direct external excitation of the eigenstates, we used a nonlinear material to break the reciprocity. Through electromagnetic simulations, we showed that this strategy is successful in exciting the embedded eigenstates and that the energy trapped inside the particle is precisely quantized. Furthermore, it was also shown that the geometry influences directly the lifetime of the trapped state.

In chapter III, we continued the study of the light trapping mechanism of the previous chapter but now considering a three-dimensional spherical meta-atom with a nonlocal plasmonic shell. We theoretically described the diffusion-effects in the shell using the hydrodynamic model and demonstrated that the meta-atom may now support multiple embedded eigenstates with suppressed radiation loss. In fact, we showed that the electron-electron interactions in the metal strongly relax the material and geometrical conditions required for the formation of bound states, allowing the same particle to

support states at multiple frequencies. With a spatially dispersive material, it is no longer required for the plasmonic shell to have a permittivity exactly equal to zero, which brings our work closer to a realistic experimental setup.

In chapter IV, we numerically studied the guided modes supported by a crossed wire grid. We started by describing the electromagnetic properties of the structure using a homogenization technique based on the transverse-average fields. After using the classical and an additional boundary conditions, we found through calculations that the structure supports a diverging number of guided mode branches that pile up near the light line for low frequencies. This behavior is due to the strong hyperbolic response of the structure near the static limit. Using an electromagnetic simulator, we found that in practice the number of guided modes is finite and depends on the wire density. Furthermore, the guided modes exhibit an extremely fast field variation along the transverse direction even though they are weakly bounded to the slab. To take advantage of this peculiarity, we devised a solution to detect subwavelength defects due to structural changes in the host material.

Finally, in chapter V we theoretically and numerically studied the topological properties of one-dimensional periodic systems. First, we showed that the number of photonic bands below a band gap can be understood as a topological number of an extended system with a synthetic dimension, defining the number of edge states in this system. In real-space, these states correspond to localized modes at an interface of one-dimensional crystals, for a given shift in the unit cell. For a full unit cell shift, the number of trapped states branches is exactly equal to the number of photonic bands below the gap. We established a rigorous and simple bulk-edge correspondence for interfaces of one-dimensional systems and numerically illustrated its application with several examples. In the second part of our chapter, we considered only systems with inversion symmetry and a shift in the unit cell of half-lattice period. We showed that these systems are characterized by a fractional Chern number equal to the number of bands below the gap divided by two. This result unveils an entirely novel class of topological systems with fractional topological invariants, which we conjecture may lead to unique physical phenomena.